Synthesis, Characterization and Optical Properties of Blue and Green Inorganic Pigments for Coloring Applications

Thesis submitted to

Cochin University of Science and Technology

In partial fulfillment of the requirements for the award of the degree of

Doctor of Philosophy

in

Chemistry

under

The Faculty of Science

by

Divya S.

(Reg: No- 4346)

Materials Science and Technology Division
National Institute for Interdisciplinary
Science and Technology (NIIST)
Council of Scientific and industrial Research
Thiruvananthapuram-695019
Kerala, India

2017

Synthesis, Characterization and Optical Properties of Blue and Green Inorganic Pigments for Coloring Applications

PhD Thesis in the field of Materials Science

Author:
Divya S.
Materials Science and Technology Division
National Institute for Interdisciplinary
Science and Technology (NIIST)
Thiruvananthapuram - 695019, Kerala, India

Supervising Guide:
Dr. P. Prabhakar Rao
Materials Science and Technology Division
National Institute for Interdisciplinary
Science and Technology (NIIST)
Thiruvananthapuram - 695019, Kerala, India

November 2017

DECLARATION

I hereby declare that the work presented in this thesis entitled **“Synthesis, Characterization and Optical Properties of Blue and Green Inorganic Pigments for Coloring Applications”** is based on the original research work done by me at the Materials Science and Technology Division, National Institute for Interdisciplinary Science and Technology (NIIST), CSIR, Thiruvananthapuram, under the supervision of **Dr. P. Prabhakar Rao**, Chief Scientist and has not been included in any other thesis submitted previously for the award of any degree.

Divya S.

Thiruvananthapuram
Date:

COUNCIL OF SCIENTIFIC AND INDUSTRIAL RESEARCH
NATIONAL INSTITUTE FOR INTERDISCIPLINARY SCIENCE AND TECHNOLOGY (CSIR-NIIST)
Industrial Estate (P.O), Thiruvananthapuram-695 019
Kerala, India

Dr. P. Prabhakar Rao
Chief Scientist
Materials Science and Technology Division

Telephone: 91-471-2515311
Fax: 91-471-2491712
E-mail: padala_rao@yahoo.com

CERTIFICATE

This is to certify that the thesis entitled **"Synthesis, Characterization and Optical Properties of Blue and Green Inorganic Pigments for Coloring Applications"** is a bonafide record of the research work carried out by **Ms. Divya S.** under my guidance and supervision in partial fulfilment of the requirement for the degree of Doctor of Philosophy of Cochin University of Science and Technology (CUSAT).

All the relevant corrections, modifications and recommendations suggested by the audience and the doctoral committee members during the pre-synopsis seminar have been incorporated in the thesis. I also certify that this work and no part of it has been submitted elsewhere for the award any other degree.

P. Prabhakar Rao
(Thesis supervisor)

Thiruvananthapuram
November 2017

ACKNOWLEDGEMENTS

The work presented in this thesis would not have been possible without my close association with many people who were always there when I needed them the most. I take this opportunity to acknowledge them and extend my sincere gratitude for helping me make this Ph.D. thesis a possibility.

Firstly, I express my heartfelt gratitude to my supervisor D. P. Prabhakar Rao for the continuous support of My Ph.D. study and related research. Without his continuous optimism concerning this work, enthusiasm, encouragement, and support, this study would hardly have been completed. His guidance helped me in all the time of research and writing of this thesis.

I am grateful to the present and former directors of NIIST, Dr. A. Ajayghosh, Dr. Gangan Pratap and Dr. Suresh Das for giving me an opportunity to work in this institute and making the facilities available for carrying out research.

My sincere thanks also goe to Dr. M. T. Sebastian, Dr. M. L. P. Reddy and Dr. P. Prabhakar Rao who had held the position of Head of Materials Science and Technology Division, who provided me an opportunity to join in the division, and who given access to the laboratory and research facilities. Without they precious support it would not be possible to conduct this research.

I am thankful to Prof. S. Sugunan, Dept. of Chemistry, CUSAT for his support as an external expert in Doctoral Committee of my research, for his comments that helped a lot in its improvement.

I acknowledge the Council of Scientific and Industrial Research (CSIR), Government of India for providing me with the necessary funding and fellowship to pursue research at NIIST.

My special word of thanks goes to the peoples who helped me for the sample analyses, especially Mr. Chandran for the beautiful SEM images. Thanks also goes to Mrs. Lucy Paul, Mr. Harish, Mrs. Soumya and Mr. Pratuviraj for their efficient service.

I would like to acknowledge all the teachers I learned from since my childhood, I would not have been here without their guidance, blessing, and support. A very special gratitude goes out to Johnson Sir, Sethu Sir, Mani Sir, and Kessiyamma teacher who offered a collegial guidance and encouragement over the years.

My sincere thanks to all my lab seniors and to my fellow labmates who have taught me the lab culture and have lived by example to make me understand the hard facts of life. I would like to acknowledge Dr. Sandhyakumari L, Dr. Mariyam Thomas, Dr. Radhakrishnan A. N, Dr. Sameera S, Mr. Mahesh S. K, Dr. Sumi S, Dr. Vaisakhan Thampi D. S, Mrs. Reshmi V. R, Mrs. Vineetha James, Ms. Sreena T. S, Mrs. Athira K. V. Raj, Mrs. Renju U. A, Mrs. Parvathi S. Babu, Ms. Suchithra V. G, Mrs. Aswathy B. A, Ms. Ajuthara, Dr. Bridha, Mrs. Soumya, Mr. Pruthiviraj, Mr. Shanoj, and Ms. Haritha in the lab. I would like to thank M.Sc. and M. Phil project students, Mrs. Sreeja, Mrs. Subhalekshmi and Ms. Divya.

My heartfelt thanks to my friends for their moral support and motivation, which drives me to give my best. Arya, Shaban, Surjith, Vishnu, Hari Sanil, Rahul, Dhaneesh, Amal, Deepak, Hari Krishnan, Akhil, Shankar, Rajeev, Suneeth, Mithun, Adharsh, Shyni, Kavitha, Vidhya, Anju, Deepu, Hazeena …the list is endless…thanks to one and all. Thanks for being with me in thicks and thins of life, I find myself lucky to have friends like them in my life.

Very special thanks goes to my parents, Mr. Ayyappan Pillai and Mrs. Saraswathy Amma for showing faith in me and giving me the liberty to choose what I desired. I salute you all for the selfless love, care, pain, and sacrifice you did to shape my life. In addition, I express my thanks to my sister Deepa, for her inspiration and support. I also thank Mr. Raveendran Pillai (vallyamaman) and Mr. Venugopal (Kochumaman) for their support and care.

I owe my tremendous and deep thanks to my husband, Renjith for his support and understanding during my pursuit of the Ph.D. degree that made the completion of thesis possible. I greatly value his contribution and deeply appreciate his belief in me.

My heartfelt regards goes to my father in law (Mr. Radhakrishnan), mother in law (Mrs. Indhira) and sister in law (Mrs. Reji) for their love and moral support.

Finally, I thank all my well-wishers who have directly or indirectly contributed to my research work. Thank you all once again for the unconditional love and support.

Divya S.

CONTENTS

Chapter 3 Monoclinic $LaGa_{1-x}Mn_xGe_2O_7$: A new blue chromophore based on Mn^{3+} in trigonal bipyramidal coordination with longer apical bonds 70

Chapter 4 Influence of aliovalent cation substitutions on the optical properties of $In_2Cu_2O_5$ system 90

Chapter 5 Enhanced pigmentary properties of rare earth germanates of the type $La_2CuGe_2O_8$ through distortion in CuO_6 octahedron 120

Chapter 6 Conclusions and future scope 146

LIST OF FIGURES

LIST OF TABLES

ABBREVIATIONS

CICPs : Complex Inorganic Color Pigments

UV: Ultraviolet

vis: Visible

IR : Infrared

NIR: Near Infrared

CIE: Commission Internationale de l'Eclairage

K-M: Kubelka Munk

XRD : X-ray Diffraction

PXRD: Powder X-ray Diffraction

SEM Scanning Electron Microscopy

TBP: Trigonal Bipyramidal

M–O: Metal-Oxygen

PVC: Polyvinyl Chloride

CT: Charge Transfer

TM: Transition Metal

JCPDS: Joint Committee on Powder Diffraction Standards

BVS: Bond Valence Sum

SSR: Solid State Reaction

ASTM: American Society for Testing and Materials

PPMS: Physical Property Measurement System

EDS: Energy Dispersive Spectrometer

C.N: Coordination Number

PMMA: Poly(methyl methacrylate)

PTFE: Poly–tetrafluoroethylene

PREFACE

Inorganic pigments have been widely used for a large variety of industrial applications such as in ceramic tiles, inks, plastics, glasses etc. Among the primary colored pigments, blue and green colored quality materials are relatively rare. Currently used inorganic blue pigments are cobalt blue ($CoAl_2O_4$), ultramarine blue ($Na_7Al_6Si_6O_{24}S_3$) and Prussian blue, ($Fe_4[Fe(CN)_6]_3$) etc. Ultramarine blue and azurite are sensitive to acid, while Prussian blue possesses poor alkali stability. Raising cost and toxicity make a pressing need to reduce the consumption of cobalt in the ceramic industry. Recently a blue inorganic pigment, $YIn_{1-x}Mn_xO_3$, based on hexagonal $YInO_3$ was reported. The blue color of the oxides arises from the specific trigonal bipyramidal ligand field around Mn^{III} in a $YInO_3$ host. However, a few host structures having a Mn^{3+} ion in their geometry have been found so far.

Conventional industrial green pigments such as chrome oxide green (Cr_2O_3), cobalt green ($CoO \cdot ZnO$), and cobalt titanate green spinel (Co_2TiO_4) have serious problems from a practical viewpoint. Cr_2O_3 contains toxic Cr, and $CoO \cdot ZnO$ and Co_2TiO_4 are less than perfect in green color. Apart from this, high infrared reflective pigments are now in great demand for usage in coatings, cement pavements, automotive and camouflage applications. The main objective of the present research work is to develop alternatives to the existing blue and green inorganic pigments that are more sustainable and commercially viable for potential applications.

The present thesis is organized into six chapters. Introduction chapter details inorganic pigments and their areas of interest, basic concepts of color, color theories. Along with a brief literature review, an emphasis is given on the research efforts in Cobalt(II) and Manganese(III) based blue pigments and Copper(II) based green pigments. Main objectives of the current work are highlighted and the motivation and importance of choosing this area are stressed.

With the aim of reducing the consumption of cobalt in the ceramic industry and improve efficiency and sustainability of pigments, we developed $Mg_{1-x}Co_xWO_4$ based blue pigments are described in chapter two. It was observed that increasing the amount of cobalt induces a change in the local symmetry of MgO_6 octahedra witnessed by change of the metal-ligand bond distances. The observations suggested that structural distortions, which were dependent on the ionic radii and electronegativity difference between the dopant and host cations. The synthesized pigments show intense blue color than $CoAl_2O_4$ with a very low doping concentration of cobalt with b^* value of -46.7.

The third chapter correlates the synthesis of a novel blue inorganic pigment with the introduction of Mn^{3+} in the trigonal bipyramidal site of the host lattice $LaGaGe_2O_7$. In the host lattice of monoclinic $LaGaGe_2O_7$ substitution of Mn^{3+} changes the color from white to blue. This absorption arises due to the d-d transition taking place from the crystal field splitting of Mn^{3+} in the trigonal bipyramidal site. Mn–O apical bond lengths play a key role in the d-d component of transition. The developed pigments are environmentally benign.

In the chapters, four and five we attempt to improve the optical properties of Cu based green colored $In_2Cu_2O_5$ and blue-green colored $La_2CuGe_2O_8$. We tried to enhance the optical properties through distortion and modifications of the crystal field environment around the transition metal ion. With a view to distorting the crystal field around the Cu^{2+} ion, we modified the polarizability around the Cu^{2+} ion through the introduction of Sc^{3+} and Zn^{2+} ions in the divalent and trivalent site of the host lattice. The trend in the optical properties with respect to Zn^{2+} and Sc^{3+} doping was analyzed and the thermal and chemical stability were well studied which are discussed in chapter five. The synthesized pigments possess more color and reflectance than conventional and commercially available Cr_2O_3 green pigment.

In chapter five, we described the enhanced pigmentary properties of blue–green $La_2CuGe_2O_8$. Optical properties of the synthesized samples are enhanced with the doping of monovalent (Li^+) in the Cu^{2+} site. The polarizability of oxygen ion of Cu–O/Li–O bonds in the solid solutions tunes the crystal field strength around Cu^{2+} ion such that intense blue-green color results for materials with small doping concentration. Application study of selected pigments to evaluate their coloring performance as well as IR reflectance to various substrates like PMMA, concrete slab and the metal plate were also discussed in this chapter.

Conclusions drawn from the studies on the optical properties of these synthesized inorganic pigments and gives the scope for further studies are presented in chapter six. These developed pigments demonstrate thermally and chemically stable, weather resistant and cost effective which make them suitable for various surface coating applications. We expect that our results will lead to the development of many environmentally benign and highly stable inorganic pigments from the derivatives of the investigated systems.

1

INTRODUCTION

Color plays an increasingly important role in daily life. We all like a bit of color in our life, man has been using paints to give us this touch of color ever since the days of cave paintings. Nowadays paints and dyes are used for everything from home appliances to homes themselves. In keeping with its status as one of the leading visual arts, painting is heavily dependent upon the use of color for its impact, mood and depth. Color is introduced into these materials and applications using substances are known as pigments. Synthesis and development of new colored inorganic pigments are the hot topic in the present scenario. This chapter includes the general introduction about colorants, color theory, application and the recent development in this field.

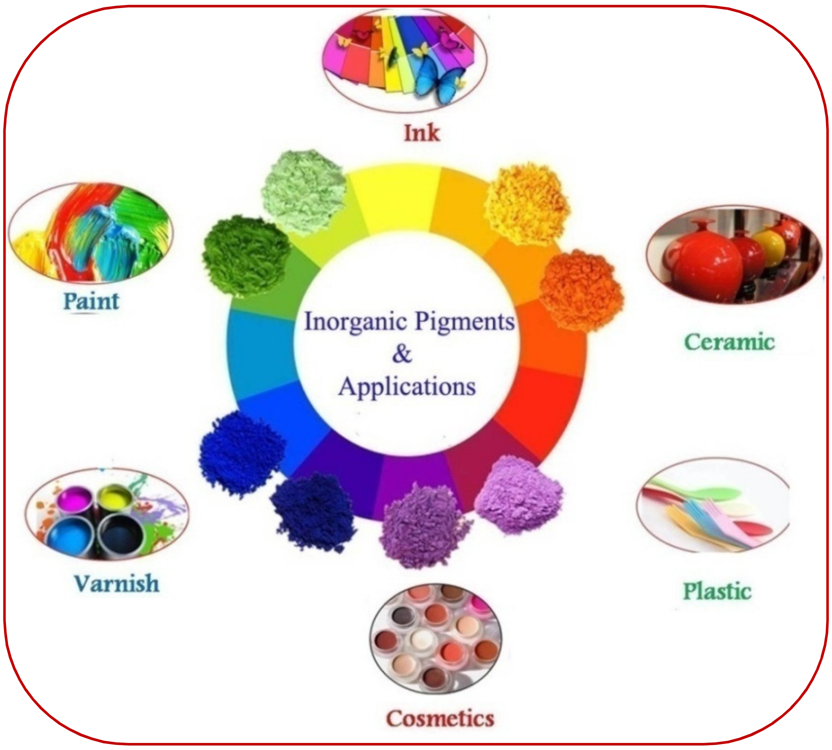

1.1 Colorants

Colorants are materials that alone or in combination with other elements, impart or change the color of the product. The visual perception of color occurs primarily by the absorption or reflection of visible light by the product and corresponds to humans seeing red, yellow, blue, green, black, etc. Colorants are used in many industries to color clothes, paints, plastics, photographs, prints, and ceramics. They are also now being used in novel applications and are termed functional as they are not just included in the product for aesthetic reasons. Colorants can be either dyes or pigments. The important characteristic that distinguishes both pigment and dye is their solubility. Dyes are soluble colored organic compounds that are usually applied to textiles from a solution in water. On the other hand, pigments are the colorants composed of particles that are insoluble in the medium in which they are applied [1]. Dyes have a stronger affinity for the medium to which they are being applied [2]. In application process dyes temporarily destroys the crystal structure by absorption, solution and mechanical retention or by ionic or covalent chemical bonds [3]. Dyes provide brighter color than conventional pigments, but they are less light stable and less permanent [4]. They provide color to the medium simply by mechanical dispersion. The word pigment used for denoting the color of a material and it originated from the Latin word pigmentum [5]. In the late middle ages, the word used by all kinds of vegetable and plant extracts used for coloring. The modern meaning of pigment originated in this century. They alter an appearance by selective absorption or by scattering of light [6]. In contrast to dyes, whose coloristic properties are almost exclusively defined by their chemical structure, the properties of pigments also depend on the physical characteristics of its particles [7]. Today there are lots of pigments available in the market. After the development of synthetic pigments, there has evolved different classes of pigments that are suited to particular types of applications. Both dyes and pigments fall into the colorant family of chemical compounds. With this classification, for the deep understanding of the colorant family, we can classify the two primary types of pigments which are organic and inorganic. If a pigment is a preferred colorant for a certain application, both organic and inorganic pigments may be presented as options.

1.2 Organic Pigments

They are not usually found in nature. That is the reason that a majority of these pigments is chemically synthesized. Carbon chains or carbon rings are always present in the molecules of the organic pigments. The atoms of nitrogen and sulphur atoms are also found along with the carbon atoms. Organic pigments with comparatively low levels of toxicity, not providing any major environmental issue. Coal tar and petroleum distillates are used as the raw materials and transformed them into insoluble precipitates. Traditionally organic pigments are used as mass colorants. They are popular in plastics, synthetic fibers and as surface coatings paints and inks. Nowadays, the organic pigments are used for industrial applications that comprise photo-reprographics, optoelectronic displays, and optical data storage. Examples: Azo, Phthalocyanine, diazo and anthraquinone pigments.

1.3 Inorganic Pigments

An inorganic pigment is a colored or hue less colorant insoluble in solvents and binders. Inorganic pigments are mainly obtained from naturally occurring mineral sources or minerals, which have been obtained synthetically. These raw materials are mainly oxides, sulphides of one or more than one metals. These pigments obtain their extraordinary properties through a combination of special manufacturing processes. The preparation process is simple and consists of the steps of washing, drying, pulverizing and mixing into a formulation. Inorganic pigments are composed of transition metals surrounded by ligands, mainly oxides of crystalline or semi-crystalline repeating units of the crystal lattice structure. The d-orbital of the metal ions is responsible for the properties of inorganic pigment, including color, reactivity, strength and weatherability. The way in which the d-orbital of the metal ion interacts with the various ligands to which it is bonded also affects the pigment properties. A few of these heavy metal pigments are no longer in use because new environmental laws are very strict about toxic. Lead oxide, cobalt blue, and nickel titanate are some of the examples.

1.4 History of Inorganic Pigments

Natural inorganic pigments have been known from the prehistoric times. The first colorant used by peoples of southern France, northern Spain, and northern Africa for the cave paintings are made with charcoal, manganese brown and clays.

Arsenic sulfide and lead, antimony is the first yellow pigments they are generally known as Naples yellow. Ultramarine (Lapis Lazuli), Egyptian blue and cobalt aluminate was the first blue pigments. The first green pigments are terra verte, malachite and synthetically prepared copper hydroxyl chloride. Inorganic pigments are divided into two subtype's natural and synthetic inorganic pigments. Red earth is the most diverse kind of inorganic pigment. The color varies from dull yellow to dull deep yellow or from dull orange to dull red or from dull dark brown to dark brown. Red iron oxides were found in all parts of the world and have been used as pigments since the prehistoric time. Natural manganese ores are added to red earth to create darker red, violet or black colors in pottery clays or glazes. Yellow earth is a natural earth containing silica and clay and they are found around the world and have been used as pigments since prehistory. These pigments are present in the hydrous form of iron oxide and also contain gypsum or manganese carbonate. Green earth has been used around the world since prehistoric times, which is completely lightfast and chemically inert. A complex rock mixture of the deep blue mineral lazurite (natural ultramarine) is the most complex mineral pigment. This is found in China, Tibet, and Central Asia, and used in jewelry, and painting in ancient Babylonian and Egyptian cultures. It was used as a very expensive reddish blue pigment in medieval manuscripts and art. The pigment is decomposed by acids, but is otherwise very permanent. Azurite is a natural inorganic pigment used for a very long period. These pigments are of copper carbonates having greenish blue shade. But often these pigments have been replaced by synthetic pigments or employed to paint the ultramarine as underpaintings. The ancient Egyptians used the green form of hydrous copper carbonate, called malachite green as a green pigment. In malachite green, the color is not permanent and it is significantly lightening and shifts toward blue as particle size decreases. Synthetic inorganic pigments are prepared in the laboratory and it is available in the pure form. Synthetic pigments consist of compounds like manganese violet, cobalt blue etc.

1.5 Classification of Inorganic Pigments

Inorganic pigments can be categorized on the basis of their chemical structure, optical properties, or technological properties. The classification is given in table 1.1 based on coloristic and chemical considerations.

Table 1.1 Classification of inorganic pigments

White pigments	the optical effect is caused by nonselective light scattering (eg: titanium dioxide and zinc white)
Colored pigments	the optical effect is caused by selective light absorption and also to a large extent by selective light scattering (eg: iron oxide red pigments, ultramarine pigments)
Black pigments	the optical effect is caused by nonselective light absorption (eg: carbon black, iron oxide black)
Effect pigments	the optical effect is caused by regular reflection or interference
Metal effect pigments	regular reflection takes place on mainly flat and parallel metallic pigment particles (eg: aluminum flakes)
Pearl luster pigments	regular reflection takes place on highly refractive parallel pigment platelets (eg : titanium dioxide on mica)
Interference pigments	the optical effect of colored luster pigments is caused wholly or mainly by the phenomenon(eg: iron oxide on mica)
Luminescent pigments	the optical effect is caused by the capacity to absorb radiation and to emit it as light of a longer wavelength
Fluorescent pigments	the light of longer wavelength is emitted after excitation without a delay (eg: silver-doped zinc sulfide)
Phosphorescent pigments	the light of longer wavelength is emitted within several hours after excitation (eg: copper-doped zinc sulfide)

1.6 Advantages of Inorganic Pigments

Inorganic pigments are considered superior to their organic counterparts. They can resist the effect of sunlight and chemical exposure in a better way. They have good opacity and thus these can protect other substances by preventing the light. These pigments also enhance rash inhibition, abrasion resistance and rigidity to the molecules. The costs of production of inorganic pigments are lower than that of organic pigments. Inorganic pigments are now highly engineered particles that impart color to the objects in which they are applied. While inorganic pigments are still used in applications, such as paints, ceramics, and cement etc. Their resistance to the effects of radiation, temperature, and chemical attack has also led to use in high technology applications, such as fibers, engineering plastics, and highly durable coatings applied to roofing panels and even space equipment. The basic technology for making inorganic pigments is hundreds or thousands of years old. Pigment production may be considered to be 30000 years old, with the evidence being the splendid cave paintings found in France and Spain. Pigment technology has evolved, and within each pigment chemistry, the most cost efficient pigment in terms of particle size, crystal structure, or composition is used to provide the desired color.

For exterior or high heat coatings applications physical and spectral features of pigments have an important consideration. Heat and chemical stability, UV opacity, hiding power and IR reflectivity are important aspects in such coatings. Complex inorganic color pigments (CICPs) provide enhanced performance in these key areas. These pigments are stable and chemically inert. They can withstand the chemically aggressive environments and they will remain colorfast in the presence of strong acids, bases, oxidizing or reducing agents or other air pollutants common in industrialized areas. They are non-migratory, and will not dissolve or bleed in contact with solvents.

In addition to excellent chemical stability, they possess excellent heat stability also. They are prepared at very high temperatures in a process called calcination. Metal oxides or oxide precursors are mixed together and then heated usually at high temperatures. At the calcining temperature metal and oxygen ions in the solids rearrange to a new more stable structure forming the CICPs. CICPs are ideal for high heat coatings, such as muffler and stove coatings, fireplace paint, and high-heat powder coatings because of their inherent heat stability. Inorganic pigments are exclusively used for porcelain enamel and decorative ceramic coatings.

In external coatings, UV protection is important and they offer superior light fastness when used in outdoor coatings. CICPs are resistant to all forms of UV radiation and they absorb incident UV radiations and convert their energy to a more benign form. Because of their small particle size and high refractive index, they will efficiently backscatter a significant amount of UV light away from a coating surface. This will make them act as very good UV opacifiers. Both absorption and scattering of UV light by CICPs acts to keep this hazardous radiation from entering and degrading a coating's resin matrix. High tinting strength and opacity allows coatings formulators to decrease the quantity of pigment needed to give equivalent color. The new higher opacity CICPs are a much better value. Another area where CICPs aid in exterior coatings is in the reflection of IR or heat radiation.

Among the advantages of inorganic pigments is not only the cost because generally has excellent chemical resistance and weathering. This feature offers advantages to the coatings industry, such as low viscosity and improved dispersibility because of mechanization, which favors the reduction of energy consumption in the manufacturing processes. Their incomparable chemical and heat stability, good hiding power, UV opacity, and IR reflective properties make them ideal for these demanding applications.

1.7 IR Reflecting Pigments

Solar energy plays an important role in economic growth around the world. Light energy that arrives at the earth's surface, typically ranges from 300 to 2500 nm. Pigments are colored compounds that are responsible to give color to objects by selective absorption of light and reflect the remainder corresponding to its color. Apart from the visible region, pigments also interact with the other wavelength of light in the electromagnetic spectrum [8]. Nearly 5% of the sun's energy that reaches the Earth's surface is in the ultraviolet region (UV) (300 - 400 nm). Absorption of these UV radiations causes the photodegradation of organic materials including organic coatings. Around 50% of the sun's energy occurs in the visible region of the electromagnetic spectrum. The human eye is sensitive to the wavelength range from 400 to 700 nm in the electromagnetic spectrum. Thus, the visible region consists of wavelengths that give us the perception of color. Some 45% of the total sun's energy occurs in the infrared region (IR) whose wavelength ranges from 700 to 2500 nm [Figure 1.1]. Heat is a direct effect of either visible or infrared radiation incident on an object. The heat-producing region of the infrared radiation ranges from 700 to 1100 nm [9].

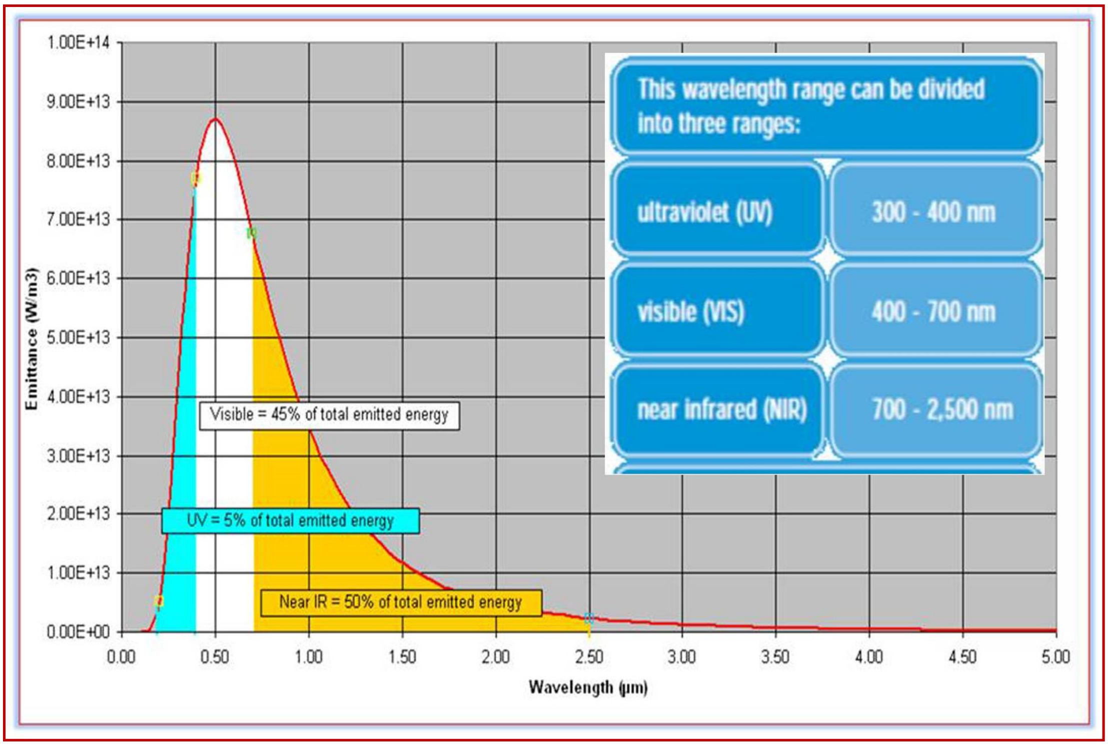

Figure 1.1 Representation of solar energy distribution.

The main purpose of IR-reflective pigments is to keep objects cooler than they would be using conventional inorganic pigments. Normally we use white paints, they reflect NIR radiations effectively, but are less useful and suitable in big cities. TiO_2 is the most employed white pigment in the formulation of paints, which reflect visible and IR radiation very well. To avoid the monotonic effect that a totally white city could produce, there are colored paints on the market, but the normal pigments used in these paints have low NIR reflection. Each pigment has distinct IR-reflective properties.

Infrared reflective inorganic pigments are color pigments made of inorganic complexes, and it can be produced by the calculations of a mixture of oxides, nitrates, acetates and even metal oxide at temperatures above 1000°C. They reflect the wavelengths in the infrared region besides selectively reflecting some visible light. The particle size of pigments plays an important role in the NIR reflectance. Pigments possessing smaller particles or nanoparticles significantly improve the reflective properties. For roof and building, IR reflective pigments are usually used because of their excellent weatherability. Certain grades also have the capability to maximize reflectivity in the near infrared region. These IR-reflective pigments s are widely used as formulators make an effort to produce dark coatings and minimize heat buildup in the underneath structure [Figure 1.2].

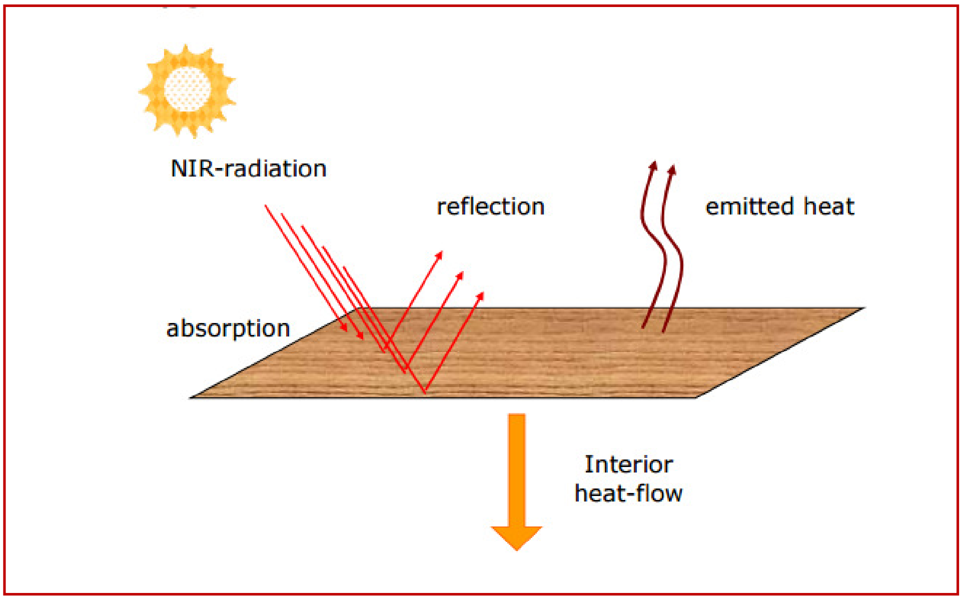

Figure 1.2 Interaction of NIR radiation with a pigmented surface.

In urban areas, the design of roofs also affects the heat absorption of sunlight. These hot buildings emit heat and warm the air in the surroundings. If there are numerous such buildings in the surrounding area, the combined effect leads to a phenomenon known as ‘Urban Heat Island Effect’. The quantity of heat radiated in the surroundings varies depending on the roof construction, type, elevation and also the color of the coating used.

A roof with high solar reflectance and high thermal emittance remains cool in the sun, reducing demand for cooling power in air-conditioned buildings and tolerable for people to work and live in them. To reduce the growing demand for energy consumption for air conditioning, there is a need for cool roofs. Increasing the solar reflectance lowers the amount of energy absorbed by the building. In turn, this decreases the heat penetrating into the building, especially during summer, resulting in more comfortable thermal conditions if the building is not air-conditioned [10, 11]. Pigment industry has realized the potential of these pigments and the cool-colored paints can be employed as an alternative.

1.8 Basic Concepts of Color

The Color is a sensation that gives excitement and emotion to our lives. Color vision is based on a variety of physical-chemical and physiological and psychological process. Color comes from an interaction between light, object, and the observer. Wavelength lies in the 400 - 700 nm region of the electromagnetic spectrum is visible to the human. Materials can be absorbed light completely or partially. The portion of the unabsorbed light can still be reflected at the surface of the object or transmitted through them. Which color is perceived depends on the composition of wavelengths in the light. If the sensors detect all visible wavelengths at once, the perceived color is white. If the object fully absorbs all wavelengths of the light, the brain perceives black. In colorants, the physical concepts of light absorption and reflection are essential for understanding the correlation between chemical structure and light absorption. Chromatic colors are produced when the object selectively absorbs or reflects the light of a particular wavelength. This will lead to the formation of absorption bands with typical maxima and minima in the absorption spectrum. If an object absorbs light in the 400 - 430 nm regions, the new reflected light spectrum that is the complement of the absorbed light creates the appearance of a color.

Table 1.2 Relationship between color and wavelength of monochromatic light.

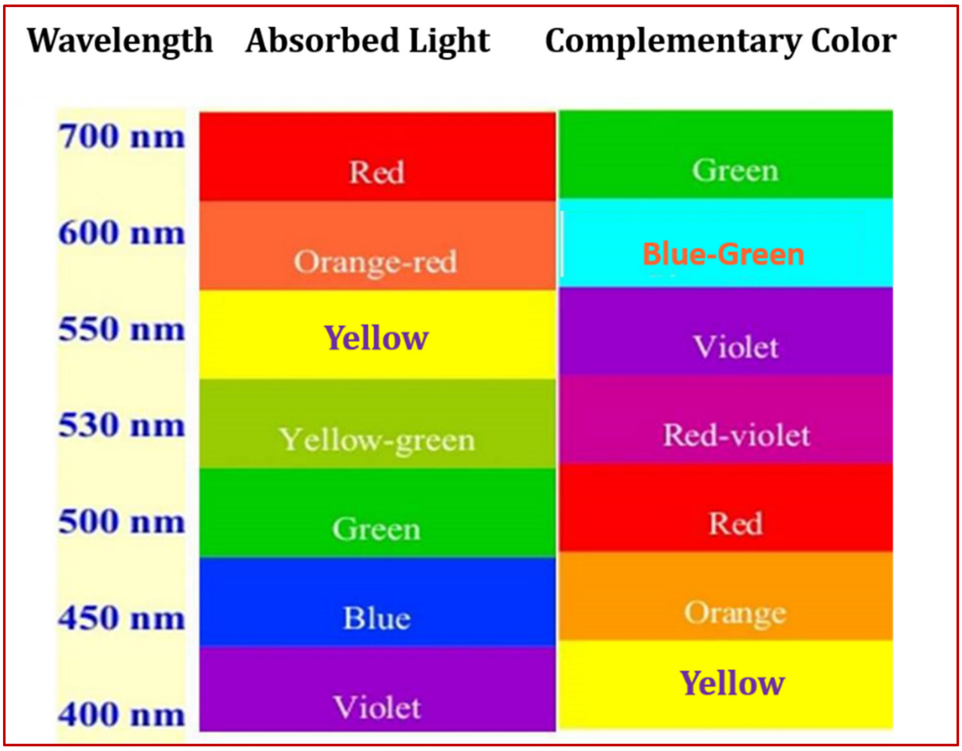

Wavelength	Absorbed Light	Complementary Color
700 nm	Red	Green
600 nm	Orange-red	Blue-Green
550 nm	Yellow	Violet
530 nm	Yellow-green	Red-violet
500 nm	Green	Red
450 nm	Blue	Orange
400 nm	Violet	Yellow

1.9 Color Systems

In our basic color wheel, there are three primary colors of light; red, green, and blue. Those can then be mixed into the three secondary colors of light; yellow, magenta and cyan. The full range of possible colors can be obtained by varying the amount of each color, or mixing in slight amounts of the third primary color. Available color systems are dependent on the medium with which a designer is working. While painting, an artist has used a variety of paints and mixed colors are attained through the subtractive color method. When a designer is utilizing the computer to generate digital media, colors are achieved with the additive color method.

1.9.1 *CMY and CMYK— the Subtractive Primaries*

In subtractive color mixing, one begins with white and ends with black; as one adds color, the result gets darker and tends to black [Figure 1.3]. The subtractive color method is used when we mix colors using paint or in the printing process. Cyan is directly opposed to red; magenta is the opposite of green and yellow is the opposite of blue in the visible spectrum. If cyan, magenta, and yellow pigments are placed on a white substrate, each completely absorbs or subtracts its opposite counterpart from the incoming white light.

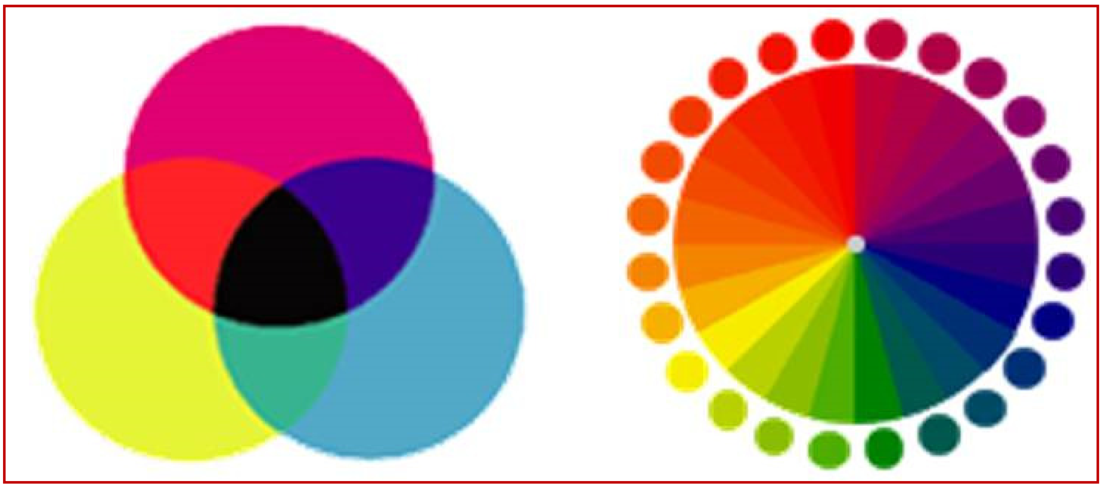

Figure 1.3 The CMYK color system—the subtractive color method.

1.9.2 *RGB— the Additive Primaries*

Additive color mixing begins with black and ends with white; as more color is added, the effect is lighter and tends to white [Figure 1.4]. The colors that see on the computer screen, televisions, and mobile phones are created with light using the additive color method. They begin with black and add red, green, and blue light to create the spectrum of colors.

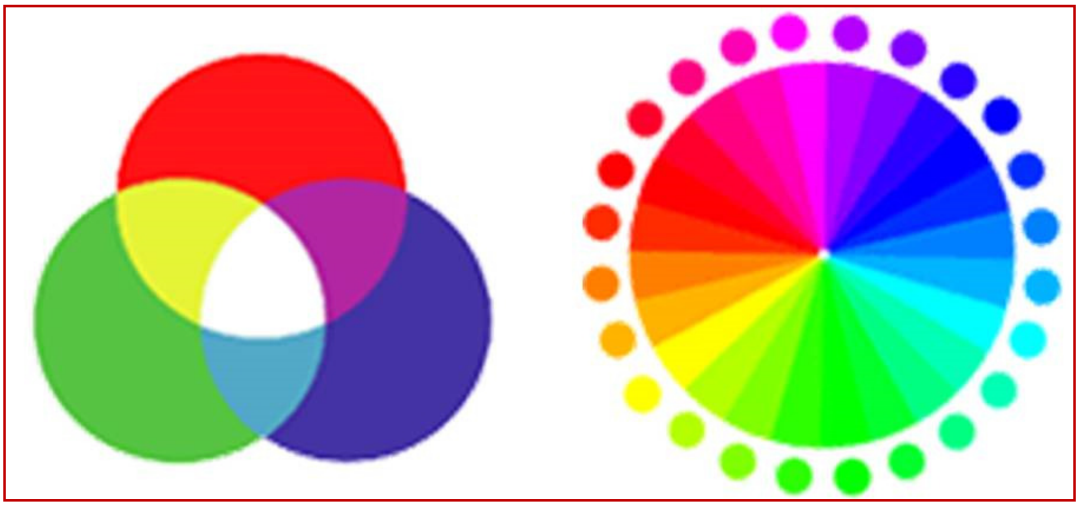

Figure 1.4 The RGB color system—the additive color method

1.10 The Dimensions of Color

Generally, we use simple names such as red, yellow or blue for referring colors. But not all yellow or blues look the same. Some are lighter or darker and some seem richer, or more color-full. If asked what color a particular object, it is more than likely that four different people would describe it in four different ways, so it would be difficult to describe the color with words. This problem has been solved by breaking down color into three basic components; hue, saturation and value.

Hue

Hues are colors and color we see is dependent on which wavelength of light being reflected or transmitted. Hue is one of the most important characteristics of a color. There is an infinite number of possible hues, for example, orange, yellow, green, cyan, blue and violet together with the non-spectral colors like magenta saw when the two ends of the spectrum are mixed. Similarly, there is a range of hues between any other two hues.

Saturation

Saturation describes the purity (intensity) of a color. Highly saturated colors look rich and full. Low intensity colors look dull and grayish. A pure color is 100% saturated, means there's no addition of gray to the hue. A hue with 0% saturation comes out as a medium gray. A more saturated (closer to 100%) hue appears as vivid or brighter.

Value

Value commonly used for describing the lightness or darkness of a color. All high saturation colors have a medium lightness (light and dark colors are achieved by mixing with white or black). The value defines the relative degree of black or white when it is mixed with a given hue. A color can lighten or darken by varying its lightness value and effect of lightness depends on the other values in the composition.

1.11 Colorimetry

Colorimetry is the science of color measurement, which is generally used to measure color differences between samples and it is employed in commerce, industry and the laboratory to express color in numerical terms. The important colorimetric applications include paints, inks, plastics, textiles, pharmaceuticals, and products that reflect or transmit color. Human color perception varies widely and is influenced by illumination, sample size, surrounding color and the angle of observation. Colorimetric instruments give a set of standardized conditions that assure consistency and reproducibility.

In colorimetry, the quantification of color is based on the three-component theory of color vision, which states that the human eye possesses receptors for three primary colors (red, green and blue) and that all colors are seen as mixtures of these primaries. In colorimetry, these components are referred to as X-Y-Z coordinates. The X-Y-Z tristimulus values are useful for defining colors; they do not allow easy visualization of color. Thus, a number of mathematical models and graphing methods have been developed under the auspices of the Commission Internationale de l'Eclairage (CIE). These conceptualizations are referred to as color spaces.

Basically, a color space based on hue, saturation and lightness uses cylindrical coordinates [Figure 1.5]. Lightness is the center vertical axis and saturation is the horizontal axis that extends from the lightness axis. Hue is the angle at which the saturation axis extends from the lightness axis. We can apply the relationship between wave attributes and color attributes to a three-dimensional color space. Wave amplitude determines a color's position on the lightness axis. Wave purity determines its location on the saturation axis and wavelength determines hue angle. Color space can be used to describe the range of visible or reproducible colors of a viewer or device. This three-dimensional format is also a very convenient way to compare the relationship between two or more colors. This standard way of giving a set of measurable color values to a sample means it is possible to directly compare colored materials.

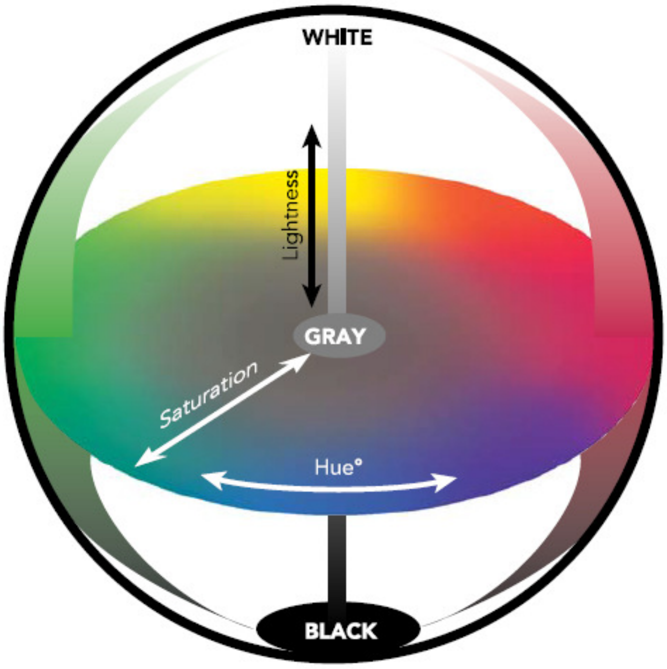

Figure 1.5 The concept of color space**.**

The RGB color model cannot be used as a standard for colorimetric measurement, because it is not repeatable. For a set of standard colorimetric measurement scales, we turn to the well-known work of the CIE—the Commission Internationale d'Eclairage [12]. The principles of colorimetry are based on the fact that all color stimuli can be simulated by additive mixing of only three selected color stimuli (trichromatic principle) [13, 14]. A color stimulus can also be produced by mixing the spectral colors. Thus, it has a spectral distribution, which in the case of nonluminous, perceived colors is called the spectral reflectance $\rho(\lambda)$. After defining three reference stimuli, the trichromatic principle allows a three-dimensional color space to be built up in which the color coordinates (tristimulus values) can be interpreted as components of a vector.

CIE Standard Illuminants

Defining the properties of the illuminant is an important part of describing color in many applications. The CIE's standards provide a universal system of pre-defined spectral data for several commonly used illuminant types. In 1931, the CIE established a set of three standard illuminants and they are identified as A, B, and C:

- Illuminant A represents incandescent lighting conditions with a color temperature of about 2856° K;
- Illuminant B represents direct sunlight at about 4874° K; and
- Illuminant C represents indirect sunlight at about 6774° K.

Later the CIE added a series of D illuminants, a hypothetical E illuminant, and a series of F illuminants. The D illuminants represent different daylight conditions. D50 and D65 are two such illuminants generally used as the standard illuminants for graphic arts viewing booths ("50" and "65" refer to color temperatures 5000° K and 6500° K, respectively)[Figure 1.6].

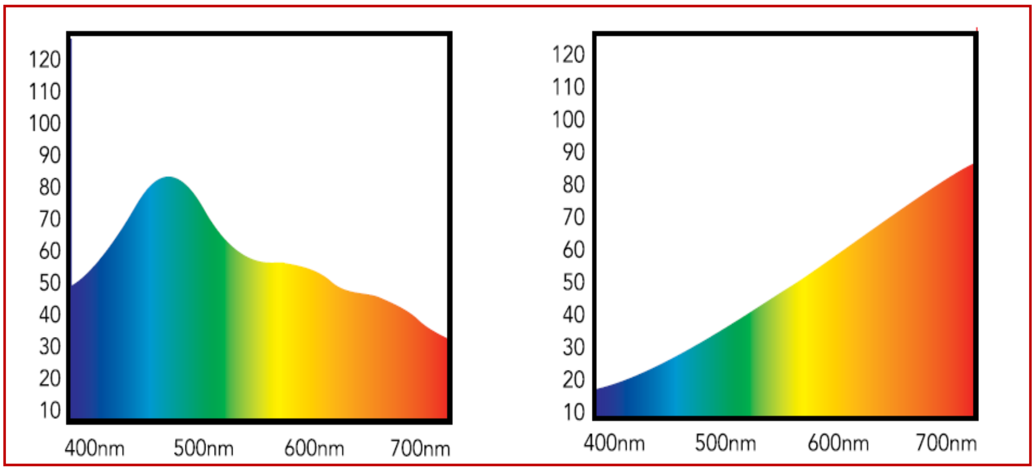

Figure 1.6 a) Bluish day light reflectance b) warm incandescent reflectance**.**

1.12 CIE Color Systems

In 1931, the CIE created standards for a series of color spaces that correspond to the visible spectrum. Using the CIE color model we can compare the varying color spaces of different viewers and devices against the standard observer. The CIE color systems are similar to the other three value models they utilize three coordinates to locate a color in a color space. However, the CIE spaces which include CIE XYZ, CIE $L^*a^*b^*$ and CIE $L^*u^*v^*$are device independent meaning the range of colors that can be found in these color spaces is not limited to the rendering capabilities of a particular device or the visual skills of an observer.

1.12.1 *CIE XYZ*

The CIE 1931 RGB color space and CIE 1931 XYZ color space were created by the International Commission on Illumination (CIE) in 1931[15, 16]. They resulted from a series of experiments done in the late 1920's by William David Wright [17] and John Guild [18]. The CIE XYZ color space encompasses all color sensations that an average person can experience. That is why CIE XYZ (Tristimulus values) is a device invariant color representation [19]. The resulting tristimulus values are defined by the CIE 1931 color space in which they are denoted *X*, *Y*, and *Z* [20].

The three CIE tristimulus values depend on the spectral reflectance ρ(λ) and the spectrum of the illuminant S(λ) as follows

$$X = \int_{400}^{700} \bar{x}(\lambda)\rho(\lambda)S(\lambda)d\lambda \tag{1.1}$$

$$Y = \int_{400}^{700} \bar{y}(\lambda)\rho(\lambda)S(\lambda)d\lambda \tag{1.2}$$

$$Z = \int_{400}^{700} \bar{z}(\lambda)\rho(\lambda)S(\lambda)d\lambda \tag{1.3}$$

The CIE's color matching function $x(\lambda)$, $\overline{y(\lambda)}$ and $\bar{z}(\lambda)$ and are the numerical descriptions of the chromatic response of the observer. They can be thought of as the spectral sensitivity curves of three linear light detectors yielding the CIE tristimulus values *X*, *Y* and *Z*. Collectively, these three functions are known as the CIE standard observer [Figure 1.7] [21].

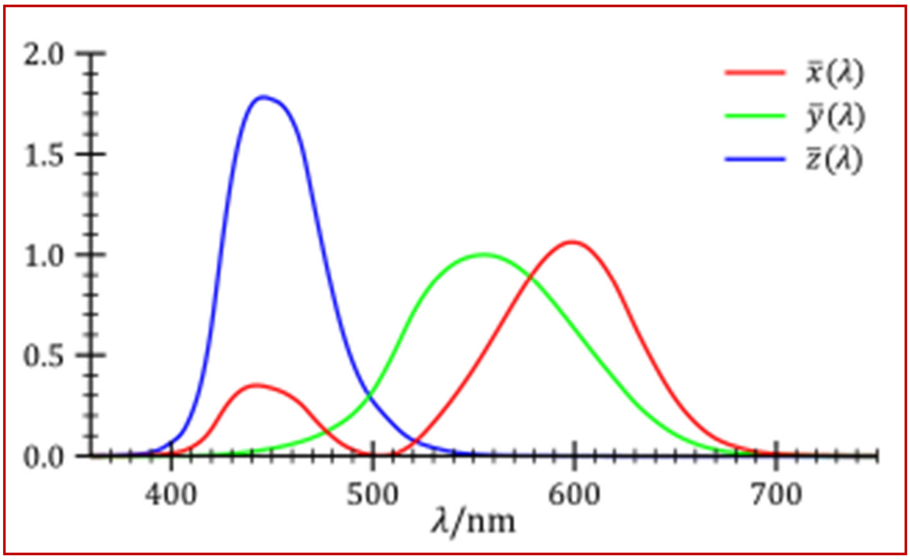

Figure 1.7 The CIE standard observer color matching functions.

The CIE chromaticity coordinates (x, y and z) are given by

$$x = \frac{X}{X+Y+Z} \tag{1.4}$$

$$y = \frac{Y}{X+Y+Z} \tag{1.5}$$

$$z = 1 - x - y \tag{1.6}$$

They are represented as coordinates in a color plane. The chromaticity coordinates x and y are used to specify the saturation and hue of any color in the CIE chromaticity diagram. The CIE spectral tristimulus value y (λ) corresponds to the lightness sensitivity curve of the human eye. In addition to x and y a third color variable issued, namely the CIE tristimulus value Y, which is a measure of lightness. This system allows exact measurement of color with the worldwide agreement. For pigment evaluation, this is not adequate because small color differences between test and reference pigment have to be determined. Using the CIE system, we can say which spectral distributions are visually identical, but this is not appropriate for measuring the color differences. Color differences can be measured by using an absolute color space; here the colors are arranged three dimensionally. The distances between two colors in any direction in color space correspond to the perceived difference. This type of color space can be based on the color attributes such as lightness, hue and saturation. The transformation, relationships between the CIE system and the physiological equidistant color system must be established for the quantitative determination of color differences.

1.12.2 *CIE $L^*a^*b^*$*

The color space CIE $L^*a^*b^*$ (CIELAB) is established by the International Commission on Illumination. The CIE color systems describe all the colors visible to the human eye and the varying color spaces of different viewers and devices against repeatable standards are compared. Since the $L^*a^*b^*$ model is a three-dimensional model, it can be represented properly only in a three dimensional space [22]. The ultimate goal of the CIE was to develop a repeatable system of color communication standards for manufacturers of paints, inks, dyes and other colorants. These standards' most important purpose was to provide a general framework for color matching. The standard observer and XYZ color space were the foundations of this framework; however, the unbalanced nature of the XYZ space as demonstrated by the xyY chromaticity diagram made these standards difficult to clearly address. The well-balanced structure of the $L^*a^*b^*$ color space is based on the theory that a color cannot be both green and red at the same time nor blue and yellow at the same time. As a result, single values can be used to describe the red/green and the yellow/blue attributes. In CIE $L^*a^*b^*$ color space, L^* describes lightness; a^* denotes the red/green value and b^* the yellow/blue color. This color spaces be similar to three dimensional color spaces like HSL. The three coordinates are denoted by a^* (the red-green axis), b^* (the yellow-blue axis), and L^* (the lightness axis). Figure 1.8 shows the simple representation of the CIELAB system. To calculate the CIELAB coordinates, X, Y and Z are first converted into the functions X^*, Y^* and Z^*.

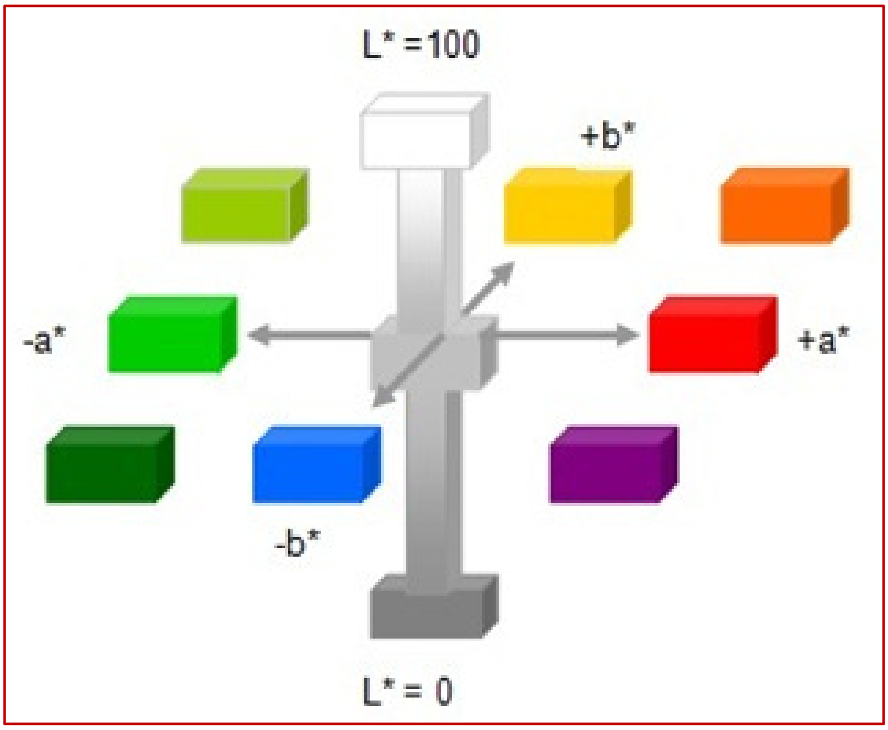

Figure 1.8 Representation of the CIELAB system.

$$X^* = \sqrt[3]{X/X_n} \tag{1.7}$$

$$Y^* = \sqrt[3]{X/Y_n} \tag{1.8}$$

$$Z^* = \sqrt[3]{X/Z_n} \tag{1.9}$$

Where X_n, Y_n and Z_n are the CIE tristimulus values of the illuminant especially a standard illuminant. For radicands ≤0.008856, these equations become:

$$X^* = (7.787X/X_n) + 0.138 \tag{1.10}$$

$$Y^* = (7.787Y/Y_n) + 0.138 \tag{1.11}$$

$$Z^* = (7.787Z/Z_n) + 0.138 \tag{1.12}$$

Values of a^*, b^*, and L^* are obtained from the values of X^*, Y^*, and Z^*:

$$a^* = 500(X^* - Y^*) \tag{1.13}$$

$$b^* = 200\,(Y^* - Z^*) \tag{1.14}$$

$$L^* = 116\,(Y^* - 16) \tag{1.15}$$

The components of the color difference are obtained as differences between the test sample (T) and the reference pigment (R):

$$\Delta a^* = a_T^* - a_R^* \quad (1.16)$$

$$\Delta b^* = b_T^* - b_R^* \quad (1.17)$$

$$\Delta L^* = L_T^* - L_R^* \quad (1.18)$$

Measurement of the difference in color between two objects is one of the most complicated aspects of color vision. For colorant users like textile, leather, and paper or paint industries the difference in color of two specimens namely a standard and a sample or of different portions of a colored specimen may be more important than the measurement of absolute color [23]. The prime difficulty is that the perception of color difference by an individual is not a precise phenomenon and may vary on successive assessment [24]. The geometrical distance between the two positions in the CIELAB color space gives the color difference:

$$\Delta E_{ab}^* = \sqrt[2]{(\Delta a^{*2} + \Delta b^{*2} + \Delta L^{*2})} \quad (1.19)$$

An important advantage of the CIELAB system is that the resulting color difference can be split into component contributions, namely lightness, saturation and hue, corresponding to the arrangement of the color space:

Chroma difference (saturation difference)

$$\Delta C_{ab}^* = \sqrt{a_T{}^{*2} + b_T{}^{*2}} - \sqrt{a_R{}^{*2} + b_R{}^{*2}} \quad (1.20)$$

$$\Delta H_{ab}^* = \sqrt{\Delta E_{ab}{}^{*2} - \Delta L^{*2} - \Delta C_{ab}{}^{*2}} \quad (1.21)$$

The CIE 1976 (L*u*v*) color space maintains the same L^* as $L^*a^*b^*$ but its chromaticity components are a different representation. CIELAB and CIELUV can also be represented in cylindrical form with the chromaticity components are changed by correlates of chroma and hue. Since CIELAB and CIELUV the CIE has been including more number of color appearance models, to better model color vision.

1.13 Kubelka-Munk Theory

Kubelka and Munk had done a simplified analysis of the interaction of incoming light with a layer of paint. The material is assumed to be uniform, isotropic, non-fluorescent and non-glossy and the sample has to be illuminated by diffuse, monochromatic light. In paper industry K-M model has been widely used due to its simple use and its adequate prediction accuracy. This model is extensively used for multiple scattering calculations in the paint, paper, plastic and textile.

In the Kubelka-Munk theory, optical properties of a film which absorbs and scatters light may be explained by two constants. The absorption coefficient K and the scattering coefficient S. The Kubelka-Munk theory assumes that all incidents and scattered light are perfectly diffuse and they considered the light transport in only two opposite directions. The intensity of the light is assumed to vary along one axis only. Such two- flux approximations have been presented by many authors starting with a paper by Schuster [25]. In 1931 Kubelka and Munk presented one of the most famous two-flux approximations [26] and further developed by Kubelka [27, 28]. Kubelka and Munk provided a comprehensive formulation and it was quickly adapted the papermaking industry [29-32]. Now, this has been widely used in the measurement and calculation of color brightness and opacity of paper sheets.

Kubelka and Munk proposed a system of differential equations based on the model of light propagation in the dull colored layer that is parallel to a planar substrate. They assumed that the incident reflected and transmitted intensities are perfectly diffuse and are dispersed either upwards or downwards direction. The reflectance of the medium is denoted as R and its transmittance is T. The sample is in optical contact with an obscure substrate with reflectance R_g and is split into a series of layers with equal thickness. That layer gets a flux i traveling downward and flux j moving upward and the reflectance being j/i. These fluxes are changed by passing from one layer to the next. According to the Beer-Lambert law without scattering the change in irradiance of the flux of light in the downwards would be $dI = -K\,dx$. Kubelka and Munk suggested that like absorption scattering is also a first order phenomenon. The flux in down direction i has a positive value when the flux is going down. According to Kubelka-Munk sign conventions, j is used for describing the flux of light in the up direction and its value of being positive when the light is going up. The term describes that the up moving flux is scattered to add to the down moving flux. The first order differential equation is expanded to include two other terms. A simple system of two linked differential equations can be written. These can be integrated for the valid boundary conditions at the incident light side and on the opposite side. Solutions for the transmittance T and the reflectance R are obtained from these integrals as a function of the absorption coefficient K, the scattering coefficient S, the film thickness h and in special cases of the reflectance R_g of a given substrate. Kubelka-Munk theory provided by a very simple equation for measuring the reflectance of an opaque (infinitely thick) film that is:

$$\frac{K}{S} = \frac{(1-R_\infty)^2}{2R_\infty} \tag{1.22}$$

The term R_∞ represents s the reflectance of the infinitely thick sample. The equation has been most useful where reflectance measurements are used to obtain information about absorption and scattering. This theory is especially useful for computer color matching of pigmented system's absorption and scattering coefficients are combined additively using the specific coefficients of the components multiplied by their concentrations.

1.14 Multiple Scattering

In the optical analysis of collections of particles surrounded in a matrix, prediction of optical properties of the final film, given the optical characteristics of the materials of which it is made, the particle size, and the fraction of the volume occupied by the particles. The first task is to make connections between the optical properties of the bulk materials of which the particles and medium and the spatial distribution of the scattered intensity of the individual particles. The multiple-scattering function also accounts for the differences in diffuse reflection observed in films of identical volume fraction occupied by particles (particle volume concentration) but different grinding time. This method of analysis begins to allow one to make an explicit connection between the fundamental optical properties of the particles and the experimentally accessible parameters. The method provided a way to begin to bridge the gap between the light scattering from individual particles and the practical characterization of a film using the Kubelka-Munk model. The absorption coefficient K obeys the Beer’s law and it is proportional to (even at high pigment volume concentrations. The relationship between the scattering coefficient S and the concentration gives rise to problems, however. As the pigment, concentration increases the distance between the pigment particles decreases. As a result of this, there are interactions and hindrance between the light scattered by individual particles and their scattering power falls. The scattering coefficient S linearly related to concentration only at low concentration at higher concentrations it remains below the linear value. The concentration dependence of the scattering coefficient can be quantitatively represented by using empirical formulae, e.g., there is a linear relationship between S/σ and $\sigma^{2/3}$.

1.15 Mie's Theory

The exact analytical solution of Maxwell's equations for the scattering of an electromagnetic wave from a single sphere was first presented by Gustav Mie in 1908 [33]. Mie theory is very important in the characterization of particles via optical scattering measurements. This theory is helpful for understanding the appearance of materials such as milk, biological tissue and latex paint. The matter is composed of discrete electric charges such as electrons and protons. When light is incident on a particle these charges are set into oscillation where the net effect is manifested in the emission of secondary radiation known as scattering. In addition to scattering part of the incident radiation is absorbing ie: having a complex index of refraction. Hence scattering and absorption lead to the temporal implication of reduction of the incident light after traversing a particle. The net effect of radiation extinguished from the incident radiation is termed extinction. In general two main formulations for handling the particle light interactions are Mie theory and ray optics. In Mie's theory, the electromagnetic wave concept is employed and Maxwell equations are used in the derivation of the incident, scattered and internal fields. Mie applied the Maxwell equations to a model in which a plane wave front meets an optically isotropic sphere with refractive index n and absorption index k. The values of the absorption cross section Q_A and the scattering cross section Q_S are obtained by integration. These dimensionless numbers relate the proportion of absorption and scattering to the geometric diameter of the particle. The theory has provided useful insights into the effect of particle size on the color properties of pigments. In addition the effect of particle geometry, particle index with respect to the surrounding medium and the angular dependence of the incident beam can be studied of particular interest is the feature of structural or morphological dependent resonance where particle resonance is generated by varying the size parameter which is defined as

$$\chi = \frac{2\pi a N_m}{\lambda} \tag{1.23}$$

a denotes the radius of a particle and λ/N_m represents the wavelength in the surrounding medium of index N_m. Mie theory remains the most complete and reliable model with its applicability extended over the entire range of particle size. The Mie calculations assume a spherical particle. The fact that pigment particles are not perfect spheres has been shown by finite-element calculations of scattering from particles of realistic shapes to cause variations in the scattering parameter [34].

1.16 Causes of Color

Nature of color has been discussed with respect to the three components of color production and the molecular basis of light modification by colored compounds. Among the colored materials taken from living things are chlorophyll from green plants and hemoglobin from the blood. The world of minerals and gems is full of color. Many of the materials that are used as artists' colors consist of these inorganic materials [35]. Most of the compounds of an element of the d block (transition elements) exhibit color [36] this fact suggests that certain structural features might be responsible for the observed colors. Substances exhibit color, because they are capable of absorbing selected wavelength ranges of white light. The absorbed light promotes the electrons within these species to higher energy levels. Such transitions lead to changes in the colors observed. Changes in energy level differences are fundamentally environmental changes, the atoms in the species are sensitive to the forces surrounding them so that virtually any change in the atoms electronic environments will produce color changes. This is a working principle, which we can use to examine the origin of color in numerous substances.

1.16.1 *Color due to Crystal Field Transitions*

Light absorption by the electrons of transition metal atoms is one of the most important and well known of the coloring mechanisms [37-39]. Numerous artists' pigments exhibit color due to crystal field transitions. Among them are manganese pyrophosphate ($MnNH_4P_2O_7$); chromium oxide green (Cr_2O_3); Thenard's Blue ($CoAl_2O_4$); smalt ($K_2CoSi_4O_{10}$) etc. The color of many minerals and gems such as emerald, ruby, olivine, turquoise, azurite and malachite are the result of these transitions. The presence of small quantities of transition metal ion in gemstones is the main reason of their color [40].

These transition metal ions have incompletely filled d-orbitals. When white light passes through a colored gemstone some part of the visible light energy is absorbed. Because of this light absorption, d electrons in the transition metal ion experience an energy change. The transmitted or reflected visible light that appears colored because those colors corresponding to 3d-electron energy transitions have been absorbed. Pure corundum is colorless but in ruby a brilliant color result from the substitution of chromium ions (Cr^{3+}) for a few percent of the aluminum ions. In ruby, the coordination environment around the Al^{3+} ion and Cr^{3+} ion is an octahedron. Here each Al^{3+} ion and the Cr^{3+} ion is surrounded by six oxide ions. In the octahedral environment, five 3d orbitals of Cr^{3+} split into two sets, the d_{xy}, d_{xz}, d_{yz} orbitals and the $d_{x^2-y^2}$ and d_{z^2} orbits and they have different energies. When visible light strikes the ruby, the gem absorbs light energy required for the transition of an electron from the lower-energy orbital to the high-energy set. The energy difference between the low and high energy orbitals corresponds to the energy of visible light. The ruby reflects or transmits the remaining part of the light. The observed color is the complementary color of the absorbed light.

The origin of color in the gemstone emerald is similar to that of the color of ruby. In emerald, the green color is produced by the presence of chromium (III) ions in the crystal. In emeralds, the Cr^{3+} is coordinated by six silicate ions rather than the oxide ions in ruby. These silicate ions also split the 3d orbitals of Cr^{3+} into two sets. However, the magnitude of the energy difference between the sets is different from that produced by the oxide ions in ruby. That is why ruby and emerald exhibits red and green colors [Figure 1.9].

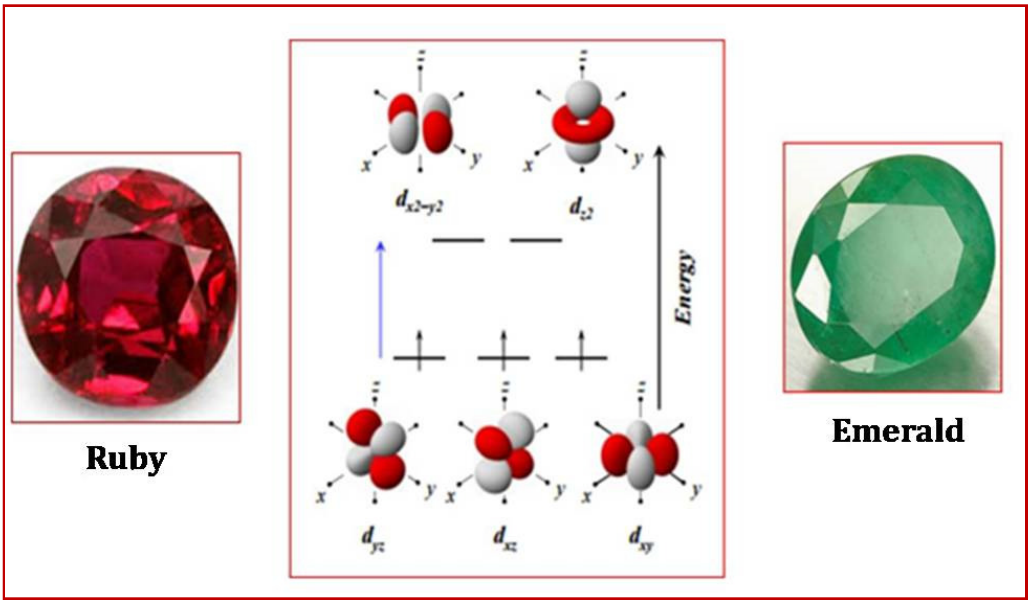

Figure 1.9 Color due to crystal field transitions.

1.16.2 *Color due to Charge Transfer*

1.16.2.1 Ligand to metal charge transfer

The color arising from crystal field transitions is sometimes striking and brilliant; they are not as intense as the colors of pigments like chrome ($PbCrO_4$) or antimony vermillion (Sb_2S_3). However, in neither of these cases does the metal undergo crystal field transitions, because it does not meet the incompletely filled d-orbitals requirement. Such compounds are said to exhibit color due to charge transfer transitions. Charge transfer can occur when two atoms in close proximity to one another have energy levels and absorption of electromagnetic radiation can result in the promotion of an electron from the highest occupied orbital of the donor to the lowest unoccupied orbital of the acceptor species. Such a transition results in the formation of an ionic structure, (D+-A-), and if the energy required for the transition is of the order of the energies of visible light, then the color will be seen. Some examples of such transitions in artist's pigments are the following:

$$\text{Chrome Yellow: } PbCr^{6+}O_4^{2-} \rightarrow PbCr^{5+}O^{-}O_3^{2-} \qquad (1.24)$$

In this case, the charge transfer transition occurs between the metal and ligand atoms. In yellow chromate K_2CrO_4, oxygen to chromium charge transfer occurs. The effect of ligand fields can be ignored as there are no unpaired electrons in the chromium (Cr^{6+} cation). The chromium cation will have a strong attraction for electrons from the oxygen anions allowing a ligand to metal (anion to cation) electron transfer [Figure 1.10]. Other examples of this are the orange dichromate ($K_2Cr_2O_7$), permanganate salts and chrome yellow ($PbCrO_4$).

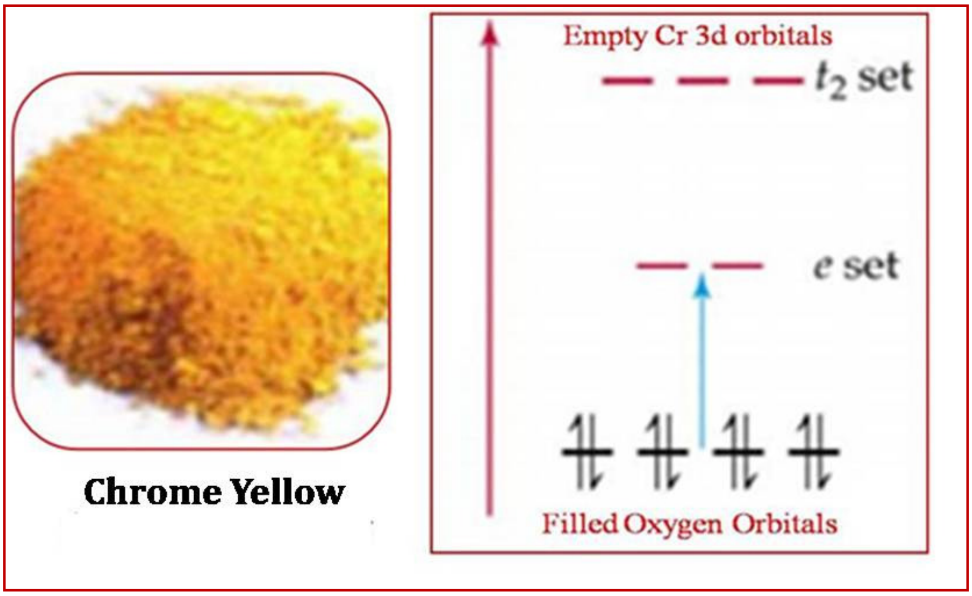

Figure 1.10 Ligand to metal charge transfer transitions.

1.16.2.2 Intervalence charge transfer

The term intervalence charge transfer is used for describing the metal to metal charge transfer between nonequivalent metal centers [41]. Corundum is Al_2O_3 based compound that contains a few percent of titanium is colorless. If a small percent of iron adds, it gives a very pale yellow. If impurities such as titanium and iron are present together, the result is a brilliant blue color. The process of intervalence charge transfer generates a strong colored appearance at a low percentage of impurities. This occurs because there is enough overlap between the outer orbitals of Fe^{2+} and Ti^{4+} to allow an electron to pass from one ion to another. The substitution of Fe^{2+} and Ti^{4+} ions for Al^{3+} creates charge imbalances in the compound. In corundum, the occupation of Fe^{2+} and Ti^{4+} ions in the adjacent sites cause the transfer of an electron from the iron cation to the titanium cation [Figure 1.11]. This process will change the valence state of both Fe^{2+} and Ti^{4+} ions. This process requires energy; this energy jump is comparatively easy for electrons to achieve when light shines on the crystal.

$$Fe^{2+} + Ti^{4+} \rightarrow Fe^{3+} + Ti^{3+} \tag{1.25}$$

According to quantum considerations, charge transfer transitions are strong because they are allowed transitions. Sapphires undergo heteronuclear charge transfer as electrons are transferred between ions of different elements.

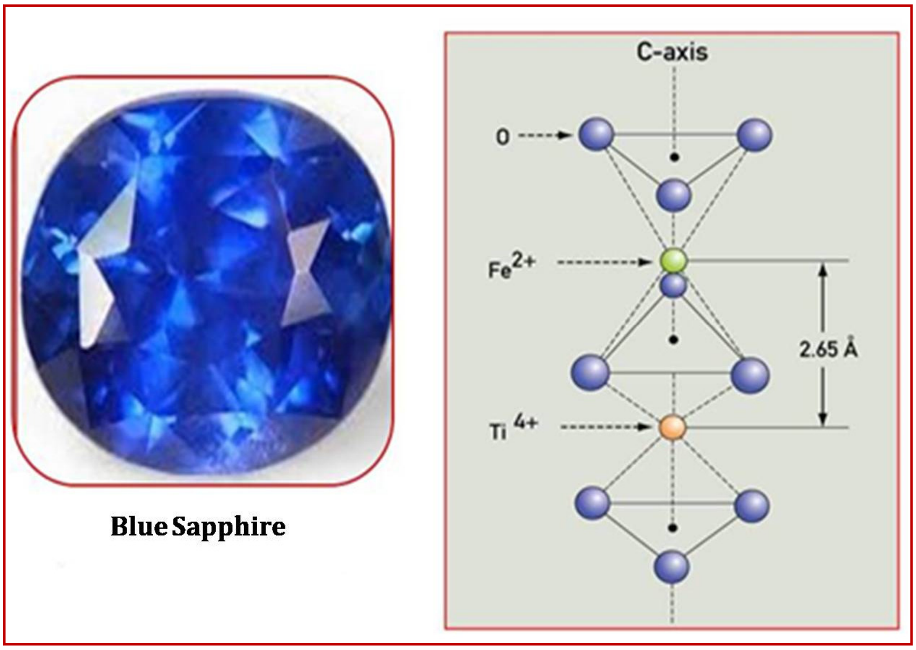

Figure 1.11 Two adjacent octahedral sites containing Fe^{2+} and Ti^{4+} in sapphire.

1.16.3 *Color due to Valence Band to Conduction Band Transitions*

The mechanism behind the color we observe in semiconductors can be explained by the band theory. In the formation of crystalline or semi-crystalline materials, numerous atoms with only definite allowed energies are arranged in such a way as to multiply the number of allowed energy states. The electrons of a single isolated atom occupy atomic orbitals, in which each orbital form at a discrete energy level. When two atoms join together to form a molecule, their atomic orbitals overlap [42]. As more atoms are coming closer together, their distinct energy levels overlap. As the number of neighboring atoms increases, the low energy levels overlap and the high energy levels overlap and bands of low and high energy levels are formed. These states are so closely spaced that a collection of such states is often referred to as a band and the spacing between the bands is called the band gap. The part of the band below the band gap is called the valence band and this part contains electrons. The portion of the band located above the gap is called the conduction band and are generally empty because electrons excited to this level. When light strikes the surface electrons in a lower energy level can be excited to a higher energy level. The distance between the levels represents the relative energy required to excite an electron. In metals, electrons are re-emitted readily, but in semiconductor, absorption is dominant over re-emission because here electrons are not being re-emitted readily or immediately. If the band gap falls within the visible region, the crystal will absorb visible light and exhibit color. Many semiconductor crystals such as HgS, AgI, CuBr and ZnSe have band gaps between 1.7 and 3.1 eV, and are colored because of band transitions. Vermillion (HgS) and cadmium yellow (CdS) are two prominent inorganic pigments they owe its color due to their semiconductor behavior [Figure 1.12] [43]. In cadmium yellow, the band gap is 2.6 eV, which energy permits the absorption of violet and some blue and we see it as a yellow color. Closely spaced energy levels in the conduction band; semiconducting crystals will absorb all wavelengths of electromagnetic radiation equal to and greater than the band gap energy.

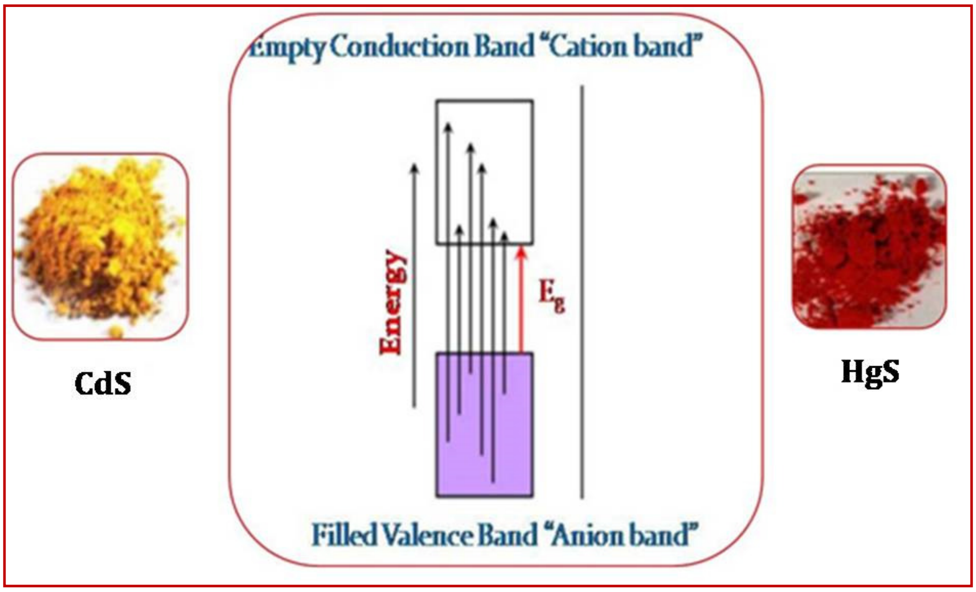

Figure 1.12 Valence band to conduction band transition.

1.17 Research Efforts in Co and Mn Based Blue Pigments and Cu Based Green Pigments

The presence of first row transition metal cations such as V, Cr, Mn, Fe, Co and Cu is known to be a source of color in many minerals and to be responsible for the absorption of near infrared and visible light [44]. Absorption properties are strongly related to the local environment of the cation and electronic transition associated with the cation occupying a crystallographic site in the compound.

1.17.1 *Cobalt Based Blue Pigments*

Blue is a cool and calm color and it is the color of creativity and intelligence. It is the color of the sky and the sea and is commonly used to represent these images. Among the three primary colors (red, green and blue) blue colored pigment quality materials are relatively very rare. Among the transition element, one of the great important elements is Co^{2+}, numerous Co^{2+} ($3d^7$) based oxides exhibit strong violet or blue coloration as well as a light pink hue and have been used as a pigment. The Co^{2+} ions can occupy four (tetrahedral), five (trigonal bipyramidal) and six (octahedral) coordinated site. In the tetrahedral coordination, the color is a deep blue ($CoAl_2O_4$), if the coordination number is six the hue changes to pink (Co_2SiO_4, $(Ca,Co)Si_2O_6$). There is a wide variety of historical cobalt pigments are available. Some of them are used for painting and others are often used for decorating ceramic objects or producing a ceramic glaze [45].

The first use of a Co-based pigment was mainly connected with glassware and porcelain in China [46], later it is employed in the form of dyes [47]. Uses of cobalt aluminate pigments in ancient Egyptian ceramics are also reported [48]. The first modern cobalt based pigment (cobalt green) is synthesized in 1780 and used as an artistic color until 1835 [49, 50]. Usually, cobalt in pigments is related to the blue hue, but the palette is very large: blue, green, yellow, violet, brown and black [51-53]. However, there are several environmental issues in the use of cobalt, at present research are enduring to minimize its use and to find phases highly stable to leaching [54, 55].

US patent No. 7,014,701 B2 provides inorganic pigments including cobalt and aluminum having the spinel crystalline structure that exhibits improved color and or weatherability in paint and polymer applications. Inorganic pigments according to the invention are formed by adding small quantities of a phosphate compound such as aluminium phosphate and chromium (III) oxide to a raw batch that includes a mixture of cobalt containing and aluminium containing inorganic pigment precursors and calcining the raw batch to obtain the inorganic pigment. The resulting inorganic pigment exhibits higher chroma values. The increased chroma due to the addition of phosphate mineralizer manifests itself as a more blue and more red pigment. The presence of Cr(III) oxide in the raw batch improved the UV absorption and has a lower pH [56].

Co doped willemite ($Co_{0.05}Zn_{1.95}SiO_4$) and with Mg doped Co-Al spinel ($Mg_{0.2}Co_{0.8}Al_2O_4$) pigments is prepared by the conventional ceramic route method. The coloring efficiency in different glazes of the Co-olivine blue pigment (Co_2SiO_4) has been compared with those obtained with a Co doped willemite and with Mg doped Co–Al spinel. The cobalt willemite composition contained a low amount of cobalt produced bluest hue of all pigments in both double and single firing glazes while the magnesium doped Co–Al spinel was found the most appropriate blue pigment in the bulk coloration fast fired porcelainized stoneware [57].

The Co-doped willemite ($Zn_{2-x}Co_xSiO_4$) pigments were synthesized using the sol-gel process. Synthesis these ceramic pigments by sol-gel method helpful for achieving high purity samples at relatively low temperatures. The materials were investigated by X-ray diffraction (XRD), IR spectroscopy, UV-visible spectroscopy, color measurements and scanning electron microscopy (SEM). Here they obtain a variety of colors (turquoise, purple, violet and blue) with a minimum quantity as possible as of cobalt. A various and intense blue color with a cobalt addition of 35 mol % was obtained [58].

Samples with compositions $Co_{2-x}Mg_xP_2O_7$ ($x = 0, 0.1, 0.2, 0.3, 0.5, 0.7, 1.0, 1.5$ and 1.8) have been prepared and characterized for the first time as an alternative low-toxicity blue ceramic pigments. The compositions were prepared through the conventional coprecipitation route and calcined up to 1000°C/2 h. Interestingly, the obtained solid solutions developed nice blue-violet color variations even with high Mg doping after enameling within double-firing ($x = 1.5 - 1.8$) and single-firing ($x = 1.0 - 1.5$) ceramic glazes. These optimal compositions containing a minimized amount of cobalt could be therefore less toxic alternatives to the conventional $Co_3(PO_4)_2$ blue ceramic pigment [59].

A novel blue colorant, based on the melilite structure has been developed by the search for a new crystal structure suitable to act as a blue pigment mainly in glazes rich in zinc and calcium. Five samples ($Ca_2Zn_{1-x}Co_xSi_2O_7$ with $x = 0.05, 0.1, 0.2, 0.3$, and 0.4) were prepared by a solid-state synthesis in industrial like conditions. Increasing cobalt doping gives rise to a gradual expansion of the hardystonite unit cell unexpected on the basis of Zn^{2+} and Co^{2+} ionic radii attributed to a change of the covalent character of M–O bonding. Optical spectra are dominated by the strong absorption bands of Co^{2+} in tetrahedral. The best compromise between cobalt concentration and the optical response was found to be around $x = 0.3$. The hardystonite pigment gives a deep blue color on glazes and glassy coatings withstanding aggressive media rich in CaO and ZnO better than industrial blue pigments (cobalt aluminate) with similar color efficiency than industrial blue dyes (cobalt silicate) [60].

1.17.2 *Manganese Based Blue Pigments*

Manganese is known to be essential for life, appearing in diverse biochemical roles ranging from noncatalytic binding and activation in lectins to water oxidation catalysis in the photosynthetic reaction centers of green plants. The atomic number of manganese is 25 and its outermost electronic configuration is [Ar] $3d^5 4s^2$. It exhibits several oxidation states, +2 to +7. Manganese has no satisfactory substitute in its major applications in metallurgy. Manganese compounds have been used as pigments and for the coloring of ceramics and glass. The brown color of ceramic is sometimes the result of manganese compounds. Larger quantities of manganese are used to produce pink colored glass. However, Manganese based blue pigments are very rare so there is growing need to develop new Mn based blue pigments.

Subramanian *et al.* reported Mn based highly stable blue inorganic pigments by the Introduction of Mn^{3+} into the trigonal bipyramidal sites of $YIn_{1-x}Mn_xO_3$. They have also shown that a blue color is obtained when Mn^{3+} is introduced into trigonal bipyramidal sites in other layered oxides. The blue color is a consequence of both the crystal field splitting associated with the trigonal bipyramidal coordination and the short apical Mn–O bonds. This result will lead to routes for the development of inexpensive, earth-abundant, environmentally benign, highly stable blue inorganic pigments [61].

Substitution of Mn^{3+} into the trigonal bipyramidal sites (TBP) of $ScAlMgO_4$, $ScGaMgO_4$, $LuGaMgO_4$, $ScGaZnO_4$, $LuGaZnO_4$ and $LuGaO_3(ZnO)_2$ with $YbFe_2O_4$ related structures produce an intense blue color because of an allowed d-d transition. There are relatively few examples of oxides where transition metal cations occupy TBP sites in oxides, and the $YbFe_2O_4$-type structure is one of the rare examples. The hue of the blue color can be controlled by the choice of the host [62].

$YIn_{1-x}Mn_xO_3$ blue pigments have been synthesized based on the pyrolysis at 600°C of aerosols generated from aqueous solutions of Y, In and Mn nitrates followed by an annealing treatment at 1100°C. This process requires a much lower temperature (1100°C) than that required by the traditional solid state method (1400°C). The amount of Mn introduced in the $YInO_3$ matrix has been varied in order to evaluate the effects of the Mn content on the color properties of the pigments. It has been found that blue color with the lowest Mn content is given by the formula $YIn_{0.9}Mn_{0.1}O_3$. The technological performance of these $YIn_{1-x}Mn_xO_3$ blue pigments has also been evaluated by testing their efficiency for coloring ceramic glazes of different composition [63].

A purple inorganic pigment, $YGa_{1-x}Mn_xO_3$ ($0 < x \leq 0.10$), based on hexagonal $YGaO_3$ was prepared by a sol gel technique. Where the dried gels obtained from aqueous solutions of metal nitrate citric acid mixtures, were calcined at 850°C. The purple color of the oxides arises from the crystal field splitting of Mn^{3+}in the trigonal bipyramidal site of the $YGaO_3$ host. Other hexagonal $RGaO_3$ hosts for R = Lu, Tm and Ho substituted with Mn^{3+} also produce similar purple colored materials [64].

A new inorganic blue chromophore series $Sr_2(Mg_{1-x}Mn_x)Ge_2O_{7+\delta}$ has been prepared by the solid state reaction method. As the content of Mn in the compound was increased, the color changed from white (for $x = 0.0$) to sky blue, deep blue, and black color (for $x = 1.0$). $Sr_2MgGe_2O_7$ has the melilite-type structure comprising $Mg(2+)O_4$ and GeO_4 tetrahedra. Mn ion in $Sr_2(Mg_{1-x}Mn_x)Ge_2O_{7+\delta}$ is mainly trivalent and that the additional oxygen atom gets into the lattice to compensate for the excess positive charge. The additional oxygen atom occupies an interstitial site, leading to the formation of $Mn(3+)O_5$ trigonal bipyramid and $Ge(4+)O_5$ square pyramid [65].

Nano blue pigment $YIn_{0.9}Mn_{0.1}O_3$-ZnO was synthesized by a sol-gel combustion method. The developed nano-pigment disclosed the existence of $YIn_{0.9}Mn_{0.1}O_3$ and ZnO in a 1:1 ratio with hexagonal crystal structures. The optical properties of $YIn_{0.9}Mn_{0.1}O_3$ synthesized by the sol-gel combustion route compared with that of $YIn_{0.9}Mn_{0.1}O_3$-ZnO. It is interesting to note that the developed

$YIn_{0.9}Mn_{0.1}O_3$-ZnO nano-pigment exhibits superior blue hue (b^* = -40.55) and solar reflectance (R^* = 70%) values as compared to the $YIn_{0.9}Mn_{0.1}O_3$ nano-pigment (b^* = -22.28, R^* = 50%). The present study reports on the development of a new inorganic nano-pigment with an intense blue color and high solar radiation (70%) [66].

1.17.3 *Copper Based Green Pigments*

Green is the color of balance and harmony and it is associated with the natural color of trees and has relaxing effects to ease tension. Vibrant colors were prized throughout the ancient world. Even today, we can still see the remains of pigments and dyes created by every major culture. Cu^{2+} is a chameleon in coordination chemistry it can occupy various coordination sites such as four, five and six. Depending upon the coordination and crystal field splitting they give a variety of colors. Cu^{2+} has an important role in the pigment industry, a lot of copper based green pigments are commercially available in the market.

Fine particles of green yttrium-barium-copper-oxide pigments Y_2BaCuO_5 have been prepared by Fernandez *et al.* using two different synthesis methods. The process of combustion of mixed nitrates and urea needs a maximal temperature of 900°C and provides samples formed by aggregates of homogeneous small particles with a size of about 0.3 µm. However, the ceramic method requires 1050°C as synthesis temperature and yields rather higher particle sizes. Even after grinding these samples are formed by heterogeneous particles with mean sizes of about 3 µm. Diffuse reflectance spectra reveal that the samples obtained using the former method present a higher brilliancy, so they have been selected to be tested as a green pigment in ceramics with good results [67].

The pigments of general formula $CuAl_{2-x}Ln_xO_4$, where (x = 0, 0.5, 1.0, 1.5 and 2 and Ln = Eu, Sm, Nd, Y, La, Tm) were synthesized by the solid state reaction method at 900 - 1100°C. The resultant color impression of the pigments was related to ionic radii of the rare earth cations. Yttrium and thulium contained pigments changed their color properties from deep brown through dark green ($CuAl_{1.5}Ln_{0.5}O_4$, $CuAlLnO_4$) to the intensive turquoise color hue ($CuLn_2O_4$). The pigments with the rising amount of lanthanide cations (x = 0.5 and 1) had darker and less rich color hue than the primary pigment (x = 0). The values of lightness and chroma again increased with increasing amount of the lanthanide cations. The CuY_2O_4 pigment has more interesting turquoise hue than the $CuTm_2O_4$ pigment. A minor amount of green hue (-a^*) and at the same time the major amount of blue hue (-b^*) contribute to the formation of a more interesting turquoise color of the CuY_2O_4 pigment [68].

A green colored nano-pigment Y_2BaCuO_5 with high NIR reflectance (61% at 1100 nm) was synthesized by a nano-emulsion method. The XRD and Rietveld analyses of the designed pigment powders reveal the orthorhombic crystal structure for Y_2BaCuO_5, where yttrium is coordinated by seven oxygen atoms, barium is coordinated by eleven oxygen atoms and the coordination polyhedron of copper is a distorted square pyramid [CuO_5]. The UV-visibile spectrum of the nano-pigment exhibits an intense transition associated with CuO_5 chromophore between 2.1 - 2.5 eV in the visible domain. Therefore, the developed nano-pigment shows the green color. The potential utility of the synthesized pigments for cool roof application was demonstrated by coating onto a building roofing material like cement slab and PVC coatings [69].

Novel green pigments based on $(R_{1-x}R'_x)_2Cu_2O_5$ (R = Y^{3+}, R' = Sc^{3+}, Gd^{3+}, Tm^{3+} , Yb^{3+} and Lu^{3+}) solid solutions were synthesized by the solid state method and the dopant concentration was optimized. Among the samples, it was found that $Sc_2Cu_2O_5$ based samples showed brilliant green hue. In response to the results $Sc_2(Cu_{1-x}Zn_x)_2O_5$ ($0 \leq x \leq 0.1$) pigments were further synthesized and their color properties were characterized in an attempt to find a new environmentally friendly pigment that has more sufficient green chromaticity. Among the samples, the most vivid green hue was obtained for $Sc_2(Cu_{0.92}Zn_{0.08})_2O_5$ with a greenness value ($-a^*$) of 41.2 in the CIE $L^*a^*b^*$ system, which was significantly larger than those of commercially available pigments. This pigment should be an effective alternative to the conventional toxic green pigments [70].

Nontoxic $Y_2Cu_2O_5$ nano-pigments were synthesized by sol-gel combustion method and the effects of synthesis parameters on their chromatic properties have been studied. The chromatic properties of the samples were studied by UV-visible reflectance spectroscopy and the $L^*a^*b^*$ coordinates were evaluated using the CIE $L^*a^*b^*$ 1976 color scales. The results showed that the chromatic properties of nano-pigments were changed by altering the synthesis conditions. In addition, some $Y_2Cu_2O_5$ micro sized pigments were synthesized by solid state reaction and the measurements showed that the chromatic properties of the nano-pigments were slightly bigger than those of the large particles from the solid state method. Measurements of a^* and b^* showed that the nano-pigments are also very stable in glazes [71].

1.18 Objectives of the Present Work

Inorganic pigments have been widely used for a large variety of industrial applications such as in ceramic tiles, inks, plastics, glasses and paints, etc. Among the primary colored pigments, blue and green colored quality materials are relatively rare. Currently used inorganic blue pigments are cobalt blue ($CoAl_2O_4$), ultramarine blue ($Na_7Al_6Si_6O_{24}S_3$) and Prussian blue, ($Fe_4[Fe(CN)_6]_3$) etc. Ultramarine blue and azurite are sensitive to acid, while Prussian blue possesses poor alkali stability. Raising cost and toxicity make a pressing need to reduce the consumption of cobalt in the ceramic industry. Recently a blue inorganic pigment, $YIn_{1-x}Mn_xO_3$, based on hexagonal $YInO_3$ is reported. The blue color of the oxides arises from the specific trigonal bipyramidal ligand field around Mn^{III} in a $YInO_3$ host. However, a few host structures having a Mn^{3+} ion in their geometry have been found so far.

Conventional industrial green pigments such as chrome oxide green (Cr_2O_3), cobalt green ($CoO{\cdot}ZnO$), and cobalt titanate green spinel (Co_2TiO_4) have serious problems from a practical viewpoint. Cr_2O_3 contains toxic Cr, and $CoO{\cdot}ZnO$ and Co_2TiO_4 are less than perfect in green color. However, their color properties are not adequate as compared to the existing industrially used toxic pigments. Apart from this, high infrared reflective pigments are now in great demand for usae in coatings, cement pavements, automotive and camouflage applications. Development of less toxic inorganic pigments that have a greater infrared reflectivity is highly essential while maintaining the appropriate light absorption in the visible spectrum to impart color. The main objective of the present research work is to develop alternatives to the existing blue and green inorganic pigments that are more sustainable and commercially viable for potential applications.

1.19 References

1. A. D. Broadbent, Basic Principles of Textile Coloration, Society of Dyers and Colourists, England (2001).
2. L. Pereira, M. Alves, Dyes-Environmental Impact and Remediation, in: A. Malik, E. Grohmann (Eds.), Environmental Protection Strategies for Sustainable Development, Springer, London (2012).
3. D. C. Nwokonkwo, IOSR J. Appl. Chem. 4 (2013) 74.
4. R. N. Rothon, Pigment and Nanopigment Dispersion Technologies, Smithers Rapra Publishing, Shrewsbury, United Kingdom (2012).
5. G. Buxbaum, G. Pfaff, Industrial Inorganic Pigments, John Wiley and Sons, United States (2006).
6. P. Merchak, Colored Organic Pigments. In: J.V. Koleske (ed) Paint and Coating Testing Manual: 15th edition of the Gardner-Sward Handbook. ASTM International, West Conshohocken, Pennsylvania (2012).
7. Kirk-Othmer, Encyclopedia of Chemical Technology, Wiley, New York (1998).
8. V. Malshe, A. Bendiganavale, Recent Patents on Chemical Engineering 1 (2008) 67.
9. A. Libbra, L. Tarozzi, A. Muscio, M. A. Corticelli, Opt. Laser Technol. 43 (2011) 394.
10. R. Levinson, H. Akbari, P. Berdahl, Sol. Energy 84 (2010) 1717.
11. M. Zinzi, E. Carnielo, S. Agnoli, Energy Buildings 50 (2012) 111.
12. Y. Ohno, CIE Fundamentals for Color Measurements, International Conference on Digital Printing Technologies, Vancouver, Canada (2000).
13. G. Buxbaum, G. Pfaff, Industrial inorganic pigment, Wiley-VCH Verlag GmbH and Co, Weinheim (2005).
14. H. G. Volz, Industrial Color Testing Fundamentals and Techniques, Wiley-VCH, Weinheim, Germany (2001).
15. Commission Internationale del'Eclairage Proceedings, Cambridge University Press, Cambridge, United Kingdom (1931).
16. T. Smit, J. Guild, Trans. Opt. Soc. 33 (1932) 73.
17. W. D. Wright, Trans. Opt. Soc. 30 (1928) 141.
18. J. Guild, Phil. Trans. R. Soc. Lond. 230 (1932) 149.
19. https://en.wikipedia.org/wiki/CIE_1931_color_space.

20. R. W. Hunt, Measuring Color, Fountain Press, England (1998).
21. A. C. Harris, I. L. Weatherall, J. R. Soc. N. Z. 20 (1990) 253.
22. http://www.brucelindbloom.com (3D Representations of the $L^*a^*b^*$`gamut).
23. M. R. Luo, New Colour Difference Formula for Surface Colors, Ph.D Thesis, University of Bradford, England (1986).
24. R. C. Zeller, H. Hemmendinger, Evaluation of Color-Difference Equations: a New Approach, AIC Color 77 Adam Hilger, Bristol (1978).
25. A. Schuster, Astrophys. J. 21 (1905) 1.
26. P. Kubelka, F. Munk, Z.Tech. Phys. (Leipzig) 12 (1931) 593.
27. P. Kubelka, J. Opt. Soc. Am. 38 (1948) 448.
28. P. Kubelka, J. Opt. Soc. Am. 44 (1954) 330.
29. J. A. Van den Akker, Tappi 32 (1949) 498.
30. A. S. Stenius, Svensk. Papperstidn. 54 (1951) 663.
31. A. S. Stenius, Svensk. Papperstidn. 54 (1951) 701.
32. A. S. Stenius, Svensk. Papperstidn. 56 (1953) 607.
33. G. Mie, Ann. Phys. (Leipzig) 25 (1908) 377.
34. E. S. Thiele, R. H. French, J. Am. Chem. Soc. 81 (1998).
35. M. V. Orna, J. Chem. Educ. 57 (1980) 264.
36. R. C. West, Handbook of Chemistry and Physics, CRC Press, Cleveland (1975-76).
37. K. Nassau, The Physics and Chemistry of Color: The Fifteen Causes of Color, John Wiley and Sons, New York (1983).
38. K. Nassau, Sci. Am. 243 (1980)124 .
39. E. Fritsch, G. R. Rossman, Gems and Gemology 23 (1987)126.
40. K. Nassau, Am. Mineral. 63 (1978) 219.
41. http://goldbook.iupac.org/I03125.html (Intervalence charge transfer)
42. S. A. Holgate, Understanding Solid State Physics, CRC Press, Florida, United States (2009).
43. B. M. Loeffler, R. G Burns, Am. Sci. 64 (1976) 636.
44. R. G. Burns, Mineralogical Applications of Crystal Field Theory, Cambridge University Press, Cambridge, United Kingdom (1970).
45. D. Jonynaitė, J. Senvaitienė, J. Kiuberis, A. Kareiva, Chemija 20 (2009) 10.
46. P. L. Leung, H. Luo, X Ray Spectrom. 29 (2000) 34.

47. P. Colomban, G. Sagon, X. Faurel, J. Raman Spectrosc. 32 (2001) 351.
48. J. Riederer, Archaeometry 16 (1974) 102.
49. M. Bouchard, A. Gambardella. J. Raman Spectrosc. 41 (2010) 1477.
50. A. Zucchiatti, A. Bouquillon, I. Katona, A. D'Alessandro, Archaeometry 48 (2006) 131.
51. R. A. Eppler, Colorants for Ceramics-Kirk-Othmer Encyclopedia of Chemical Technology, John Wiley and Sons, New Jersey, United States (2000).
52. D. M. A. Melo, J. D. Cunha, J. D. G. Fernandes, M. I. Bernardi, M. A. F Melo, A. E. Martinelli, Mater. Res. Bull. 38 (2003) 1559.
53. T. Mimani, S. Ghosh, Curr. Sci. 78 (2000) 892.
54. A. Fores, M. Llusar, J. A. Badenes, J. Calbo, M. A. Tena, G. Monros, Green Chem. 2 (2000) 93.
55. E. Ozel, H. Yurdakul, S. Turan, M. Ardit, G. Cruciani, M. Dondi, J. Eur. Ceram. Soc. 30 (2010) 3319.
56. K. A. Stewart, T. J. Detrie, G. B Burkhart, D. R. Swiler, Inorganic Pigments, US7014701 B2 (2006).
57. M. Llusar, A. Fores, J. A Badenes, J. A. Calbo, M. A. Tena, G. Monros, J. Eur. Ceram. Soc. 21 (2001) 1121.
58. H. Ahamdane, M. A. El Idrissi Raghni, F. Bensamka, A. Outzourhit, M. J. Condens. Matter 8 (2007) 1.
59. M. Llusar, A. Zielinska, M. A. Tena, J. A. Badenes, G. Monrósa, J. Eur. Ceram. Soc. 30 (2010) 1887.
60. M. Dondi, C. Zanelli, M. Arditw, G. Cruciani, J. Am. Ceram. Soc. 94 (2011) 1025.
61. A. E. Smith, H. Mizoguchi, K. Delaney, N. A. Spaldin, A. W. Sleight, M. A. Subramanian, J. Am. Chem. Soc. 131 (2009) 17084.
62. H. Mizoguchi, A. W. Sleight, M. A. Subramanian, Inorg. Chem. 50 (2011) 10.
63. M. Ocaña, J. P. Espinós, J.B. Carda, Dyes Pigm. 91 (2011) 501.
64. S. Tamilarasan, D. Sarma, M. L. P. Reddy, S. Natarajan, J. Gopalakrishnan, RSC Adv. 3 (2013) 3199.
65. T.-G. Kim, S.-J. Kim, C. C. Lin, R.-S. Liu, T.-S. Chan, S.-J. Im, J. Mater. Chem. C 1 (2013) 5843.

66. S. Jose, A. Jayaprakash, S. Laha, S. Natarajan, K. G. Nishanth, M. L. P. Reddy, Dyes Pigm. 124 (2016) 120.

67. F. Fernandeza, C. Colona, A. Durana, R. Barajasa, A. Dorsb, M. Becerrilb, J. Llopisc, S. E. Pajecd, R. Saez-Puche, I. Julian, J. Alloys Compd. 275 (1998) 750.

68. Ž. Dohnalová, P. Šulcová, M. Trojan, Ceram. Mater. 60 (2008) 139.

69. S. Jose, A. Prakash, S. Laha, S. Natarajan, M. L. P. Reddy, Dyes Pigm. 107 (2014) 118.

70. T. Masui, N. Takeuchi, H. Nakado, N. Imanaka, Dyes Pigm. 113 (2015) 336.

71. M. Farbod, Z. Rafati, Ceram. Int. 42 (2016) 15.

2

INTENSE BLUE COLORS IN WOLFRAMITE-TYPE Co^{2+}:$MgWO_4$ OXIDES THROUGH DISTORTION IN Co^{2+} OCTAHEDRA

New inorganic cobalt based blue pigments $Mg_{1-x}Co_xWO_4$ (x = 0.1, 0.2 and 0.3) have been prepared by the solid-state reaction and flux added methods. The synthesized samples show intense blue color with a very low doping concentration of cobalt. Raising cost and toxicity make a critical need to reduce the consumption of cobalt in the ceramic industry, at the same time trying to improve the efficiency and sustainability of pigments. The present investigation helps us to minimize the cobalt consumption and cost of production with respect to conventional blue ceramic colorants. Intense blue hue was obtained at a relatively low doping concentration of Co^{2+} (20 mol%) with b^* value of -46.97, which is considerably intense than cobalt aluminate spinel (b^* = -32.70). UV-visible absorption properties are strongly related to the coordination environment of the Co^{2+} ions. Increasing the amount of cobalt induces a change in the local symmetry of MgO_6 octahedra witnessed by the change of the metal-ligand bond distances. The changes are attributed to the larger ionic radius and electronegativity of Co^{2+} ions compared to the Mg^{2+} ions in the host lattice. These observations corroborate the important structural distortions arising from the differences in ionic radii and electronegativity between the dopant and host cations.

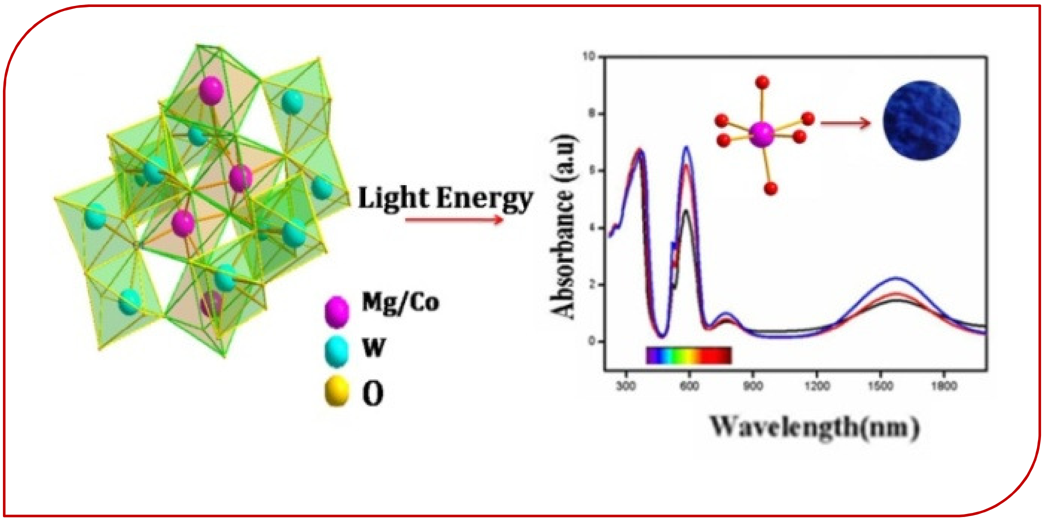

2.1 Introduction

Among the transition metal ions, Co^{2+} is an inevitable source of blue color in ceramic pigment [1]. Co^{2+} ($3d^7$) can adapt to different coordinations giving rise to different colorations and a large number of cobalt based blue, green, violet and light pink pigments are available in the ceramic industry. The commonly used blue pigments are Co aluminate, (Co,Zn) aluminate, $(Co,Cr)Al_2O_4$ and also $(Co,Zn)_2SiO_4$ willemite and in these pigments the intense blue color is associated to Co^{2+} in tetrahedral sites [2, 3]. In contrast, when Co^{2+} ions are accommodated in octahedral sites the color obtained is not so intense and is often violet or pink, as it occurs in Co_2SiO_4 olivine or in some phosphate-based pigments [4-6]. Cobalt based green colored inorganic pigments are also available. Green coloration in ZnO:Co is due to the incorporation of Co^{2+} ions in the tetrahedral site of wurtzite and in the karroite green pigments doped with Co and Zn in which Co^{2+} ions occupy in the octahedral site [7, 8]. Jian Zou et al. synthesized complex green colored pigment with a $TiO_2@CoTiO_3$ core-shell structure, the complex pigments had much lower consumption of cobalt compared to pure $CoTiO_3$ and Co_2TiO_4 pigments [9].

Optical properties are strongly related to the structural features and more especially to the local environment of transition metals. The origin of color in a compound depends on the crystal field splitting; the d-orbital-ligand interaction splits the degeneracy of the transition metal ions [10]. Since this spacing depends on factors such as the geometry of the complex, the nature of the ligands and the oxidation state of the central metal atom. Similar to d-d transitions, charge-transfer (CT) transitions also involve the metal d-orbitals. CT bands are observed if the energies of empty and filled ligand and metal centered orbitals are similar. The direction of the electron transfer is determined by the relative energy levels of these orbitals. Color can be tuned by changing the local environment of transition metal (TM) and covalent character of M–O bonding. Doping of small modifiers into the lattice structure can modify these band gap interactions and give rise to color, or shift the color.

Recently, Lucile cornu et al reported a blue inorganic oxide material based on triclinic $(Mg,Zn)MoO_4$ substituted with Co^{2+} at the octahedral site [11]. Even though cobalt is considered to be toxic, cobalt appears to be hardly replaceable in order to achieve a deep blue coloration [12]. Recently Forés et al developed an intense blue ceramic pigment based on the willemite lattice, with low Co content, ranging from 25 mol% Co ($Co_{0.5}Zn_{1.5}SiO_4$) to 2.5 mol% Co ($Co_{0.05}Zn_{1.95}SiO_4$). Here $Co_{0.5}Zn_{1.5}SiO_4$ exhibits the best blue hue once enameled ($b^* = -39$), but the color intensity diminishes producing lighter colors [13]. Research on ceramic pigments has been dedicated with the aim of obtaining new low-toxic pigments. Moreover, the product performance must meet the growing social demands in the environmental, technological and economical point of view. In the present investigations, we prepared alternative blue ceramic pigment for replacing the traditional blue colored pigments. Here we develop new blue ceramic pigment containing a relatively lower amount of Co^{2+} ($x = 0.20$) doped on $MgWO_4$, thereby we can reduce the toxicity and cost of production compared to other Co-containing ceramic pigments such as (olivine –Co_2SiO_4, spinel–$CoAl_2O_4$).

Divalent-metal tungstates (AWO_4) are currently being studied with great interest due to their use as materials for scintillator detectors, laser-host crystals, as well as in acoustic and optical fiber applications [14, 15]. Magnesium tungstate ($MgWO_4$), the mineral hunzalaite, is part of this family. It is one of the most extensively studied metal tungstates because of its interest as a scintillator material for cryogenic applications [16]. The color is an optical property having interests in several industrial areas, such as ceramics, textiles, cosmetics, plastics, and paints. Here we have studied the coloring and NIR reflectance properties of the $Mg_{1-x}Co_xWO_4$ (x = 0, 0.1, 0.2 and 0.3) system by using Co^{2+} as the chromophore. In the present work, the optical properties are coming from the octahedral coordination of Co^{2+} in the $MgWO_4$ host lattice.

2.2 Experimental Section

2.2.1 *Materials and Synthesis*

$Mg_{1-x}Co_xWO_4$ (x = 0, 0.1, 0.2 and 0.3) has been prepared by the solid state method and flux added method. The precursors used for this purpose are MgO (Aldrich, 99.9%), WO_3 (Aldrich, 99.9%) and CoO (Aldrich, 99.9%). In a typical pigment sample $Mg_{0.9}Co_{0.1}WO_4$, MgO (0.1316 g, 0.0032 mol), WO_3 (0.8411 g, 0.0040 mol) and CoO (0.0272 g, 0.00040 mol) were mixed for four times using a mortar with acetone (approximately 10 ml), and then the mixture was dried in an oven at 100°C for 30 min to evaporate acetone. The process of mixing and drying was repeated thrice to get a homogeneous mixture. Finally, the dried mixtures were placed in platinum crucibles and calcined in an electric furnace at 1100°C for 12 h, using a heating rate of 5°C/min. The calcined samples were ground thoroughly into fine powders in an agate mortar for further studies. In the flux added method we prepared $Mg_{0.8}Co_{0.2}WO_4$ by adding 0.05 wt. % of NH_4Cl. In order to get the homogeneous mixture we carried out the above mentioned procedures and the sample is calcined at 900°C for 6 h.

2.2.2 *Characterization*

Formation of single phase product and their structure was studied by using powder X-ray diffraction. The PXRD pattern was taken with the aid of the PANalytical X'pert Pro diffractometer (Ni-filtered Cu Kα radiation, λ = 1.5406 Å). The data were recorded over the 2θ range of 10° - 90°. In order to establish the crystal structures correctly. Rietveld analysis of the samples was carried out and a detailed exploration of the lattice parameters, bond distances, and other structural parameters was done with the X'Pert HighScore Plus software. The morphology of the prepared samples was examined by scanning electron microscopy (JEOL JSM-5600 LV SEM). The thermal stability of the colorant was also checked using a (Schimadzu, DTG-60) make in an argon atmosphere at a heating rate of 20°C/min. For the characterization of the pigment quality of the samples (the color parameters), the diffuse reflectance spectra were recorded (220-2000 nm) employing a (Shimadzu UV-3600) UV-vis spectrometer using PTFE as the reference. The CIE 1976 $L^*a^*b^*$ colorimetric method was used, as recommended by the Commission Internationale de l'Eclairage (CIE). In this method, L^* is the lightness axis [black (0) to white (100)], a^* is the green (−ve) to red (+ve) axis, and b^* is the blue (−ve) to yellow (+ve) axis. The parameter, C^* = $[(a^*)^2 + (b^*)^2]^{1/2}$ represents saturation of the color and $h°= tan^{-1}(\frac{b^*}{a^*})$ represents the hue angle. The IR solar reflectance was calculated in accordance with the ASTM standard number G173-03. The IR solar reflectance is expressed as the integral of the percent reflectance times the solar irradiance divided by the integral of the solar irradiance when integrated over the 700 - 2500 nm range as shown in the formula 2.1.

$$\frac{\int_{750}^{2500} r(\lambda)i(\lambda)d(\lambda)}{\int_{750}^{2500} \mathrm{i}(\lambda)\mathrm{d}(\lambda)} \qquad (2.1)$$

Where *r(λ)* is the spectral reflectance obtained from the experiment and *i(λ)* is the standard solar spectrum ($Wm^{-2}nm^{-1}$) obtained from the standard. The NIR solar reflectance spectra were determined from ASTM Standard G173-03.

2.3 Results and Discussion

2.3.1 *Structural Analysis*

The XRD patterns were recorded to identify the phase purity and crystal structure of the material. The XRD patterns of the samples prepared from the solid state method and flux addition method are taken. The crystal structure of $MgWO_4$ consists of alternating layers of MgO_6 and WO_6 octahedral units. The structure of the $MgWO_4$ can be described as a network of interconnected zigzag chains of alternate MgO_6 and WO_6 distorted octahedra running along the crystallographic axis C [17]. $MgWO_4$ exists in wolframite type monoclinic structure belonging to space group P2/c and has C_{2h} point-group symmetry with two formula units per primitive cell [18]. Magnesium, tungsten and oxygen atoms occupy the 2*f*, 2*e,* and 4*g* sites, respectively [19]. The existence of two non-equivalent positions for oxygen atoms (labeled as O1 and O2) is a characteristic of the structure of $MgWO_4$ tungstate. There are two tungsten atoms and one magnesium atom in the nearest arrangement of the O1 atoms, whilst one tungsten atom and two magnesium atoms are among the nearest neighbors of the O2 atoms. The schematic of the unit cell of $MgWO_4$ was drawn with the help of diamond software in order to get some idea of the crystal structure (Figure 2.1).

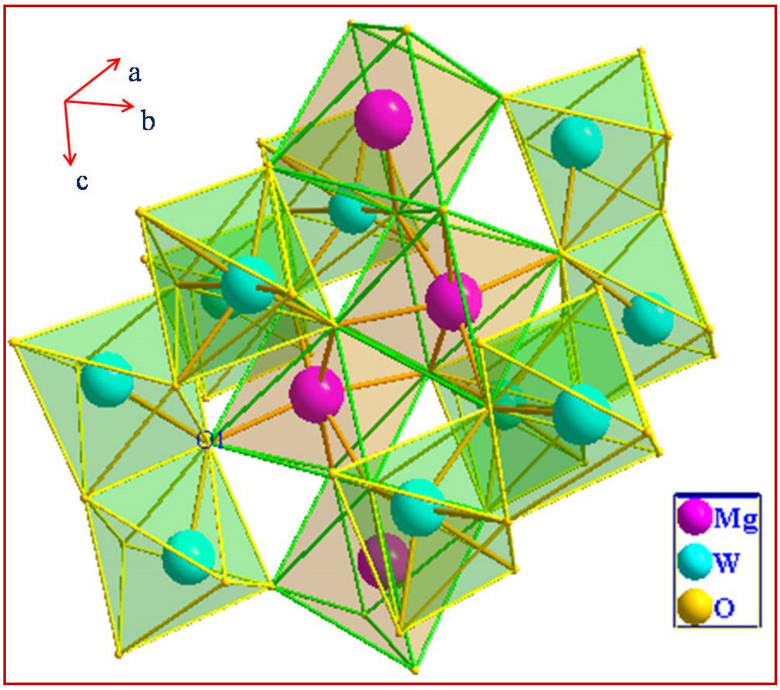

Figure 2.1 Schematic representation of the crystal structure of $MgWO_4$

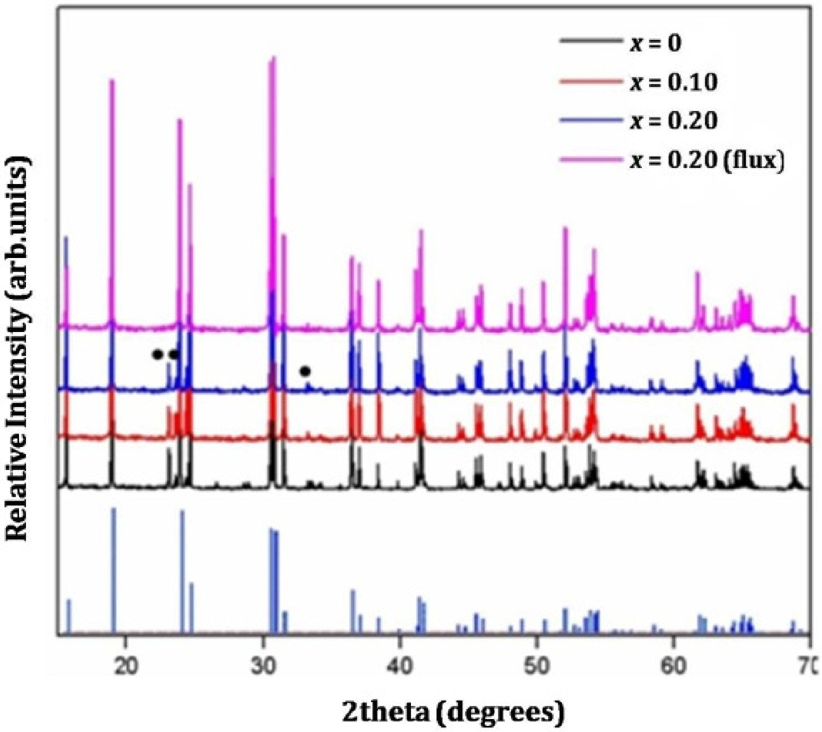

Figure 2.2 Powder XRD patterns of $Mg_{1-x}Co_xWO_4$ (x = 0.1, 0.2, 0.3 and 0.2 (flux)

Figure 2.2 shows the XRD patterns of $Mg_{1-x}Co_xWO_4$ (x = 0.1, 0.2, 0.3 and 0.2 (flux) samples. All the diffraction peaks can be indexed to the monoclinic structure with P2/c space group in agreement with the JCPDS file No. (01-073-0562). In the solid state reaction method, the doped samples contain traces of impurity phase of WO_3 marked as bold circles in figure 2.2. Sample from the flux added method shows no evidence of any kind of secondary or impurity phase. When the concentration of cobalt increased above 30 mol% some secondary phase of $CoWO_4$ is formed. The diffraction peak of $Mg_{1-x}Co_xWO_4$ (x = 0.1, 0.2 and 0.3) slightly shifted towards the lower angle side with increasing the concentration of the Co^{2+} ion. The Co^{2+} (ionic radius) doping in the Mg^{2+} position will lead to change in lattice volume of the monoclinic crystal structure from 131.1153 to 131.1671 Å^3. This is because of the ionic radius of Co^{2+} (74.5 pm for 6 C.N) slightly higher than that of Mg^{2+} (72 pm for 6 C.N), showing that Co^{2+} ion effectively incorporated into the $MgWO_4$ host lattice [20].

Table 2.1 Lattice parameters of $Mg_{1-x}Co_xWO_4$ (x = 0.1, 0.2, 0.3 and 0.2 (flux)).

x	***a* (Å)**	***b* (Å)**	***c* (Å)**	***β* (degrees)**	**Crystallite size (nm)**
00.10	4.6880(4)	5.6760(4)	4.9276(4)	90.6169	109.76
00.20	4.6830(4)	5.6788(4)	4.9310(4)	90.5229	109.74
00.30	4.6812(5)	5.6789(4)	4.9342(4)	90.4436	109.99
0.2 (flux)	4.6842 (4)	5.6765(4)	4.9319(4)	90.5667	99.74

Variations of Lattice parameters of the samples with respect to doping concentration (x) are calculated with the aid of X'Pert HighScore Plus software is given in table 2.1. There is a gradual increase in the b, c cell parameters and unit cell volume with increasing of x, which is consistent with the shift of the diffraction peaks. Whereas the a unit cell parameter slightly decreases as the cobalt content increases. The net result is c/a ratio increases linearly with increasing of Co concentration. The unit cell parameters of $MgWO_4$ taken from reference PDF 27-789 (a = 4.6879 Å, b = 5.6751 Å, c = 4.9288, β = 90.7°, V = 131.1 Å^3). The crystallite size was calculated from the XRD pattern using the Scherer equation crystallite size $D = 0.94\lambda/\beta\cos\theta$. Here, D is the crystallite size for the (hkl) plane, λ is the wavelength of the incident X-ray radiation [Cu Kα (0.154056 nm), β is the full width at half maximum (FWHM) in radians and θ is the diffraction angle for the (*hkl*) plane. A plot of unit cell edges for the $Mg_{1-x}Co_xWO_4$ solid solution is shown in figure 2.3. From this figure, it can be seen that the lattice constant increases a very little amount with the increase in Co^{2+} concentration.

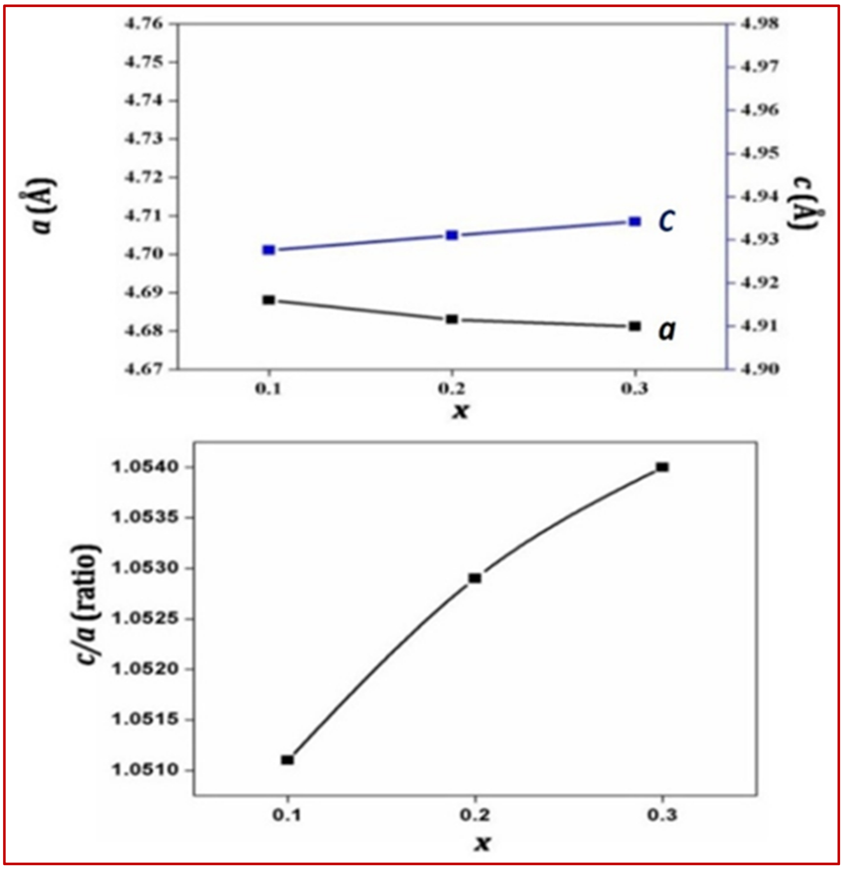

Figure 2.3 Unit cell parameter *a* and *c* (left) and *c/a* ratio (right) of $Mg_{1-x}Co_xWO_4$ (x = 0.1, 0.2 and 0.3)

The structural parameters of the $Mg_{0.8}Co_{0.2}WO_4$ (flux added) compound (cell parameters and atomic positions) are refined. Rietveld refinement of the obtained XRD data was carried out using X' Pert HighScore Plus software. In order to determine the quality of the final refinement, reliability factors are defined to compare the difference between the observed pattern and calculated profile. Observed, calculated, and difference XRD plots are represented in figure 2.4. The crystallographic data of previously reported $MgWO_4$ as the starting model was employed to refine the patterns of the doped sample [21].

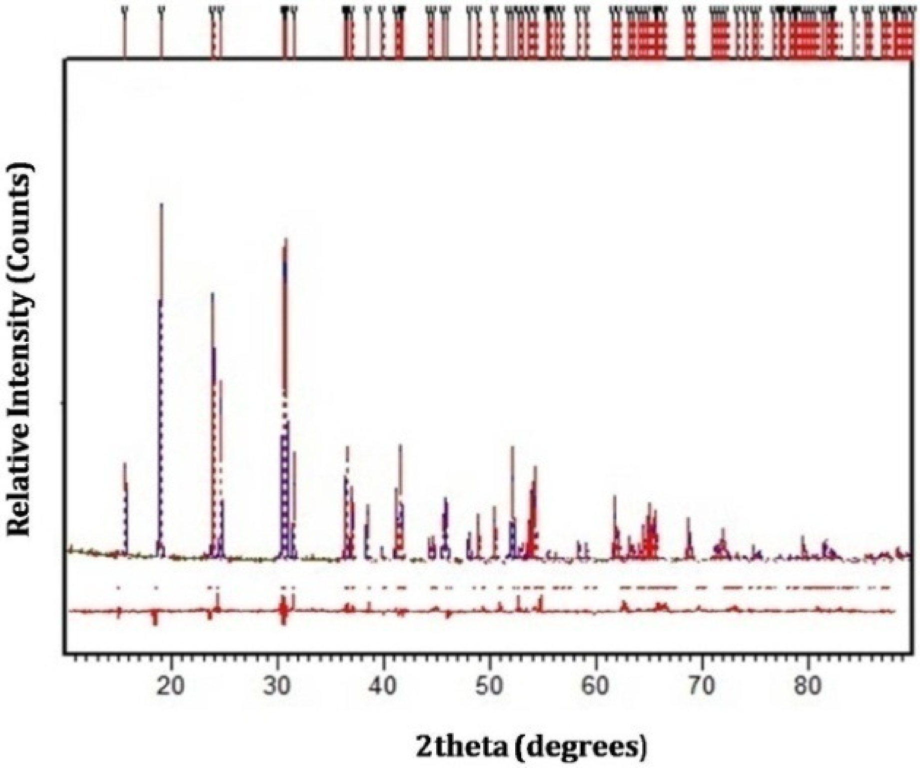

Figure 2.4 The observed, calculated and difference (at the bottom) X-ray powder diffraction pattern for $Mg_{0.8}Co_{0.2}WO_4$ (flux added) at room temperature.

Rietveld data and experimental conditions for data collection are reported in table 2.2, and the final reliability factors are given. Based on the structural property of $MgWO_4$ crystal, there is only one kind of lattice site occupied by Mg^{2+} ion. The final values for the structural parameters of the wolframite type phase of $Mg_{0.8}Co_{0.2}WO_4$ (flux added) are presented in table 2.2. The weighted profile reliability (R_{wp}) factor is the more valuable, for a complex phase (monoclinic to triclinic), a value < 0.15 is good.

Table 2.2 Rietveld refinement data of $Mg_{0.8}Co_{0.2}WO_4$ (flux added).

Atom	**Site**	***x***	***y***	***z***
Mg	2*f*	0.5000	0.6592	0.2500
W	2*e*	0.0000	0.1821	0.2500
O1	4*g*	0.2210	0.1010	0.9301
O2	4*g*	0.2660	0.3847	0.4127
Flat Back ground	56.2359			
Scale Factor	0.000228			
U	0.0151			
V	-0.0064			
W	0.0056			
Peak Shape 1	0.8751			
Peak Shape 2	-0.0087			
R_{wp} (%)	14.68			
R_{exp} (%)	10.25			
R_p (%)	11.62			
GoF	2.04			

From the Rietveld refinement data, we found that doping of Co^{2+} ions in the Mg^{2+} site changes the average Mg/Co–O and W–O bond length. The bond length variations arising from doping Co^{2+} ions into the divalent site of the $MgWO_4$ host lattice prepared from solid state method are shown in table 2.3. The average Mg–O bond length decreases from 2.068 Å to 2.058 Å and the average W–O bond length increases from 1.958 Å to 1.966 Å with the increase in Co^{2+} concentration. The results indicate that the Co^{2+} ions exhibit an effect on the crystallographic environment and that these modifications provide desirable optical properties.

Table 2.3 Interatomic distances in $Mg_{1-x}Co_xWO_4$ (x = 0.1, 0.2 and 0.3).

x	0.1	0.2	0.3
Mg/Co-O2	2.042	2.025	2.020
-O2	2.070	2.062	2.065
-O1	2.092	2.091	2.090
Average	2.068	2.059	2.058
W-O2	1.854	1.877	1.882
-O1	1.943	1.940	1.941
-O1	2.077	2.072	2.077
Average	1.958	1.964	1.966

Table 2.4 Bond valence sum for $Mg_{1-x}Co_xWO_4$ (x = 0.1, 0.2 and 0.3).

x	C.N	R_{ij}	BVS
0.1	6	2.068	2.05
0.2	6	2.059	2.09
0.3	6	2.058	2.10

Bond valence sums were calculated to confirm the proper coordination numbers and oxidation states (Table 2.4). According to Pauling, the BVS surrounding the j^{th} atom or ion is equal to the oxidation state Z_j, as shown in equation 2.1 [22]. The valences of the individual bonds, S_{ij} in the equation. 2.2 can be calculated from the observed bond lengths using equation 2.3 [23]. Where the atomic positions and interatomic distances are available, the BVS were obtained by inserting the bond lengths directly into this formula. Where R_0 and R_{ij} are expected and experimentally determined bond lengths between the atoms i and j, and B is a constant (0.37 Å for oxide compounds. Values of R_0 as 1.67 Å for Co–O was used in all calculations [23]. BVS for Co^{2+} in all compositions is in the range of 2.04 - 2.10, in good agreement with the presence of Co(II) in the compounds.

$$Z_{j=} \sum_i S_{ij} \rightarrow \tag{2.2}$$

$$S_{ij=\sum_j e^{\frac{R_O - R_{ij}}{B}}} \rightarrow \tag{2.3}$$

2.3.2 *Morphological analysis*

Scanning electron microscopy was carried out on the calcined pigment powder samples in order to find out the surface morphology and the particle size. SEM micrographs of $Mg_{0.8}Co_{0.2}WO_4$ samples prepared by the flux added method and the SSR method are shown in the figure. 2.5. The figures indicate the existence of agglomerates in these samples. In the SSR method, pigment particles have a bigger particle size and present irregular morphology and some smaller particles anchored on the surface of these irregular particles. The sample obtained by the flux added method is formed by aggregates of small particles. The synthesized samples consist of irregular particles and the average particle size of the non-fluxed sample (x = 0.20) was found to be 20 μm and the average size of flux added (x = 0.20) sample was found to be 14 μm. The particle size of the sample that was prepared by the flux added method is smaller than the sample prepared by the SSR method. The reflectance of the sample prepared from the flux added method is higher than that of the solid state method, because aggregates of smaller particle provide more surface for light reflectance.

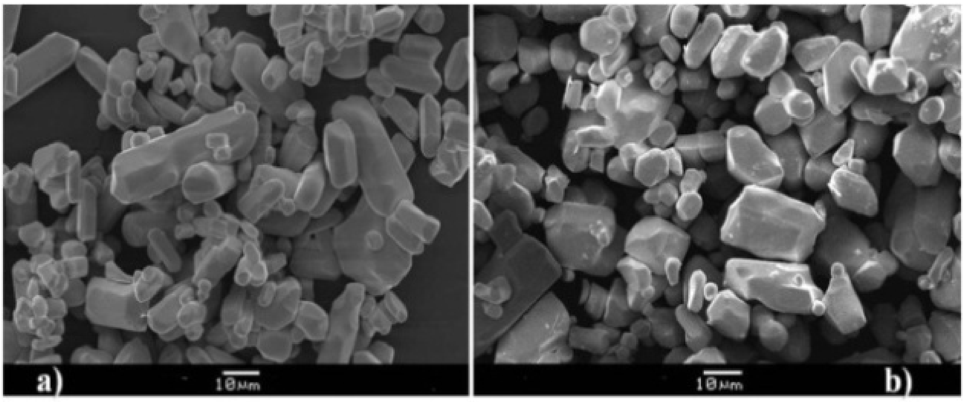

Figure 2.5 SEM photographs of $Mg_{0.8}Co_{0.2}WO_4$ prepared from a) solid state method b) flux added method.

2.3.3 *UV-Visible Studies*

The blue colors of the $Mg_{1-x}Co_xWO_4$ (x = 0.1, 0.2, 0.3 and 0.2 (flux)) samples are evident even in very low concentrations of Co^{2+} ions. To understand the origin of this blue color, we measured diffuse reflectance spectra using (Shimadzu UV-3600) UV-visible spectrometer. Absorption spectra of cobalt complexes can give very important structural information such as coordination environment of the Co^{2+} ion. The absorbance spectrum of Co^{2+} doped in $MgWO_4$ shown in figure 2.6. In all, four absorption bands are observed, one in the infrared region, two in the visible regions and one in the ultraviolet region. Cobalt spectra are mainly appealing in that they are distinguished by narrow spin-forbidden bands as well as by broad spin-allowed bands, which are more typical of d–d transitions. The absorption bands of the flux added one, is broader and less intense than that of the non-fluxed samples. The lower intensity could be presumably associated with the lower particle sizes in this fluxed sample.

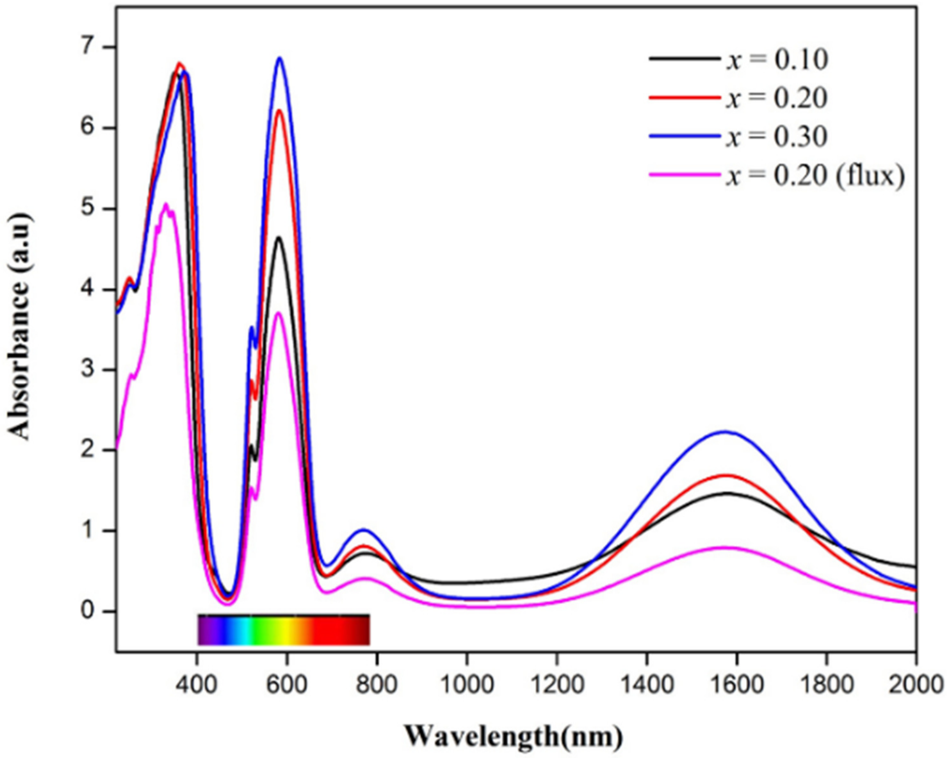

Figure 2.6 Absorbance spectra of $Mg_{1-x}Co_xWO_4$ (x = 0.1, 0.2, 0.3 and 0.2 (flux).

The Co^{2+} ion has the d^7 configuration, in an octahedral field may give rise to either high spin or low spin complexes. The free ion Co^{2+} gives rise to ^4F, ^4P, ^2P, ^2D, ^2G, ^2H, and ^2F and other doublet terms. In an octahedral high spin field, the lowest free ion state, ^4F forms the ground state according to Hund's rule. In the weak octahedral field the ^4F splits into two orbital triplets, $^4T_{Ig}(F)$ and $^4T_{2g}(F)$, and an orbital singlet, $^4A_{2g}(F)$, while the next lowest free ion state, ^4P, remains un-split ($^4T_{Ig}(P)$, the ground state term in the high spin field is $^4T_{Ig}(F)$ (Figure 2.7). In the high spin octahedral field three spin allowed electronic transitions are expected, namely, $^4T_{Ig}(F)$ to $^4T_{2g}(F)$ (ν_1), $^4T_{Ig}(F)$ to $^4A_{2g}(F)$ (ν_2) and $^4T_{Ig}(F)$ to $^4T_{Ig}(P)$ (ν_3) [24]. The transition from the ground state $^4T_{Ig}(F)$ to $^4T_{2g}(F)$ leads to a broad absorption band in the near infrared region located in the 6330 cm^{-1}(1580 nm). A broad and less intense band at 12990 cm^{-1} (769 nm) is due to the transition from $^4T_{Ig}(F)$ to $^4A_{2g}(F)$. Another broad band in the visible region is due to the transition from $^4T_{Ig}(F)$ to $^4T_{Ig}(P)$, located at the 17241 cm^{-1} (580 nm) [24]. The absorption band corresponding to the $^4T_{Ig}(F)$ to $^4A_{2g}(F)$ transition involves a two electron jump and hence it is expected to be very weak [25]. Generally, the spin-allowed band should be strong and intense, the two intense bands observed at 6330 cm^{-1} and 17241 cm^{-1} have been assigned to the transitions from $^4T_{Ig}(F)$ to $^4T_{2g}(F)$ and $^4T_{Ig}(F)$ to $^4T_{Ig}(P)$ respectively, which are characteristic of Co^{2+} ion in octahedral symmetry. In addition, a new band is observed with maxima at 19230 cm^{-1} (520 nm) assigned to the transition $^4T_{Ig}(F)$ to $^2A_{Ig}(G)$ [26]. The interaction between the $^4T_{Ig}(P)$ state and doublet states arising from the free-ion ^2P and ^2G-states, in most cases, causes one or two shoulders. This band is typical of Co^{2+} ion in octahedral coordination and appears as a shoulder to the on the high energy side of $^4T_{Ig}(P)$ band. With the help of the TANABE-SUGANO energy level diagram, the bands observed in the ultraviolet region, located at 27397 cm^{-1} (365 nm) is due to $^4T_{Ig}(F)$ to $^2A_{2g}(F)$ transition.

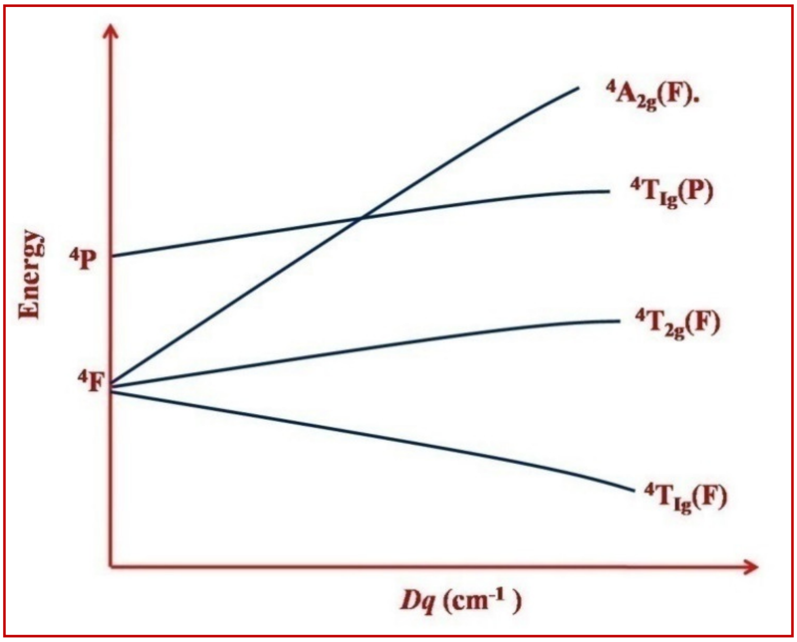

Figure 2.7 Energy level diagram of quartet states of Co^{2+} in octahedral field.

Methods of calculation of the parameters *Dq* and *B* from the ligand-field spectra of octahedral cobalt(II) compounds are discussed. The assignment of the $^4T_{Ig}$(F) to $^4T_{Ig}$(P) levels permits the calculation of *Dq* and *B* by the method of Tanabe and Sugano [27]. *Dq* is the crystal field strength parameter and *B* is the interelectronic repulsion parameter. However, in the case of Co^{2+}, the Tanabe-Sugano diagram cannot be used directly for the calculation of *Dq* and *B*, because of a number of complications, such as the splitting of the $^4T_{Ig}$(F) by spin-orbit coupling and the weakness of the transition $^4T_{Ig}$(F) to $^4A_{2g}$(F). Hence, in the literature, for certain compounds, different values for *Dq* and *B* are sometimes reported, although calculated from the same spectral data. The ligand-field parameters *Dq* and *B* can be calculated using first-order perturbation theory and the transition energies are given by the following equations [28].

$$\nu_1 = \frac{1}{2}(10Dq\text{-}15B') + \frac{1}{2}[(10Dq + 15B')^2\text{-}120DqB]^{1/2} \rightarrow \qquad (2.4)$$

$$\nu_2 = \frac{1}{2}(30Dq\text{-}15B') + \frac{1}{2}[(10Dq + 15B')^2\text{-}120DqB]^{1/2} \rightarrow \qquad (2.5)$$

$$\nu_3 = = [(10Dq + 15B')^2\text{-} 120DqB]^{1/2} \rightarrow \qquad (2.6)$$

But the values obtained by using above equations are not accurate; in order to obtain reasonable values for *Dq* and *B*, Reedwick et al [29] modified the equations ([2.4] and [2.6]) as;

$$\nu_1 = \frac{1}{2}(10Dq\text{-}15B') + \frac{1}{2}[(10Dq + 15B')^2\text{-}120DqB]^{1/2} + 0.45B^2/Dq \rightarrow \qquad (2.7)$$

$$\nu_3 = [(10Dq + 15B')^2 \text{-} 120DqB]^{1/2} + 0.45B^2/Dq \rightarrow \qquad (2.8)$$

In octahedral symmetry the energy ratio ν_2/ν_1 of transitions $^4T_{1g}(F) \rightarrow {}^4T_{2g}(F)$: ν_1 and $^4T_{1g}(F) \rightarrow {}^4A_{2g}(F)$: ν_2 is almost invariable at 1.9 to 2.2 [30]. In the present work, this ratio (2.05) is in good agreement with this prediction. Therefore, the weak band at 12990 cm^{-1} is attributed to the transition $^4T_{1g}(F) \rightarrow {}^4A_{2g}(F)$ (Table 2.5).

Table 2.5 Observed and calculated energies and assignments of the bands for Co^{2+} in $MgWO_4$ (cm^{-1})

x	**$^4T_{1g}(F) \rightarrow {}^4T_{2g}(F)$**		**$^4T_{1g}(F) \rightarrow {}^4A_{2g}(F)$**		**$^4T_{1g}(F) \rightarrow {}^4T_{1g}(P)$**	
	Observed	Calculated	Observed	Calculated	Observed	Calculated
0.10	6309	6305	12903	13105	17242	17261
0.20	6329	6323	12987	13153	17094	17117
0.30	6349	6348	12987	13208	17094	17109

When a metal ion is surrounded by ligands in a complex, the ligand orbitals being directed toward the metal ion make changes in the total electron environment of the metal ion. As a consequence of these electrons, become more delocalized in the complex than they are in the free ion. The expansion of the electron cloud is known as the nephelauxetic effect [31]. An important feature of the nephelauxetic effect is that it is directly related to covalence. Hence, the measure of the B reduction of the compounds is simultaneously a measure of covalence. The decrease of β reflects the increase of covalence in the compounds. From this point of view, the nephelauxetic effect is more useful with respect to chemical bonding than the spectrochemical effect, although they are a rough quantitative process. The nephelauxetic ratio β is given by equation 2.9. [32]

$$\beta = B/B' \qquad (2.9)$$

Where B is the Rach parameter for the free metal ion and B' is the same parameter for the metal ion in the complex.

Table 2.6 Energy parameters for the $Mg_{1-x}Co_xWO_4$ (x = 0.1, 0.2 and 0,3).

x	Dq (cm^{-1})	B' (cm^{-1})	Dq/B	β
0.10	680	789	0.86	0.81
0.20	683	778	0.87	0.80
0.30	686	777	0.88	0.80

(Interelectronic repulsion parameter B for a free Co^{2+} ion is 971)

Examination of the data presented in table 2.6 shows that crystal field splitting increases with increasing the concentration of Co^{2+} despite the larger lattice constant in $Mg_{1-x}Co_xWO_4$ (x = 0, 0.1, 0.2 and 0.3). In the point charge model, splitting shows a relationship with the metal to ligand distance. The bond length (lattice constant), the molecular orbital overlap between metal ions and ligand, and the electronegativity (χ) value mainly affect the magnitude of the crystal-field splitting. From the electrostatic model, it may be interpreted as the bond length of polyhedral volume increases the crystal field splitting decreases. Equation 2.10 was the dependence of crystal-field splitting Dq on the bond length [33]:

$$Dq = 3Ze^2r^4/5R^5 \tag{2.10}$$

Here Z is the charge or valence of the anion, e is the charge of an electron, r is the radius of the d wave function, and R is the bond length. As the bond length or polyhedral volume increases crystal field splitting increases. Equation 2.10 was derived by using a point charge model and therefore can be used only as an approximation for describing crystal field splitting trends with bond distance. Therefore, when the Co–O bond length becomes shorter, the magnitude of the crystal field strength is increased and, because crystal field splitting Dq is proportional to $1/R^5$.

In order to understand the reason behind the variations crystal field strength, our attention is focused on the substantial difference between the electronegativity of Mg^{2+} and Co^{2+} ion. The electronegativity of Co^{2+} (1.88) is higher than that of Mg^{2+} (1.31) [34]. It is well known that electronegativity of cation very much affects the polarizability of an anion. Anion in Mg^{2+}–O^{2-} is more polarizable than that of in the Co^{2+}–O^{2-}, because of less the electronegative Mg^{2+} ion. In Co^{2+}–O^{2-}, the shift of the center of the negative charge density of O^{2-} towards the Co^{2+} is stronger, which decrease the polarizability of the anion. The decreased in the difference in electronegativity value of Co–O indicates the decreases in the ionic strength of the Co–O bond than that of Mg–O bond. This will decrease the average Co–O bond length and render strong crystal field around the Co^{2+} ion [35]. Strong covalency can be expected in the Co^{2+}–O^{2-}, bonding than that of Mg^{2+}–O^{2-} bonding. Even though Mg/Co and W occupy in the different site, through inductive effect, it has strongly affected the nearest WO_6 octahedra, as a result of this, the average W–O bond length increases and distortion of the octahedra occurs. Here we can observe that electronegativity plays an important role in crystal field strength, it is strongly related to the covalency of the Co–O bond. The polarizability of anion decreases with an increase in the electronegativity of cation [36], which in turn increases the covalency of the bond and enhances crystal field splitting. The measure of the nephelauxetic ratio (β) also a direct measure of the covalency, covalency increases with the decrease of β. The observed trend in the crystal field strength is due to the electronegativity differences between the Mg^{2+} and Co^{2+} ions than that of the associated differences in the atoms ionic radius. This stabilization has been linked to the polarizability of the surrounding anion ligands and to the covalency of the crystal.

Table 2.7 shows the color parameters of the $Mg_{1-x}Co_xWO_4$ samples and commercial $CoAl_2O_4$ pigment. As shown in figure 2.8 the L^* values gradually decrease with increasing of x value (0 to 0.3), while a^* and b^* values increase as x moves from 0 to 0.20. From this table, we can see that the amount of dopant affected in a significant manner in the value the blue chromaticity ($-b^*$). As observed, ($-b^*$) increased with increasing the amount of Co^{2+} from 0 to 0.20, above that concentration, it decreased. As a result, the most vivid blue color was obtained for $Mg_{0.8}Co_{0.2}WO_4$ ($b^* = -46.7$).

Table 2.7 Color properties of $Mg_{1-x}Co_xWO_4$ (x = 0.1, 0.2, 0.3 and 0.2 (flux))

x	***L*****	***a*****	***b*****	***C*****	***h°***	***R* (%)**	***R** (%)**	***E***
0.10	49.12	1.47	-37.55	37.58	272.26	42	33	3.02
0.20	46.28	6.33	-46.97	47.48	277.68	56	38	2.94
0.30	43.80	4.33	-44.14	44.35	275.62	55	36	2.86
0.2(flux)	53.81	3.60	-43.00	43.15	274.8	70	50	3.00
$CoAl_2O_4$	44.80	2.10	-32.70	—				

Data for $CoAl_2O_4$ taken from ref. [37]

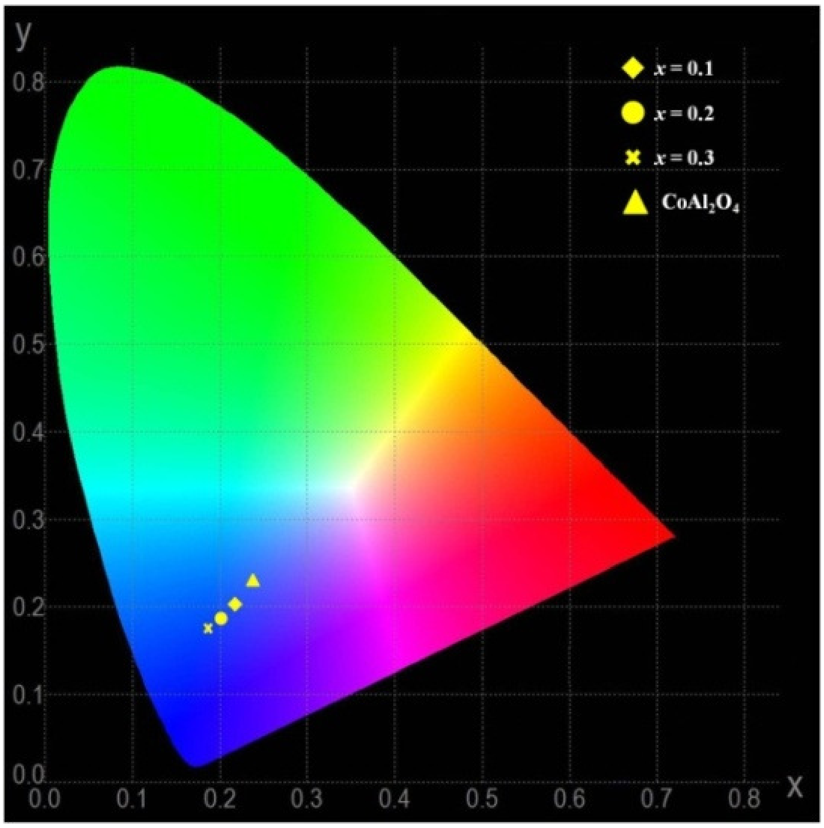

Figure 2.8 L^* (represent a black (L^*=0) /white (L^*=100) component of color), a^* (responsible for a red (a^*>0) /green (a^*<0), b^* (represent a yellow (b^*>0) /blue (b^*<0)) parameters of samples as a function of x.

Near infrared reflectance spectra were measured to examine the potential application of the samples as cool roof applications. NIR reflectance of $Mg_{1-x}Co_xWO_4$ (x = 0.1, 0.2, 0.3and 0.2 (flux) samples as a function of wavelength are shown in figure 2.9. Intensity of reflectance goes up from x = 0.1 to 0.2 sample. Around 50% of the energy in the solar irradiance spectrum is from near infrared irradiation (700 - 2000 nm). The reflectance of the samples in the 1100 nm region display reflectance is around 42 to 56%. The reflectance of $Mg_{0.8}Co_{0.2}WO_4$ prepared from the flux assisted solid state method shows a higher reflectance of 70% in the 1110 nm range. In comparison to the reflectance of $Mg_{0.8}Co_{0.2}WO_4$ (without flux), flux added sample shows more than 10% enhancement in the NIR reflectance. These pigments exhibit high reflectance in the NIR region (1100 nm), however, it decreases above 1100 nm due to the $^4T_{Ig}(F)$ to $^4T_{2g}(F)$ transition of Co^{2+} in the octahedral environment. From the SEM micrograph, we observed that particle size of flux added samples are smaller than that of the sample from the solid state method. Pigments possessing low absorbance in the NIR region can be considered as ideal for cool coating. For the cool colored pigments, this part of solar energy is expected to be reflected as much as possible.

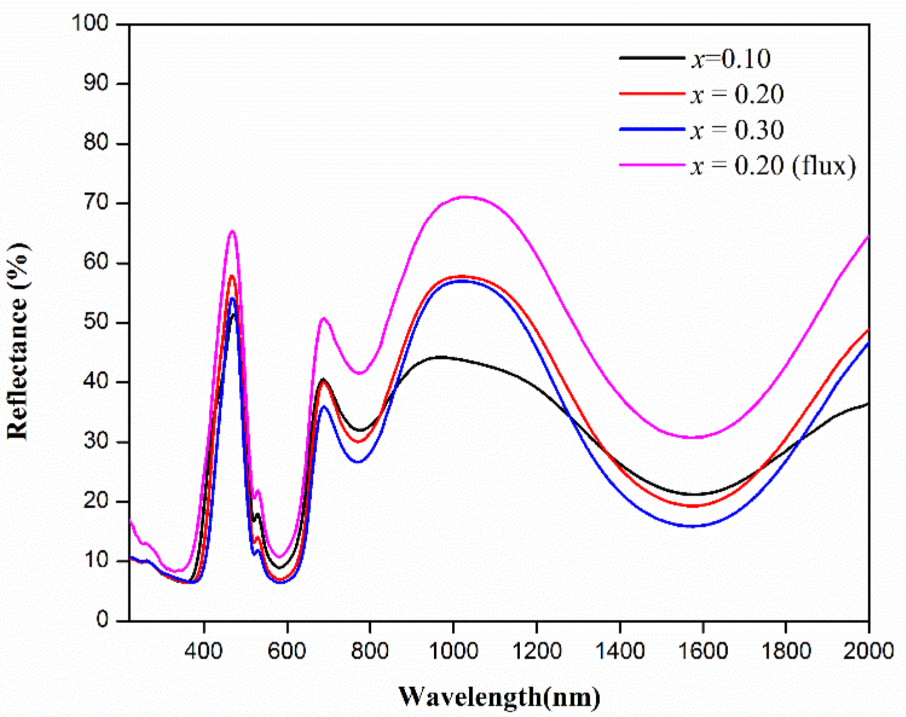

Figure 2.9 Reflectance spectra of $Mg_{1-x}Co_xWO_4$ (x = 0.1, 0.2, 0.3 and 0.2 (flux)).

The NIR solar reflectance spectra of samples synthesized by both SSR and flux added methods in comparison with ASTM Standard G173-03 [38] presented in figure 2.10. This gives the reflectance in the 750 - 2000 nm region. The optical band gap E_g can be calculated based on the Tauc equation 2.11 [39-41]:

$$F(R)h\nu = \alpha h\nu = A(h\nu - E_g)^n \rightarrow \qquad (2.11)$$

where α is the absorbance, A is the constant characteristic for material under study, h is the Planck constant, ν is the light frequency, and n is the constant determined by the electronic transition type (n =1/2, 2, 3/2, or 3 for allowed direct, allowed indirect, forbidden direct and forbidden indirect transition, respectively). Band gap can be determined from the plots of $(\alpha h\nu)^{1/2}$ as a function of $h\nu$ by extrapolating the linear portion of the curve to intersect the photon energy axis at zero absorption. The plots $(\alpha h\nu)^{1/2}$ versus $h\nu$, and the extrapolated indirect allowed band gap E_g values are given in table 2.7, respectively. The NIR solar reflectance (R^*) of samples synthesized by SSR and flux added methods are also given in table 2.7.

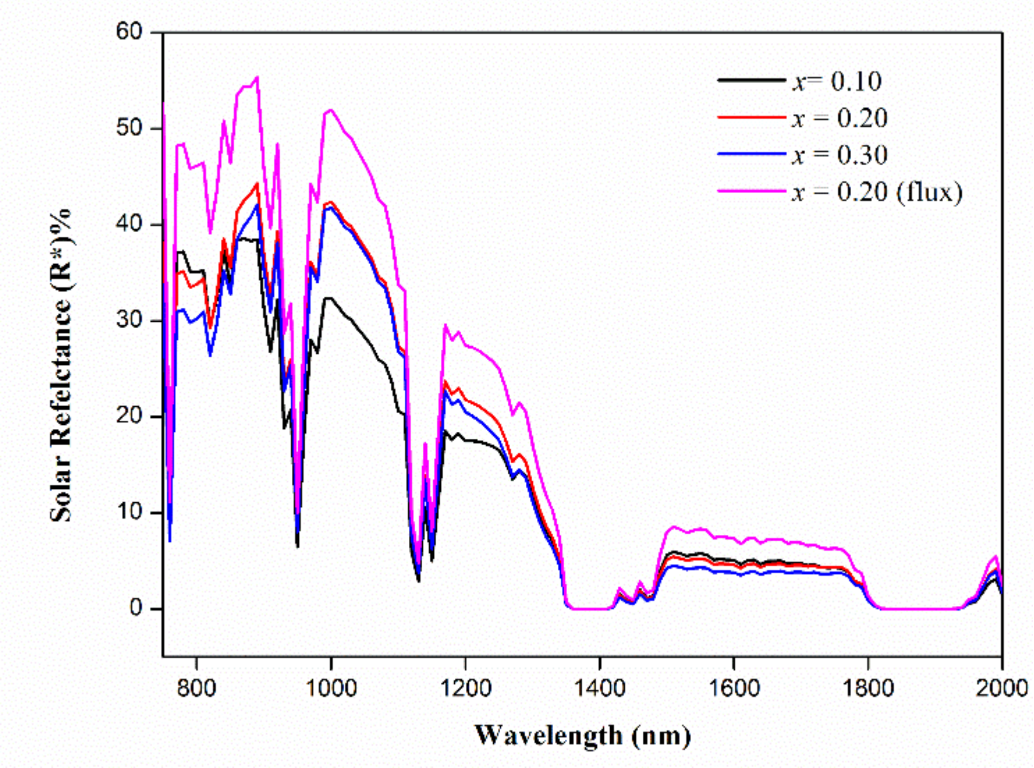

Figure 2.10 NIR solar reflectance spectra of $Mg_{1-x}Co_xWO_4$ (x = 0.1, 0.2, 0.3 and 0.2 (flux)).

2.3.4 *Thermal and Chemical Stability Testing*

Thermo-gravimetric analysis of the samples was investigated with a view to find out its thermal stability and the results clearly indicate that there is a negligible weight loss of the pigment. Thermo gravimetric analysis (TGA) was performed on $Mg_{0.8}Co_{0.2}WO_4$ in the temperature range 30 - 300°C, under an argon atmosphere at a heating rate of 20°C/min (Figure 2.11). For evaluating the chemical stability of the synthesized pigment $Mg_{0.8}Co_{0.2}WO_4$, we treated it with acid and alkali. For this, a small amount of weighing sample is mixed with 2% NaOH and 2% HCl and immersed for 1 hour with constant stirring. Then the pigment was filtered, washed with distilled water, dried and finally weighed. The color difference $\Delta E^*{}_{ab}$ was calculated from the data before and after each test using the equation 2.12 and is summarized in table 2.8. The smaller values of ΔE_{ab^*} indicate that the pigments are chemically stable towards the acid/alkali.

$$\Delta E^*{}_{ab} = \left[(L^*{}_{after} - L^*{}_{before})^2 + (a^*{}_{after} - a^*{}_{before})^2 + (b^*{}_{after} - b^*{}_{before})^2\right]^{1/2} \tag{2.12}$$

Table. 2.8 The color coordinates of $Mg_{0.8}Co_{0.2}WO_4$ after chemical resistance tests.

Sample	***L****	***a****	***b****	**$\Delta E_{ab}{}^*$**
$Mg_{0.8}Co_{0.2}WO_4$	46.28	6.33	-46.97	-
Acid	45.27	5.57	-44.24	2.39
Base	45.78	5.91	-46.20	1.01

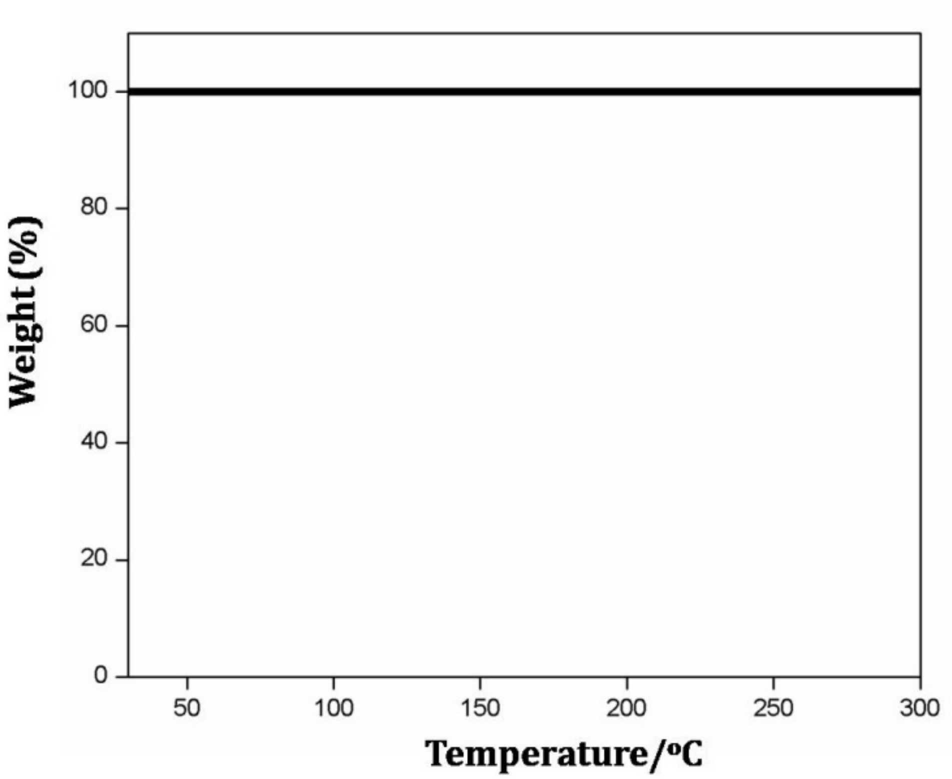

Figure 2.11 TGA of $Mg_{1-x}Co_xWO_4$ ($x = 0.2$) pigment from solid state method.

2.4 Conclusions

In the present work, we prepared new blue colored ceramic pigment with the doping of Co^{2+} in the monoclinic $MgWO_4$ host lattice other than spinels. The solid solutions of Co-$MgWO_4$ are formed at 1100°C for 12 h in the solid state method. While the flux added, the method used in this work let to obtain the pigments with high purity at relatively low temperature. The doping of Co^{2+} ions in the monoclinic $MgWO_4$ produces intense blue colors are obtained with relatively low amounts of Co (20 mol%), which is a lower amount in comparison with nonsubstituted $CoAl_2O_4$ spinel and Co_2SiO_4 olivine blue or violet pigments. Accordingly, an important reduction in the toxicity and cost of production of the obtained ceramic pigments may be accomplished. The doped Co^{2+} ions change the optical properties of the $MgWO_4$ host lattice. In the case of currently available blue pigments, the blue color is normally assigned to the incorporation of Co^{2+} in tetrahedral coordination. One of the major advantages of the present study is that the prepared pigments had intense blue color and higher NIR reflectance with the incorporation of Co^{2+} in the octahedral site with the low amount of cobalt.

2.5 References

1. R. K. Mason, Am. Ceram. Soc. Bull. 17 (1961) 167.
2. M. Dondi, M. Ardit, G. Cruciani, C. Zanelli, Am. Mineral. 99 (2014) 1736.
3. R. Pozas, V. M. Orera, M. Ocaña, J. Eur. Ceram. Soc. 25 (2005) 3165.
4. D. C. M. A. M. Oxides, C. C. Subcommittee, DCMA Classification and Chemical Description of the Mixed Metal Oxide Inorganic Colored Pigments, Metal Oxides and Ceramic Colors.
5. M. Llusar, A. Zielinska, M. A. Tena, J. A. Badenes, G. Monrós, J. Eur. Ceram. Soc. 30 (2010)1887.
6. M. Miyake, H. Nakamura, H. Kojima, F. Marumo, Am. Mineral. 72 (1987) 594.
7. A. E. Lavat, C. C. Wagner, J. E. Tasca, Ceram. Int. 34 (2008) 2147.
8. M. Llusar, T. Bermejo, J. E. Primo, C. Gargori, V. Esteve, G. Monrós, Ceram. Int. 43 (2017) 9133.
9. J. Zou, W. Zheng, Ceram. Int. 42 (2016) 8198.
10. B. Fromme, d-d Excitations in Transition-Metal Oxides, Springer-Verlag, Berlin, Heidelberg (2001).
11. L. Cornu, V. Jubera, A. Demourgues, G. Salek, M. Gaudon, Ceram. Int. 43 (2017) 13377
12. M. Dondi, C. Zanelli, M. Ardit, G. Cruciani, J. Am. Ceram. Soc. 94 (2011) 1025.
13. A. Forés, M. Llusar, J. A. Badenes, J. Calbo, M. A. Tena, G. Monrós, Green Chem. 2 (2000) 93.
14. D. Errandonea, F. J. Manjon, Prog. Mater Sci. 53 (2008) 711.
15. J. H. Zhao, T. Liu, S. S. Guo, J. Guan, X. L.Wang, Opt. Express 18 (2010) 18989.
16. V. B. Mikhailik, H. Kraus, V. Kaputstyanyk, M. Panasyuk, Y. Prots, V. Tsybulskyi, L.Vasylechko, J. Phys. Condens. Matter 20 (2008) 365219.
17. A. Sleight, Acta Crystallogr. Sect. B. 28 (1972) 2899.
18. R. Keeling, Acta Cryst. 10 (1957) 209.
19. E. Cavalli, A. Belletti, M. G. Brik, J. Phys. Chem. Solids 69 (2008) 29.
20. R. Shannon, Acta Crystallogr. Sect. A. 32 (1976) 751.
21. V. B. Kravchenko, J. Struct. Chem. 10 (1969) 139.
22. L. Pauling, J. Am. Chem. Soc. 51 (1929) 1010.
23. R. M. Wood, G. J. Palenik, Inorg. Chem. 37 (1998) 4149.

24. S. N. Rao, S. Vedanand, R. Ravikumar, R. V. S. S. N. Ravikumar, Y. P. Reddy, Solid State Commun. 92 (1994) 815.
25. S. Koide, Philos. Mag. 4 (1959) 243.
26. R. R. Kumar, P. D. B. C. V. Reddy, Cryst. Res. Technol. 30 (1995) 853.
27. Y. Tanabe, S. Sugano, J. Phys. Soc. Jpn. 9 (1954) 753.
28. A. B. P. Lever, J. Chem. Educ. 45 (1968) 711.
29. J. Reedijk, W. L. Driessen, W. L. Groeneveld, Recl. Trav. Chim. Pays-Bas 88 (1969) 1095.
30. C. K. Jørgensen, in Absorption Spectra and Chemical Bonding in Complexes, Pergamon press, Oxford, London (1962).
31. D. S. Gouveia, L. E. B. Soledade, C. A. Paskocimas, E. Longo, A. G. Souza and I. M. G. Santos, Mater. Res. Bull. 41 (2006) 2049.
32. I. B. Bersuker, Electronic Structure and Properties of Transition Metal Compounds: Introduction to the Theory, Wiley (2010).
33. W. B. Im, Y.-I. Kim, N. N. Fellows, H. Masui, G. A. Hirata, S. P. DenBaars and R. Seshadri, Appl. Phys. Lett. 93 (2008) 091905.
34. A. L. Allred, J. Inorg. Nucl. Chem. 17 (1961) 215.
35. A. M. Srivastava, Opt. Mater. 31 (2009) 881.
36. V. Dimitrov, T. Komatsu, J. Solid State Chem. 196 (2012) 574.
37. M. Ocaña, J. P. Espinós, J. B. Carda, Dyes Pigm. 91 (2011) 501.
38. Standard tables for reference solar spectral irradiances: Direct normal and hemispherical on 37° tilted surface; ASTM International: West Conshohocken, Pennsylvania, United States (2012).
39. J. Tauc, R. Grigorovici, A. Vancu, Phys. Status Solidi B. 15 (1966) 627.
40. M. Piątkowska, H. Fuks, E. Tomaszewicz, A. E. Kochmańska, Ceram. Int. 43 (2017) 7839.
41. M. Pawlikowska, H. Fuks, E. Tomaszewicz, Ceram. Int. 43 (2017) 14135.

3

MONOCLINIC $LaGa_{1-x}Mn_xGe_2O_7$: A NEW BLUE CHROMOPHORE BASED ON Mn^{3+} IN TRIGONAL BIPYRAMIDAL COORDINATION WITH LONGER APICAL BONDS

New blue colored Mn^{3+} *doped* $LaGa_{1-x}Mn_xGe_2O_7$ *(x = 0. 0.1, 0.2, 0.3 and 0.4) inorganic pigment was prepared by the solid state route. Here we introduce* Mn^{3+} *ions in the gallium site of monoclinic* $LaGaGe_2O_7$*. In the host lattice of monoclinic* $LaGaGe_2O_7$ *the* Ga^{3+} *ions are occupying the distorted five coordinated site. Substitution of* Mn^{3+} *in the* $LaGaGe_2O_7$*, host lattices changes the color from white (x = 0) to blue (x = 0.1, 0.2, 0.3 and 0.4). The blue color of this developed* $LaGa_{1-x}Mn_xGe_2O_7$ *is mainly due to the absorption in the region of 1.8 - 2.5 eV regions. This absorption arises due to the d–d transition taking place from the crystal field splitting of* Mn^{3+} *in the trigonal bipyramidal site. Mn–O apical bond lengths play a key role in the d–d component of this transition. The pigment powders were characterized by XRD and UV- visible spectroscopy.*

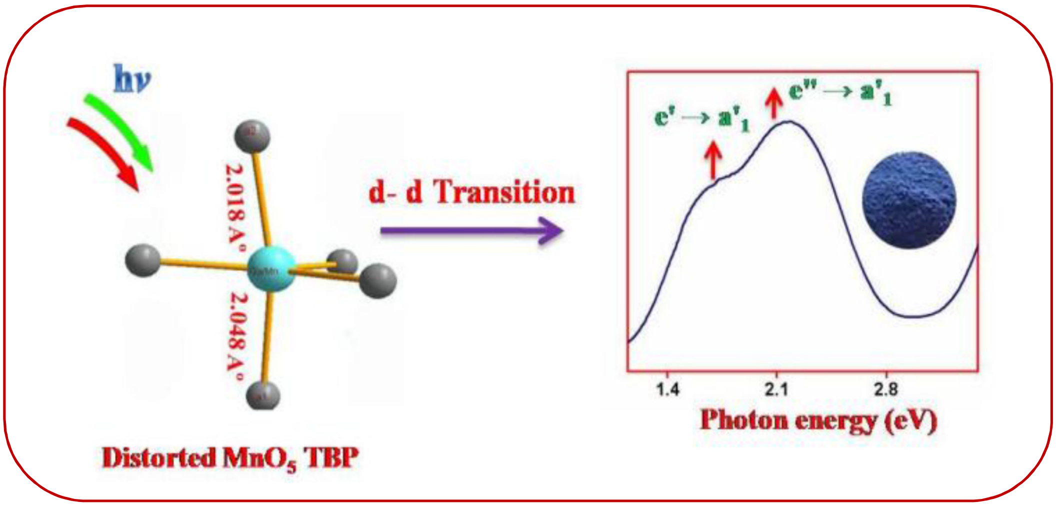

3.1 Introduction

Nature of d-electrons in the transition metals (TM) are of great importance in several phenomena that occur in the TM based compounds. Transitions between the d-states of these metal ions are of great influence on the optical property and these transitions determine the color. V, Cr, Mn, Fe, Co, Ni, and Cu are the most commonly used chromophores in pigment systems, which have incompletely filled d-orbitals [1]. Inorganic green pigments are usually applied ceramic tiles, inks, and paints. Among the various colors perceptible to the human eye, blue is a special color that is associated with trust, loyalty, and understanding. Nowadays, the search for new intense blue inorganic pigments that are environmentally friendly, cheap, and durable is of prime importance in pigment industry but remains a key challenge.

Currently used inorganic blue pigments are cobalt blue ($CoAl_2O_4$), ultramarine blue and Prussian blue ($Fe_4[Fe(CN)_6]_3$). In cobalt blue the attribution of color is due to the spin allowed the d-d transition of Co^{2+} in the tetrahedral coordination, whereas in ultramarine blue it is based on the absorption in the S^{3-} radical anion, and in Prussian blue the color is associated with the intervalence charge transfer taking place from the Fe^{2+} to Fe^{3+} ion [2, 3]. It is clear that the environment of the transition metal ion, which is determined by the host lattice, considerably affects the optical properties of a compound.

Subramanian *et al.* discovered new blue inorganic oxide materials with the introduction of Mn^{3+} in the TBP sites of hexagonal $YInO_3$, $ScGaZnO_4$, $LuGaZnO_4$ and $LuGaMgO_4$ [4, 5]. In addition to the individual ion and its oxidation state, the ionic environment markedly affects absorption phenomena. Recently a new blue chromophore based on $Sr_2(Mg,Mn)Ge_2O_{7+\delta}$ was synthesized which has a melilite type structure [6]. Crystal structure of $Sr_2(Mg,Mn)Ge_2O_{7+\delta}$ contains the rarely found $Mn^{III}O_5$ trigonal bipyramid (TBP) and the GeO_5 square pyramid, this might result from the oxidation of Mn^{2+} ions due to the uptake of an interstitial oxygen. In the case of hexagonal $YIn_{1-x}Mn_xO_3$ the origin of blue color is due to the d–d transition taking place from the Mn $d'_{(x^2-y^2,\, xy)} \rightarrow d'_{z^2}$ state. Shorter Mn–O apical bond lengths play a key role in the d-d component of this transition and also favorable for the layered arrangements in hexagonal perovskites [4]. Recently reported a purple inorganic oxide material based on hexagonal $YGaO_3$ substituted with Mn^{3+} at the Ga^{3+} site [7].

The absorption spectrum of $YGa_{1-x}Mn_xO_3$ similar to the corresponding $YIn_{1-x}Mn_xO_3$ except that the lower energy band is assigned to transition from $d'_{(x^2-y^2, xy)} \rightarrow d'_{z^2}$ blue shifted by about 0.3 - 0.5 eV. The blue shift in the absorption maxima is due to the slightly shorter Ga–O apical bond length in $YGaO_3$ compared to that of $YInO_3$. Also, this work shows that the color of the TBP coordinated Mn^{3+} could be tuned by altering the host material possessing different Mn–O apical bond lengths [7]. The color of a compound depends on the magnitude of crystal field splitting, which depends on the structure of the compound and d-orbital–ligand interaction [8]. The extent of crystal field splitting strongly depends on nature and the coordination environment of the ligands [9].

The germanates of the type $MRGe_2O_7$ (M = Al^{3+}, Ga^{3+} or Fe^{3+} and R = rare earth ion) have been reported in the early 1980s, which belong to the monoclinic $AlNdGe_2O_7$ type structure (Figure 3.1) [10]. These kinds of compounds are of great interest in laser crystal physics [11]. The luminescence study of these compounds provides much valuable information for optical applications, $LaAlGe_2O_7$ doped with Tb^{3+} and Tm^{3+} shows intense green and blue light emissions, respectively [12, 13]. However, no reference was found in the literature describing the optical studies of Mn^{3+} doped $LaGaGe_2O_7$ this work is just the first step. Recent times research efforts are being made to develop and explore cobalt free blue chromophores for environmentally benign pigment applications. However, a few host structures having a Mn^{3+} ion in their geometry have been found so far. In this respect, there is a growing need for finding out host structures incorporating Mn^{3+} in the trigonal bipyramidal geometry. In the present investigation, we prepared new blue pigment with the introduction of Mn^{3+} in the monoclinic host other than the hexagonal perovskites and we observed some changes in the absorption spectrum of Mn^{3+} in the TBP site from that observed in the hexagonal $YIn_{1-x}Mn_xO_3$.

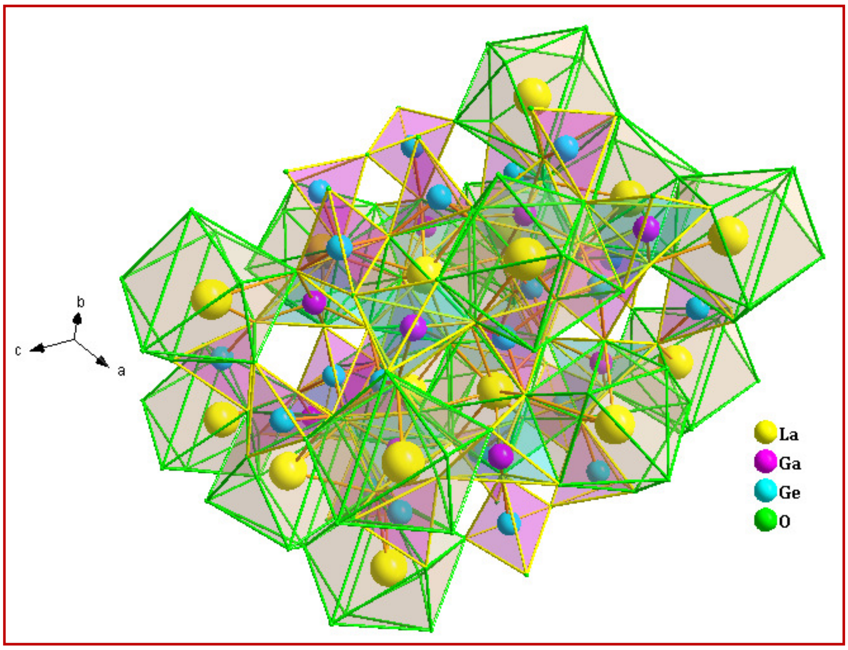

Figure 3.1 Representation of crystal structure $LaGaGe_2O_7$.

3.2 Experimental Section

3.2.1 *Materials and Synthesis*

Samples of Mn^{3+} doped $LaGaGe_2O_7$ prepared by the conventional solid state method. For this purpose chemicals such as La_2O_3 (Sigma Aldrich-99%), Ga_2O_3 (Sigma Aldrich-99%), Mn_2O_3 (Aldrich-99.9%) and GeO_2 (Aldrich-99.9%) were mixed with a stoichiometric proportion in the acetone medium. In the solid state reaction method, flux is added to improve the crystallinity and lower the reaction temperature, here H_3BO_3 (1 wt. %) was used as a flux. The mixed product was dried in an oven at 100°C for 30 min. The process of mixing and drying was repeated thrice to get a homogeneous mixture. Finally, the dried mixtures were placed in platinum crucibles and calcined in an electric furnace at 1100°C for 6 h, using a heating rate of 5°C /min. The calcined samples were ground thoroughly into fine powders in an agate mortar for further studies.

3.2.2 *Characterization*

The crystal structure and phase purity of the synthesized $LaGa_{1-x}Mn_xGe_2O_7$ samples were obtained with the aid of the PANalytical X'pert Pro diffractometer (Ni-filtered Cu Kα radiation, $\lambda = 1{\cdot}5406$ Å). The data were recorded over the 2θ range of 10° - 90°. Rietveld refinement of X-ray diffraction pattern was carried out using X'Pert

HighScore Plus software. The morphology of the prepared samples was examined by scanning electron microscopy (JEOL JSM-5600 LV SEM). Temperature dependent dc magnetic measurements *M(T)* was performed in PPMS from Quantum Design. For the characterization of the pigment quality of the samples (color parameters), diffuse reflectance spectra were recorded (220 - 2500 nm) employing a UV-visible spectrometer (Shimadzu UV-3600) using PTFE as the reference. For the color analysis, the CIE 1976 $L^*a^*b^*$ colorimetric method was used, as recommended by the Commission Internationale de l'Eclairage (CIE). In this method, L^* is the lightness axis [black (0) to white (100)], a^* is the green (−ve) to red (+ve) axis, and b^* is the blue (−ve) to yellow (+ve) axis. The parameter C^* (chroma) represents saturation of the color and is defined as $C^* = [(a^*)^2 + (b^*)^2]^{1/2}$ and $h° = tan^{-1}(\frac{b^*}{a^*})$ represents the hue angle.

3.3 Results and Discussion

3.3.1 *Structural Analysis*

The structural characterization was carried out by using powder X-ray diffraction. The X-ray diffraction (XRD) patterns of the calcined powders of all the samples were taken to confirm the formation of the phase and structural identification are obtained from X-ray powder diffractometer using Cu-Kα radiation in a 2θ range of 10° to 90°. $LaGaGe_2O_7$ crystals belong to a large family of C^5_{2h}-monoclinic compounds with the $NdAlGe_2O_7$ structure. In $LaGaGe_2O_7$, the rare-earth ions are separated by GaO_5 and Ge_2O_7 polyhedra and the oxygen coordination around the rare-earth ion is in 9-fold (Figure 3.2). In the monoclinic unit cell of $LaGaGe_2O_7$ (Z = 4), four La^{3+}, four Ga^{3+}, eight Ge^{4+} and fourteen O^{2-} occupy the 4*e* positions of C_1 symmetry.

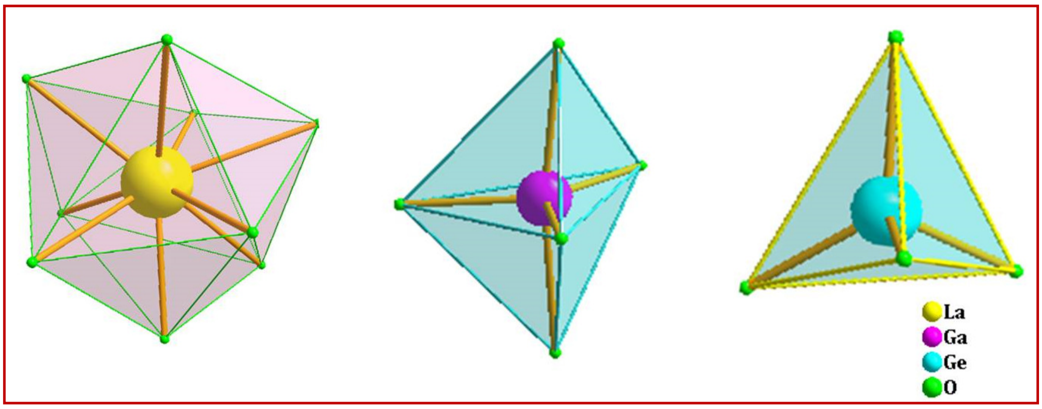

Figure 3.2 Representation of coordination polyhedra in $LaGaGe_2O_7$.

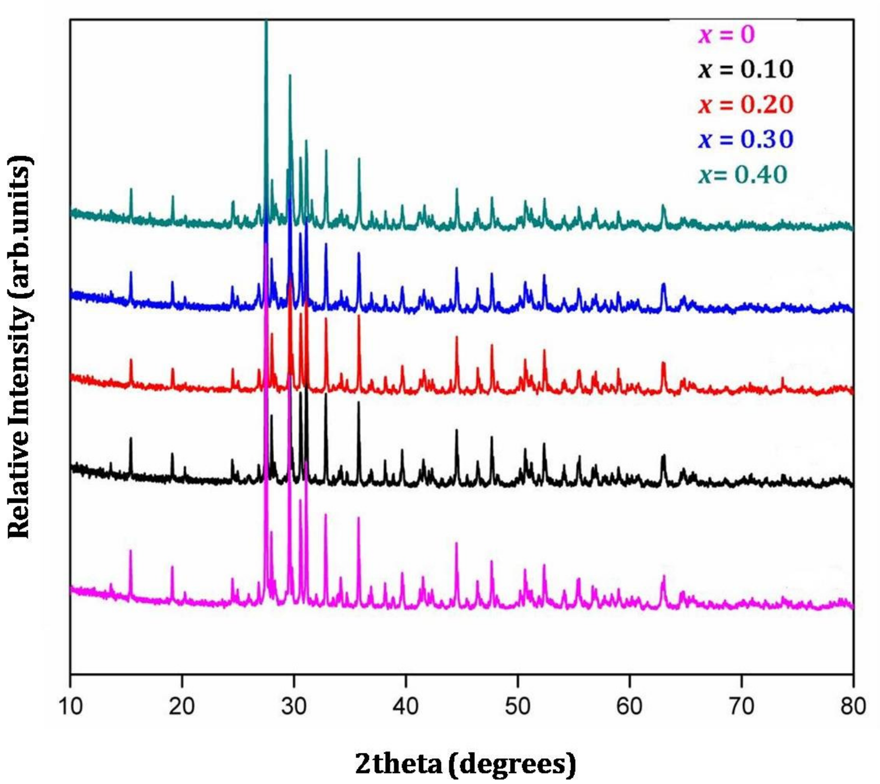

Figure 3.3 XRD patterns of $LaGa_{1-x}Mn_xGe_2O_7$ (x = 0, 0.1, 0.2, 0.3 and 0.4).

Figure 3.3 shows the XRD patterns of the samples prepared via the solid-state method. All the reflections in the XRD pattern can be indexed according to the powder diffraction file 00-041-0969 and $LaGa_{1-x}Mn_xGe_2O_7$ crystallizes in monoclinic structure with a space group of $P2_1/c$. The crystalline nature of the sample is evident from the powder. Although the lattice parameters of the doped systems changed due to the ionic radii mismatch, the crystal structures remained monoclinic (Table 3.1). The doping of Mn^{3+} gives rise to a progressive increase in the lattice parameters and unit cell volume up to 20 mol% of Mn^{3+}. Above 20 mol% of the doping concentration of Mn^{3+} shows decreases in the lattice parameter.

Table 3.1 Lattice parameters of $LaGa_{1-x}Mn_xGe_2O_7$ (x = 0, 0.1, 0.2, 0.3 and 0.4).

Composition	***a* (Å)**	***b* (Å)**	***C* (Å)**	**β(degrees)**	***V* (Å^3)**
x = 0	7.3114 (3)	6.6360(3)	12.9608(4)	117.4300	558.1354
x = 0.1	7.3144(4)	6.6342(4)	12.9624(4)	117.4248	558.3203
x = 0.2	7.3177(4)	6.6309(4)	12.9718(4)	117.4423	558.6127
x = 0.3	7.3171(4)	6.6277(4)	12.9713(3)	117.4377	558.2990
x = 0.4	7.3168(3)	6.6265(4)	12.9697(4)	117.4414	558.0858

Variation of lattice parameters *a* and *c* with Mn^{3+} concentrations are shown in figure 3.4. This shows that up to 20 mol% doping concentration the values of *a* and *c* goes on increasing, further doping of Mn^{3+} the values of lattice parameter start to decrease. The unit cell volume slightly increases from 558.13 to 558.61. This expansion is due to the slightly increased ionic radii of Mn^{3+} (58 pm) compared to Ga^{3+} (55 pm). Shrinkage in unit cell volume with higher doping occurs; this raises the possibility that some Mn^{3+}may be in the Mn^{4+}oxidation state.

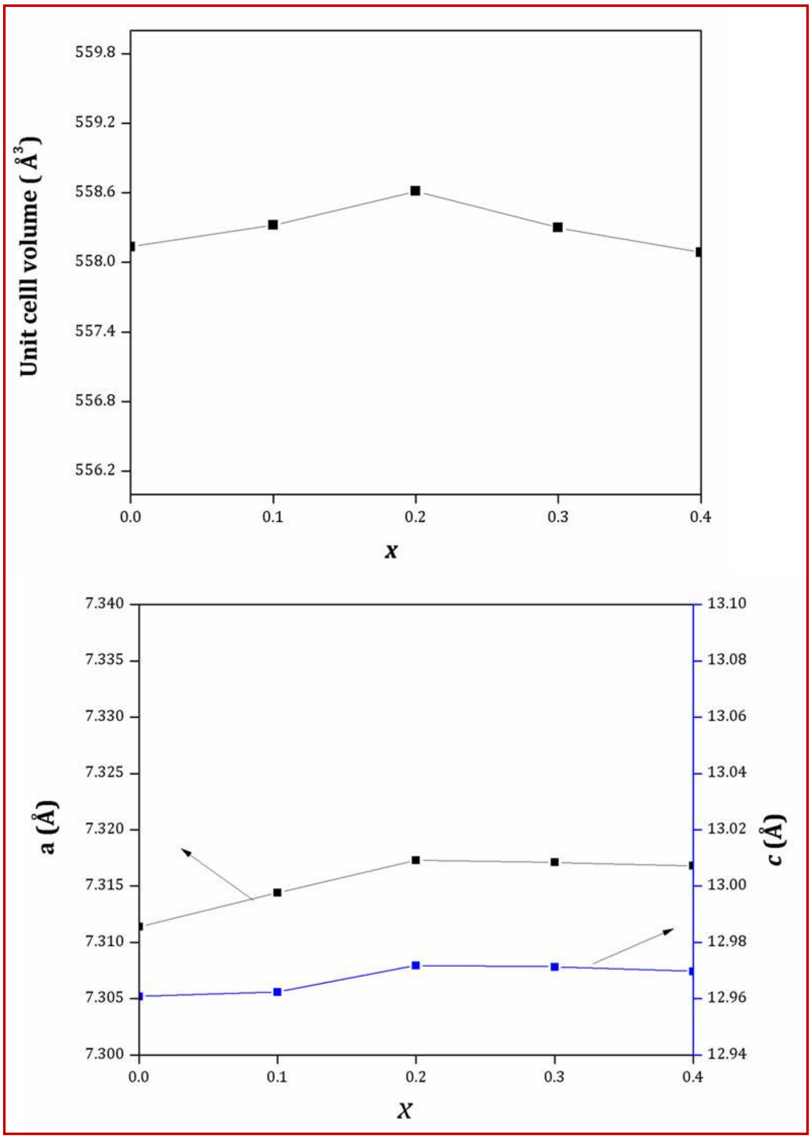

Figure 3.4 Variation of unit Cell parameter *a* and *c* (bottom) and unit cell volume (top) with Mn^{3+} doping in the $LaGaGe_2O_7$.

Crystal structure $LaGa_{1-x}Mn_xGe_2O_7$ was refined based on the experimental powder diffraction data by Rietveld analysis (Figure 3.5). In order to determine the quality of final refinement, reliability factors are defined to compare the difference between the observed pattern and calculated profile. The weighted profile reliability (R_{wp}) factor is the more valuable, for a complex phase (monoclinic to triclinic), a value < 0.15 is good. The refinement results of $LaGa_{0.8}Mn_{0.2}Ge_2O_7$ are shown as a typical example in Table 3.2.The final reliability factors are R_{wp} = 13.91%, R_p= 10.82% and GoF = 1.11

Table 3.2 Rietveld refinement data of LaGa$_{0.8}$Mn$_{0.2}$Ge$_2$O$_7$ at room temperature.

Atoms	**site**	*x*	*y*	*z*
La	4*e*	0.764871 (4)	0.14345 (4)	0.02365 (4)
Ga	4*e*	0.790730 (3)	0.391102 (3)	0.266216 (4)
Mn	4*e*	0.790730 (3)	0.391102 (3)	0.266216 (4)
Ge1	4*e*	0.790654 (4)	0.654471 (4)	0.045139 (4)
Ge2	4*e*	0.295782 (3)	0.406011 (3)	0.219268 (4)
O1	4*e*	0.574604 (3)	0.867119 (2)	0.014767 (3)
O2	4*e*	0.782631 (3)	0.106881 (2)	0.208647 (3
O3	4*e*	0.562742 (2)	0.381692 (2)	0.300715 (3)
O4	4*e*	0.01036 (3)	0.325342 (3)	0.421378 (3)
O5	4*e*	0.766044 (3)	-0.00442 (4)	0.431423 (3)
O6	4*e*	0.819558 (3)	0.433638 (3)	0.134616 (3)
O7	4e	0.148757 (3)	0.188868 (3)	0.1890 (4)

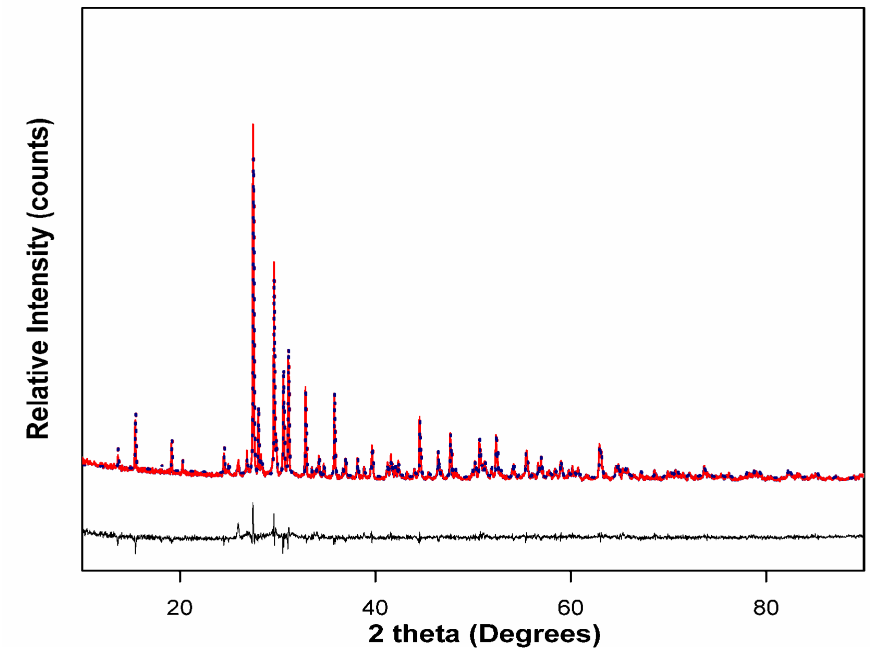

Figure 3.5 Rietveld refinement of the structure of LaGa$_{0.8}$Mn$_{0.2}$Ge$_2$O$_7$.The observed (red solid line), calculated (blue dotted) and difference (at the bottom).

Table 3.3 shows the selected Ga/Mn–O bond distances trigonal bypiramidal site in $LaGa_{1-x}Mn_xGe_2O_7$ (x = 0.1, 0.2, 0.3 and 0.4). In ideal trigonal bipyramid the two apical bonds are identical, when different cations enter the bipyramids the two apical bonds are not identical and they have been classified into two categories. In Type I the three basal M–O bonds shorter than the two apical ones and the bipyramid shows not much distortion. In Type II one of the apical bonds is shorter and the other one longer than the three basal ones: here the cation significantly off-centered from the basal plane, and pointing towards one of the corners [14]· Here the synthesized $LaGa_{1-x}Mn_xGe_2O_7$ (x = 0.1 and 0.2) in which the two apical bonds (ap_1 and ap_2) are longer than the three basal M–O bonds (e_1, e_2 and e_3), thus substitution of Mn^{3+} will not cause much distortion in the bipyramids.

Table 3.3 Ga/Mn–O bond distances (Å) in $LaGa_{1-x}Mn_xGe_2O_7$ (x = 0.1, 0.2, 0.3 and 0.4).

x	**0.1**	**0.2**	**0.3**	**0.4**
Ga/Mn-Oa_{P1}	2.0427	2.0480	1.9890	2.2738
Ga/Mn-Oa_{P2}	1.9960	2.0180	1.7948	1.5419
Ga/Mn-Oe_1	1.8175	1.9172	1.9711	1.8041
Ga/Mn-Oe_2	1.8241	1.8358	1.8655	1.9148
Ga/Mn- Oe_3	1.9576	1.9603	1.8557	1.9538
BVS	3.17	2.95	3.46	3.44

Above 20 mol% of the doping concentration, one of the apical bonds is longer and the other one is shorter than the three basal bonds, this may be due to the more distortion in the bipyramids. We calculate the bond valence sum of all the samples by using Pauling's BVS rule $V_{ij} = e^{R0-Rij/B}$, where R_0 and R_{ij} are expected and the experimentally determined bond length between the atoms, B is a constant (0.37 Å) [15] and the value of R_0 (1.76 Å) for Mn–O. From this calculation, we can see that the BVS of x = 0.3 and 0.4 are over bonded and have more deviations from the value of 3^+ oxidation state this may be due to the presence of Mn^{4+} (Table 3.3).

3.3.2 *Color Analysis*

To understand the origin of this blue color, we measured diffuse reflectance spectra using (Shimadzu UV-3600) UV-vis spectrometer. Coloring performance of Mn^{3+} bearing pigments very much depends on its coordination environment. Optical absorption spectra of the $LaGa_{1-x}Mn_xGe_2O_7$ (x = 0, 0.1, 0.2, 0.3 and 0.4) is shown in figure 3.6. The band gap of undoped $LaGaGe_2O_7$ lies in the range of 3.3 eV. As we introduced the Mn^{3+} in the gallium site of $LaGaGe_2O_7$, two new absorption bands are observed in all doped samples. The D_{3h} crystal-field symmetry of bipyramidal oxygen ions around the Mn^{3+} ion splits the Mn 'd' levels into three components e" (d_{xz},d_{yz}), e' ($d_{x^2-y^2}$,d_{xy}) and a'$_1$ (d_{z^2}) in figure 3.7 [16]. The e" orbitals directed away from the apical oxygens have the lowest energy, due to their small overlap with O_{2p} orbitals. Next highest in energy e' orbitals strongly hybridize with the O_{2p} orbitals. Finally, a'$_1$ orbital has the highest energy, the d_{z^2} orbital remains empty in the ground state. Transitions to this unoccupied orbital will be of prime importance to the observed optical spectrum. The blue color of $LaGa_{1-x}Mn_xGe_2O_7$ is mainly due to the absorption in the 1.7 - 2.5 eV energy region [17]. This absorption arises due to the symmetry-allowed optical transitions from $d'_{(x^2-y^2,xy)} \rightarrow d'_{z^2}$ and $d'_{(xz,yz)} \rightarrow d'_{z^2}$, (symmetry forbidden transition) and here the corresponding d-states hybridized with O_{2p} orbital. Usually, the absorption spectra of Mn^{3+} in TBP site will give an intense absorption band in the 1.7eV region and a weak one around the 2.1 eV region [17]. TBP site of $LaGa_{1-x}Mn_xGe_2O_7$ is in a distorted environment, there is a small splitting in the absorption band located at the 2 eV region of all samples; this is similar to what appears in the absorption spectra of $YIn_{1-x}Mn_xO_3$. An ideal TBP will not give such type of splitting in the 2 eV region, this kind of splitting has not been observed in the $ScGa_{1-x}Mn_xZnO_4$ in which the TBP possesses full D_{3h} symmetry of an ideal one [10]. The absorption band located in the 3 - 4.5 eV region is due to the transition taking place from the $O_{2p} \rightarrow$ Mn d'_{z^2} orbital [18].

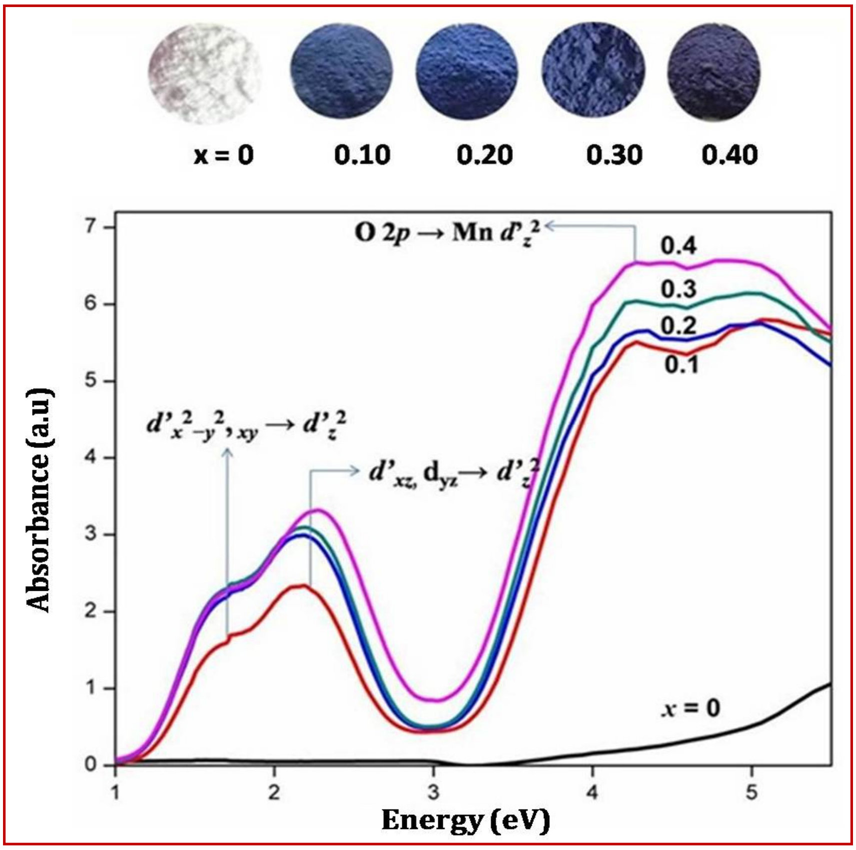

Figure 3.6 Absorbance spectra of $LaGa_{1-x}Mn_xGe_2O_7$ (x = 0, 0.1, 0.2, 0.3 and 0.4).

But in our case the absorption spectra of $LaGa_{1-x}Mn_xGe_2O_7$ (x = 0, 0.1, 0.2, 0.3 and 0.4) shows a weak intense band in the 1.7 eV region and a strong intense band in the 2.1 eV region. We inferred that the additional loss of intensity in the 1.7 eV region is due to the diminished hybridization strength of Mn d_{z^2} orbitals with O_{2p} orbitals due to their longer Mn–O apical bond lengths (Figure. 3.6)[19]. We proposed that the increased intensity of absorption band arises from the $d'_{(xz,yz)} \rightarrow d'_{z^2}$ transition is due to the close proximity of spin allowed and spin forbidden transition, these close proximity of the excited states lead to strong mixing through spin-orbit coupling. The mixing causes an increase of the intensity and bandwidth of the spin-forbidden transition [20]**.** Longer apical Mn–O bonds in $LaGa_{1-x}Mn_xGe_2O_7$ produce smaller ligand field around Mn^{3+} thus decreasing the energy separation between the e' and e" and a'_1 orbitals**.** Subramanian et al. pointed out the importance of Mn–O apical bonds in $YIn_{1-x}Mn_xO_3$, shorter Mn–O apical bonds favors effective hybridization with O_{2p} orbital, this will result in the origin of blue color. In the present system $LaGa_{1-x}Mn_xGe_2O_7$ all the doped samples possess longer Mn–O apical bonds, this situation also favors the development of blue color.

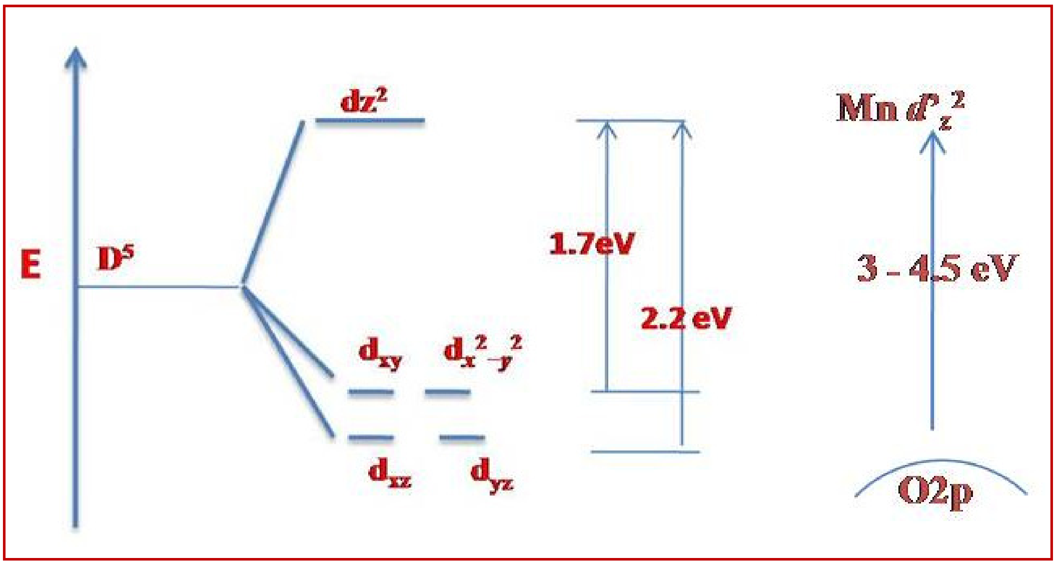

Figure 3.7 Crystal field splitting of Mn^{3+} in TBP site of $LaGaGe_2O_7$.

The *L*a*b** parameters of all synthesized pigments are shown in table 3.4. From this table, we can see that the amount of dopant affected in a significant manner in the value of -*b**, as the doping concentration increases up to 20 mol% -*b** value increases and thereafter decrease. The dopant also affects the lightness (*L**) which decreases (darker color) with increasing of Mn^{3+} content. From these parameters, it can also be concluded that the optimum pigment concentration (best color with lower doping level) was that containing a 20 mol% of Mn^{3+}.

Table 3.4 Color properties of $LaGa_{1-x}Mn_xGe_2O_7$ (x = 0, 0.1, 0.2, 0.3 and 0.4).

Sample	L^*	a^*	b^*	C^*	$h°$	NIR reflectance (%)
x = 0.1	49.52	9.7	-27.81	29.46	289	68
x = 0.2	45.77	14.92	-35.12	38.15	293	60
x = 0.3	44.62	12.58	-28.72	31.35	294	59
x = 0.4	42.82	11.13	-20.41	23.25	298	57

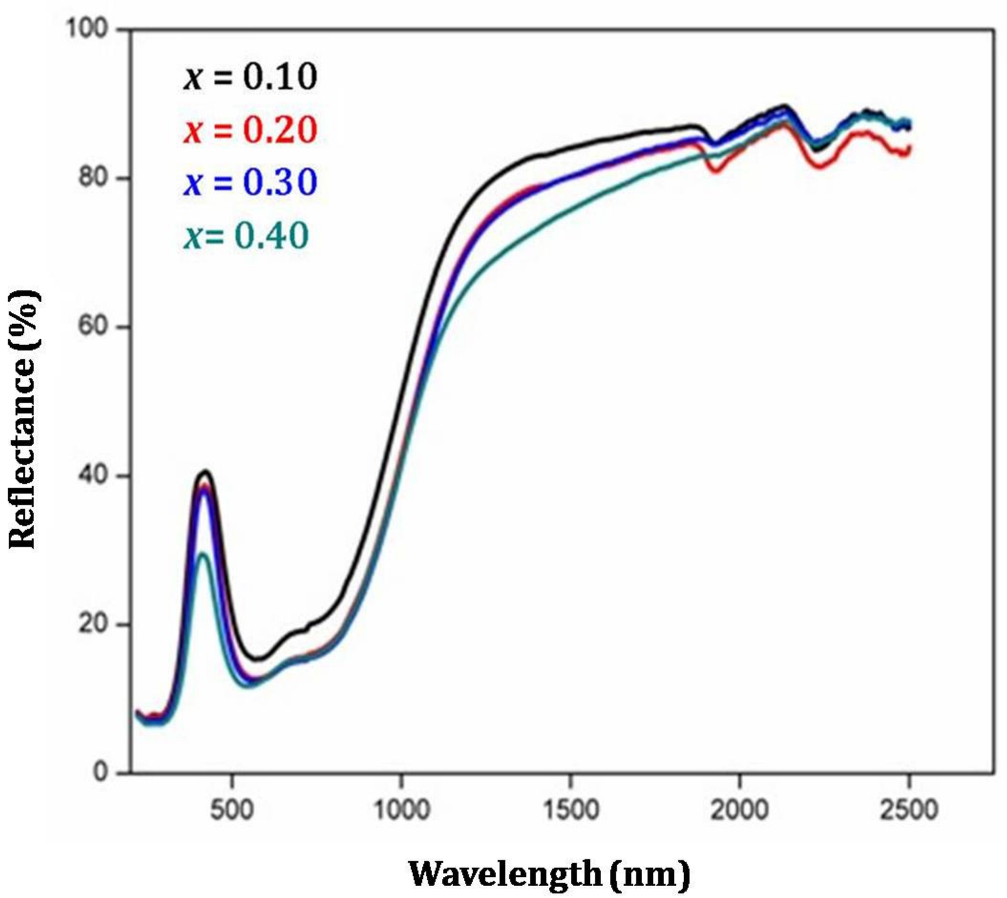

Figure 3.8 Reflectance spectra of $LaGa_{1-x}Mn_xGe_2O_7$ (x = 0.1, 0.2, 0. 0.4).

The NIR reflectance of $LaGa_{1-x}Mn_xGe_2O_7$ (x = 0.1, 0.2, 0.3 and 0.4) samples is given in figure 3.8. Pigments possessing low absorbance in the NIR region can be considered as ideal for cool coatings. In the case of $LaGa_{1-x}Mn_xGe_2O_7$ NIR reflectance enhanced up to 68% in the 1100 nm region for x = 0.1. From the NIR reflectance spectra, we can see that increasing of doping concentration decreases the reflectance. These changes in the reflectance spectra can be analyzed based on particle size. From the microstructure analysis, we find that particle size increases as the Mn^{3+} concentration increases. Increasing of particle size decreases the reflectance. The synthesized samples show more absorbance in the UV region with increasing the Mn concentration indicating as promising UV absorbers.

3.3.3 *Morphological Studies*

The homogeneous and crystalline nature of the sample can be observed in the SEM photographs figure 3.9. All the samples have a particle size in the range of 1 - 2 μm. From the micrograph, it is clear that the particles are distributed uniformly. As the concentration of Mn^{3+} increases, the particle size also increases. Particle size influences the reflectance spectrum also, where the reflectance decreases with increasing doping concentration.

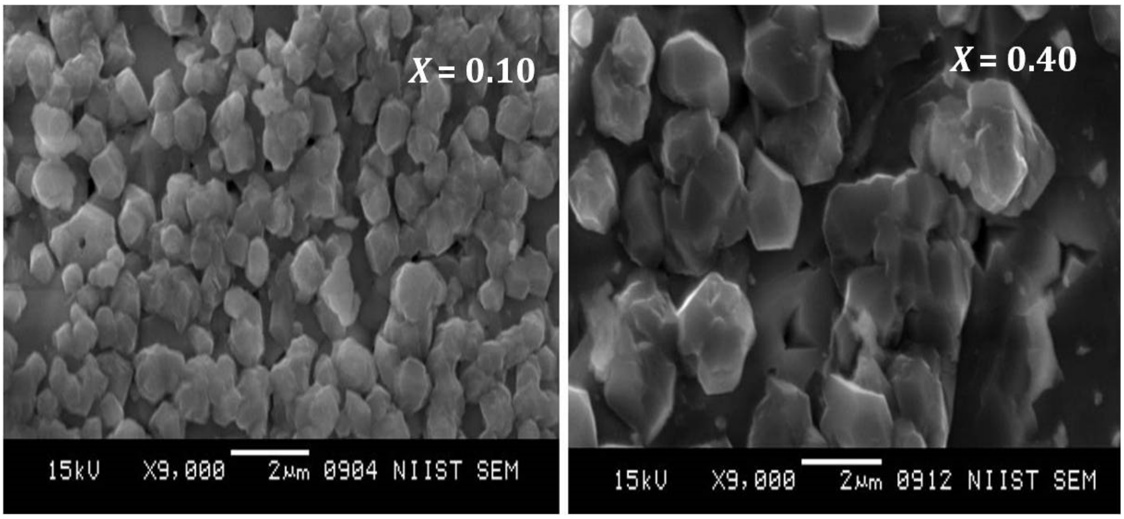

Figure 3.9 SEM photographs of $LaGa_{1-x}Mn_xGe_2O_7$ (x = 0.1 and 0.4**).**

3.3.4 *Magnetic Properties*

The temperature dependence of magnetic susceptibility $\chi(T)$ and its inverse susceptibility $\chi^{-1}(T)$ measured in a field of 500 Oe is plotted in the figure. 3.10. In the powder X-ray diffraction (XRD) patterns of the calcined powders of Mn^{3+} doped $LaGaGe_2O_7$, doping of Mn^{3+} gives rise to a progressive increase in the lattice parameters up to 20 mol% of Mn^{3+}. Above 20 mol% the doping of Mn^{3+} decreases the lattice parameter, this raises the possibility that some Mn^{3+} may be in the Mn^{+4} oxidation state. In order to confirm the presence of Mn^{4+} along with Mn^{3+} in the $LaGa_{0.6}Mn_{0.4}Ge_2O_7$, magnetic susceptibility measurements were conducted. As can be seen in the figure, the inverse susceptibility satisfactorily follows the Curie-Weiss law given by $\chi = C/(T - \theta)$, where C is the Curie constant and θ is the Weiss constant. The theoretical effective Bohr magneton, μ_{eff}, was calculated from the equation, $\mu_{eff} = 2[S(S+1)]^{1/2}$. The observed value of μ_{eff} is lower than that one would expect for a free Mn^{3+} ion (4.90). The experimental μ_{eff} value of Mn^{3+} in $LaGa_{0.6}Mn_{0.4}Ge_2O_7$ is 4.47 this lowering of magnetic moment confirms the presence of Mn^{4+} along with Mn^{3+} in the synthesized samples $LaGa_{1-x}Mn_xGe_2O_7$(x = 0.3, 0.4). In general, up to 20 mol% we expect the presence of Mn^{3+} alone above 20 mol% of the doping concentration, presence of Mn^{4+} is also seen in the prepared samples.

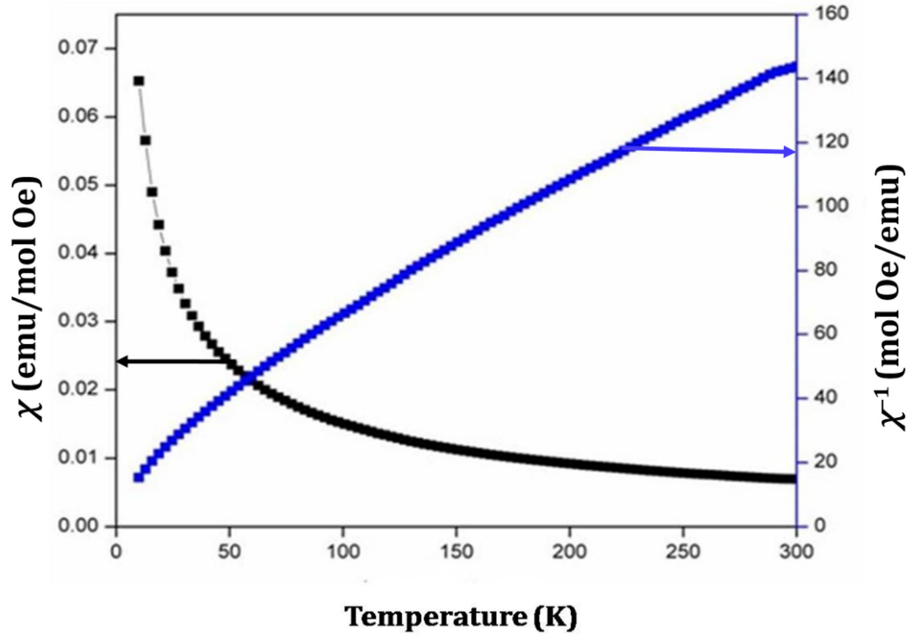

Figure 3.10 Temperature dependence of χ and χ^{-1} for $LaGa_{0.6}Mn_{0.4}Ge_2O_7$.

3.4 Conclusions

In the present work, we prepared new blue inorganic oxide material with the introduction of Mn^{3+} in the TBP site of monoclinic $LaGaGe_2O_7$ other than in the layered perovskites. In the absorption spectra of $LaGa_{1-x}Mn_xGe_2O_7$ (x = 0.1, 0.2, 0.3 and 0.4) two absorption bands are observed with the intensity of symmetry allowed transition (1.7 eV) diminished and the intensity of symmetry forbidden transition (2.1 eV) increased. We proposed that this effect is due to the presence of longer Mn-O apical bond length in $LaGa_{1-x}Mn_xGe_2O_7$ (x = 0.1, 0.2, 0.3 and 0.4).

3.5 References

1. D. S. Gouveia, L. E. B. Soledade, C. A. Paskocimas, E. Longo, A. G. Souza, I. M. G. Santos, Mater. Res. Bull. 41 (2006) 2049.
2. V. Pishch, T. I. Rotman, Z. A. Romanenko, V. A. Goremykin, Glass Ceram. 46 (1989) 113.
3. R. M. Christie, Color Theory, Royal Society of Chemistry, Cambridge, United Kingdom (2001).
4. A. E. Smith, H. Mizoguchi, K. Delaney, N. A. Spaldin, A. W. Sleight, M. A. Subramanian, J. Am Chem. Soc. 131 (2009) 17084.
5. H. Mizoguchi, A. W. Sleight, M. A. Subramanian, Inorg. Chem. 50 (2011) 10.
6. T.-G. Kim, S.-J. Kim, C. C. Lin, R.-S. Liu, T.-S. Chan, S.-J. Im, J. Mater. Chem. C. 1 (2013) 5843.
7. S. Tamilarasan, D. Sarma, M. L. P. Reddy, S. Natarajan, J. Gopalakrishnan, RSC Adv. 3 (2013) 3199.
8. B. Fromme, D-D Excitations in Transition-Metal Oxides, Springer-Verlag, Berlin, Heidelberg (2001).
9. R. G. Burns, Mineralogical Applications of Crystal Field Theory, Cambridge University Press, Cambridge, United Kingdom (1993).
10. A. A. Kaminskii, B. V. Mill, A. V. Butashin, E. L. Belokoneva and K. Kurbanov, phys. Status Solidi A. 103 (1987) 575.
11. A. A. Kaminskii, H. Rhee, O. Lux, A. Kaltenbach, H. J. Eichler, J. Hanuza, S. N. Bagayev, H. Yoneda, A. Shirakawa, K. Ueda, Laser Phys. Lett. 10 (2013) 075803.
12. Y. C. Li, Y. H. Chang, Y. F. Lin, Y. S. Chang, Y. J. Lin, Electrochem. Solid State Lett. 9 (2006) H74.
13. Y. C. Li, Y. H. Chang, Y. F. Lin, Y. J. Lin, Y. S. Chang, Appl. Phys. Lett. 89 (2006) 081110.
14. M. Nespolo, M. Isobe, J. Iida, N. Kimizuka, Acta Crystallogr. Sect. B: Struct. Sci. 56 (2000) 805.
15. M. Kasunic, S. D. Skapin, D. Suvorov, A. Golobic, Acta Chim. Slov. 59 (2012) 117.
16. D.-Y. Cho, S. J. Oh, D. G. Kim, A. Tanaka, J. H. Park, Phys. Rev. B: Condens. Matter Mater. Phys. 79 (2009) 035116.
17. Z. Jin, H. Ma, G. Li, Y. Xu, G. Ma, Z. Cheng, Appl. Phys. Lett. 100 (2012) 021106.

18. G. J. Babonas, J. C. Grivel, A. Reza, R. Girkantaite, Lith. J. Phys. 47 (2007) 309.
19. F. M. F. de Groot, M. Grioni, J. C. Fuggle, J. Ghijsen, G. A. Sawatzky, H. Petersen, Phys. Rev. B: Condens. Matter Mater. Phys. 40 (1989) 5715.
20. M. C. Nolet, A. Michaud, C. Bain, D. Zargarian, C. Reber, Photochem. Photobiol. 82 (2006) 57.

4

INFLUENCE OF ALIOVALENT CATION SUBSTITUTIONS ON THE OPTICAL PROPERTIES OF $In_2Cu_2O_5$ SYSTEM

The influence of aliovalent cation substitutions on the optical properties of the $In_2Cu_2O_5$ *system has been investigated through the powder X-ray diffraction coupled with Rietveld analysis, UV-vis-NIR spectroscopy, scanning electron microscope attached with the energy dispersive spectrometer. The aliovalent cation substitution affected the optical absorption of the system distinctly as the counter cation substitution of* Sc^{3+} *influences the crystal field environment of* Cu^{2+} *ions more dominantly than that of the direct substitution of* Zn^{2+} *ions. Consequently, this allowed the red shift of the absorption edge pronounced in the case of* Sc^{3+} *substituted samples than that in the* Zn^{2+} *substituted ones. The key factor responsible for achieving the larger red shift in* Sc^{3+} *substituted sample is due to increased anion polarizability. The modified absorption properties translated in enhancing the green chromaticity and reflectance of the* $In_2Cu_2O_5$ *system even better than the commercially available chromium oxide green* (Cr_2O_3)*.*

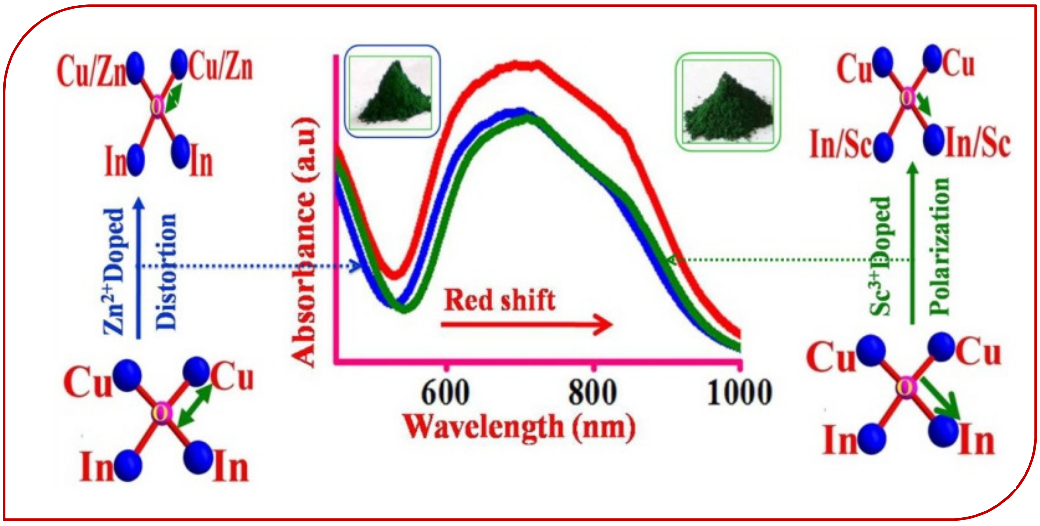

4.1 Introduction

Inorganic compounds display a wide range of colors because of their tendency to absorb energies within the visible range of the light spectrum [1]. Transition metal ions tend to form colored compounds and the attribution of color mainly depends on the local crystal field. However, most inorganic compounds contain transition metals, V, Cr, Mn, Fe, Co, Ni, and Cu these are the generally used coloring constituents [2]. Among these transition elements, our interest focuses on the coloring capability of copper. Copper commonly produces green or blue color pigments by the incorporation of Cu^{2+} ion in the square planar or square pyramidal site. Coloring performance of an ion very much depends on its coordination environment. The green color of Y_2BaCuO_5 is due to square pyramidal coordination (CuO_5) of Cu^{2+} ion [3] and the blue color in $BaCuSi_4O_{10}$ is due to the square planar coordination of copper (CuO_4) [4]. Color can be tuned by changing the CF splitting through changing the metal or ligand. Many ions can occur in more than one type of coordination and various colors are produced. As with the mineral malachite ($Cu_2CO_3(OH)_2$) and azurite $Cu_3(CO_3)_2(OH)_2$), chemical formula of these two minerals are same, but they possess different colors. The crystal field in azurite is sufficiently different from that of malachite that is why they perceive different colors blue versus green [5].

Crystal field splitting is strongly related to the structural features and the nature of chemical bonds between the metal and ligands, such as the covalent or ionic. In the historical blue pigments Egyptian Blue ($CaCuSi_4O_{10}$) and Han Blue ($BaCuSi_4O_{10}$), the slightest difference in the color tonality can be explained by the reduction in the Cu–O distance [6]. For a given ligand, the crystal field depends on the ionic radius (r) of the cation, biggest 'r' decreases the overlap between the cation and anion orbitals [7]. The heavier alkaline earth ion (M) increases M–O bond length and subsequently reduces the Cu–O bond. The Cu–O bond length is 1.929 Å and 1.921 Å for $CaCuSi_4O_{10}$ and $BaCuSi_4O_{10}$ respectively [8]. This situation is similarly found in Ba^{2+} doped $CaCuSi_4O_{10}$ phosphors, here the larger ionic radius of Ba^{2+} increased the Ca/Ba–O bond length and shortened the Cu–O bond length [9]. This will result in the red shift of the emission spectrum of $CaCuSi_4O_{10}$ phosphor. In the case of Eu^{2+} doped MGa_2S_4 (Ca, Sr and Ba) phosphors, the lower red shift is observed in the $BaGa_2S_4$ due to lower crystal field splitting [10]. Here the electronegativity plays an important rule.

Covalency also affects the electronic transitions in the absorption spectrum. Increasing of covalency shifts the electronic transitions to lower energy side of the absorption spectrum [11]. For a given dopant ion its absorption spectrum is not only dependent on its energy level but also significantly affected by the host lattice.

Inorganic pigments have been utilized by mankind since ancient times, and are widely applied to plastics, paints and inks [12]. In the present work, we studied the pigmentary properties and changes observed in the absorption spectrum by the doping of ions in the $In_2Cu_2O_5$ system. Mainly we focused on the doping effect of Zn^{2+} and Sc^{3+} in the host matrix. It is observed that these doped divalent and trivalent ions significantly affect the absorption spectrum. $In_2Cu_2O_5$ is a green colored pigment with orthorhombic structure [13]. Coordination geometry around the copper ion is a square planar one, this is the color producing constituent in $In_2Cu_2O_5$. In the present work we synthesized $In_2Cu_{2-x}Zn_xO_5$ and $In_{2-x}Sc_xCu_2O_5$ (x = 0, 0.05, 0.1 and 0.15) by the solid state method. Both the Zn^{2+} and Sc^{3+} affect the crystal field around the Cu^{2+} ion in the host matrix, this leads to the changes in the absorption bands of the Cu^{2+} ion. The modified green pigments possess greater green chromaticity and reflectance than that of commercially available chromium oxide green (Cr_2O_3).

4.2 Experimental Section

4.2.1 *Materials and Synthesis*

The $In_2Cu_{2-x}Zn_xO_5$ and $In_{2-x}Sc_xCu_2O_5$ (x = 0, 0.05, 0.1 and 0.15) pigments were prepared by the solid state method. The precursors used for this purpose are In_2O_3, Sc_2O_3, ZnO, and CuO (99.9% supplied by Sigma-Aldrich,). Stoichiometric amounts of the weighed samples were mixed thoroughly in an agate mortar using acetone as the mixing medium. Mixed product was dried in an oven at 100°C for 30 min. The process of mixing and drying was repeated thrice to get a homogeneous mixture. Finally, the dried mixtures were placed in platinum crucibles and calcined in an electric furnace at 1050°C for 6 h, using a heating rate of 5°C/min. The calcined samples were ground thoroughly into fine powders in an agate mortar for further studies.

4.2.2 *Characterization*

Formation of single phase product and their structure were studied by using powder X-ray diffraction. The PXRD pattern was taken with the aid of the PANalytical

X’Pert Pro diffractometer (Ni-filtered Cu Kα radiation, λ = 1.5406 Å). The structural parameters of the samples are refined by the Rietveld method using the X’Pert HighScore Plus software. The data were recorded over the 2θ range of 10-90°. By using scanning electron microscopy (JEOL JSM-5600 LV SEM) and energy dispersive spectrometer (EDS), we examined the morphology and elemental analysis of the prepared samples. The thermal stability of the colorant was also checked using a (Schimadzu, DTG-60) make in an argon atmosphere at a heating rate of 20°C/min. For characterization of absorption of the samples (the color parameters), the diffuse reflectance spectra were recorded (220-2500 nm) employing a (Shimadzu UV-3600) UV-vis spectrometer using PTFE as the reference. The band gap values were calculated using the Kubelka-Munk function which is given by $f(R) = (1-R)^2/2R$, where R is the reflectance value. A plot of $f(R)$ against wavelength is drawn, and the absorption edge is determined from the plot. The CIE 1976 $L^*a^*b^*$ colorimetric method was used, as recommended by the Commission Internationale de l’Eclairage (CIE). In this method, L^* is the lightness axis [black (0) to white (100)], a^* is the green (−ve) to red (+ve) axis, and b^* is the blue (−ve) to yellow (+ve) axis. The parameter, C^* (chroma) represents saturation of the color and is defined as $C^* = [(a^*)^2 + (b^*)^2]^{1/2}$ and $h°$ represents the hue angle. The hue angle, $h°$ is expressed in degrees and ranges from 0 to 360° and is calculated by using the formula $h° = \tan^{-1}(b^*/a^*)$.

4.3 Results and Discussion

4.3.1 *Structural Analysis of $In_{2-x}Sc_xCu_2O_5$ and $In_2Cu_{2-x}Zn_xO_5$ Systems*

4.3.1.1 *$In_{2-x}Sc_xCu_2O_5$ (x = 0, 0.05, 0.1 and 0.15)*

Crystal structure of $In_2Cu_2O_5$ contains indium polyhedra and Cu planes [13]. Here the two indium atoms are lying at the centers of the distorted octahedron and the polyhedra of Cu^{2+} gives the impression of five coordination [14]. Interatomic distances of Cu–O bonds are varying from 1.815 Å - 2.529 Å and from 1.830 Å - 2.594 Å for Cu_1–O and Cu_2–O bonds respectively. The length of four Cu–O bonds in the plane are quite small (1.815 - 2.010 Å) compared to the distance of the fifth Cu ion which is significantly larger (2.529 - 2.594 Å). So the coordination geometry around the Cu^{2+} can be considered as distorted square planar. It consists of CuO_4 units, which combine to another by producing a dimer, where each Cu ion is connected together with oxygen situated between the Cu ions [15]. In this structure, each of the copper and indium ions is connected together by common oxygen edges. Figure 4.1 display the structural representation of $In_2Cu_2O_5$, which modeled using the diamond crystal and molecular structure visualization software based on the atomic coordinate data from XRD refinement.

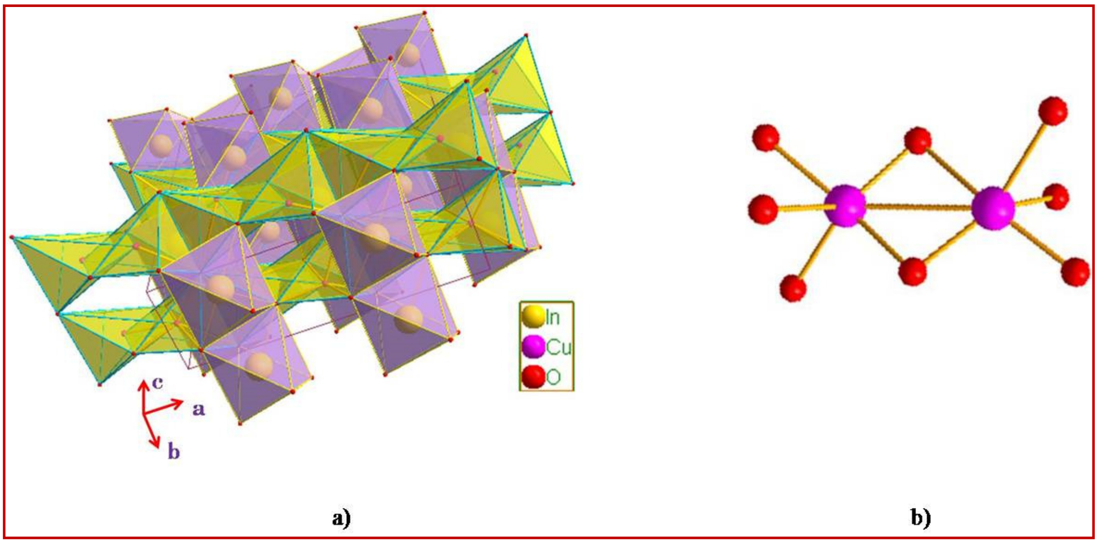

Figure 4.1 (a) Schematic crystal structure illustration of $In_2Cu_2O_5$ and (b) Cu–Odimers connected by oxygen**.**

Crystal structure of $In_2Cu_2O_5$ is isostructural to $Ho_2Cu_2O_5$. This crystallizes in an orthorhombic structure with a space group of $Pna2_1$ [13]. From the X-ray diffraction profiles of $In_{2-x}Sc_xCu_2O_5$ (x = 0, 0.05, 0.1 and 0.15) all the peaks in the diffraction patterns were matched well with the reflections in the space group $Pna2_1$ (Figure 4.2). A single-phase orthorhombic structure was observed in all samples, all patterns are compared with the standard reference card 01-070-1082. The diffraction peaks shifted towards higher angle side, this is because the ionic radius of Sc^{3+} (0.745 Å) is smaller than that of In^{3+} (0.80 Å) in the host lattice [16]. Lattice constants of $In_{2-x}Sc_xCu_2O_5$ (x = 0, 0.05, 0.1 and 0.15) are summarized in table 4.1. Variations in the lattice parameters indicate that Sc^{3+} ions are effectively incorporated into the host lattice. In the undoped sample, we can see the presence of some impurity phase of ($^*In_2O_3$). With a starting model adopted by reference [14], we performed Rietveld refinement of XRD data of $In_{2-x}Sc_xCu_2O_5$ (x = 0, 0.05, 0.1 and.0.15). Refinements were done with the aid of X'Pert HighScore Plus software. Selected Cu–O bond distances and refined parameters of $In_{2-x}Sc_xCu_2O_5$ (x = 0, 0.05, 0.1 and 0.15*)* were given in the table 4.2.

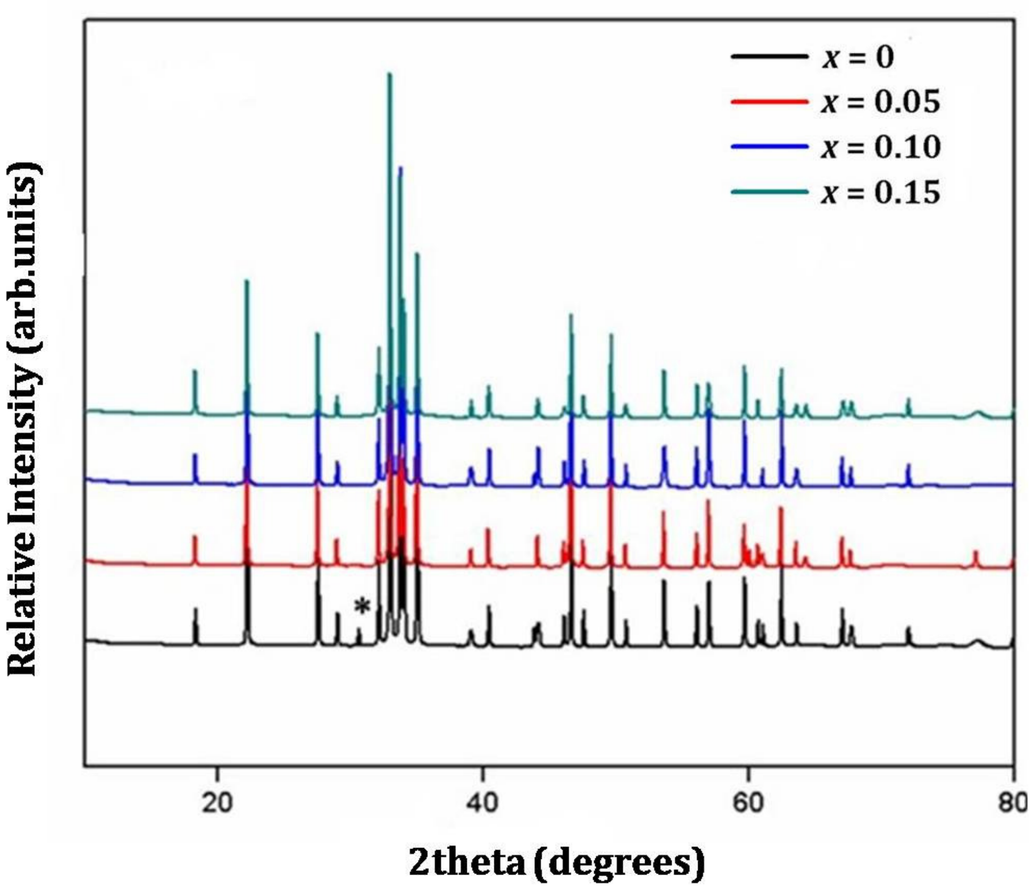

Figure 4.2 Powder XRD patterns of $In_{2-x}Sc_xCu_2O_5$ (x = 0, 0.05, 0.1 and 0.15).

Table 4.1 Lattice constants of $In_{2-x}Sc_xCu_2O_5$ (x = 0, 0.05, 0.1 and 0.15).

Sample	***a* (Å)**	***b* (Å)**	***c* (Å)**	***V* (Å³)**
x = 0	10.5483(3)	3.2820(1)	12.3063(3)	426.0540
x = 0.05	10.5441(5)	3.2796(1)	12.3187(6)	426.0000
x = 0.10	10.5470(5)	3.2818(0)	12.3041(5)	425.8936
x = 0.15	10.5448(4)	3.2790(1)	12.3145(5)	425.7962

Table 4.2 Selected Cu–Obond distances and refined parameters of $In_{2-x}Sc_xCu_2O_5$ (x = 0, 0.05, 0.1 and 0.15).

Bond length (Å)	***x* = 0**	***x* = 0.05**	***x* = 0.10**	***x* = 0.15**
Cu_1 - O2	1.815(4)	1.794 (4)	1.709(4)	1.743(8)
- O4	1.907(6)	1.954(4)	1.889 (4)	1.894(5)
- O3	2.010(2)	1.955(3)	1.913(5)	1.979(1)
- O5	2.000(1)	1.964(6)	2.021(3)	2.015(2)
- O3	2.529(2)	2.503(2)	2.405 (3)	2.565(4)
Cu_2 -O4	1.830(4)	1.852(5)	1.810(1)	1.831(9)
- O1	1.845(1)	1.848(3)	1.900(3)	1.916(2)
- O2	2.022(7)	2.108(4)	2.091(6)	1.943(2)
- O3	2.009(3)	2.050(5)	2.221(4)	2.032 (3)
- O3	2.594(2)	2.649 (3)	2.703(7)	2.592(5)
R_{exp}[%]	9.52	9.79	9.44	9.58
R_p[%]	11.28	11.01	10.89	10.24
R_{wp}[%]	15.14	14.76	14.10	13.44
GOF	2.52	2.27	2.26	1.96

4.3.1.2 $In_2Cu_{2-x}Zn_xO_5$ (x = 0, 0.05, 0.1 and 0.15)

$In_2Cu_{2-x}Zn_xO_5$ (x = 0, 0.05, 0.1 and 0.15) also crystallizes in orthorhombic structure with a Pna21 space group (Figure 4.3). In the powder diffraction patterns of Zn^{2+} doped samples, diffraction peaks shifted towards the lower angle side as Zn^{2+} (0.74 Å) is larger than that of Cu^{2+} (0.71 Å) in the host lattice [16]. A small amount of impurity phase (*In_2O_3) appeared in the x = 0 and 0.05 doping concentrations of Zn^{2+}. Lattice constants of $In_2Cu_{2-x}Zn_xO_5$ (x = 0, 0.05, 0.1 and 0.15) are summarized in table 4.3. From this table, it can be observed that lattice volume increases with increasing the concentration of Zn^{2+}. We performed Rietveld refinement of $In_2Cu_{2-x}Zn_xO_5$ (x = 0, 0.05, 0.1 and 0.15) to illustrate in which site of Cu^{2+}occupied by Zn^{2+}. Best fit with lowest R values was obtained by the occupation of Zn^{2+} in the Cu2 site.

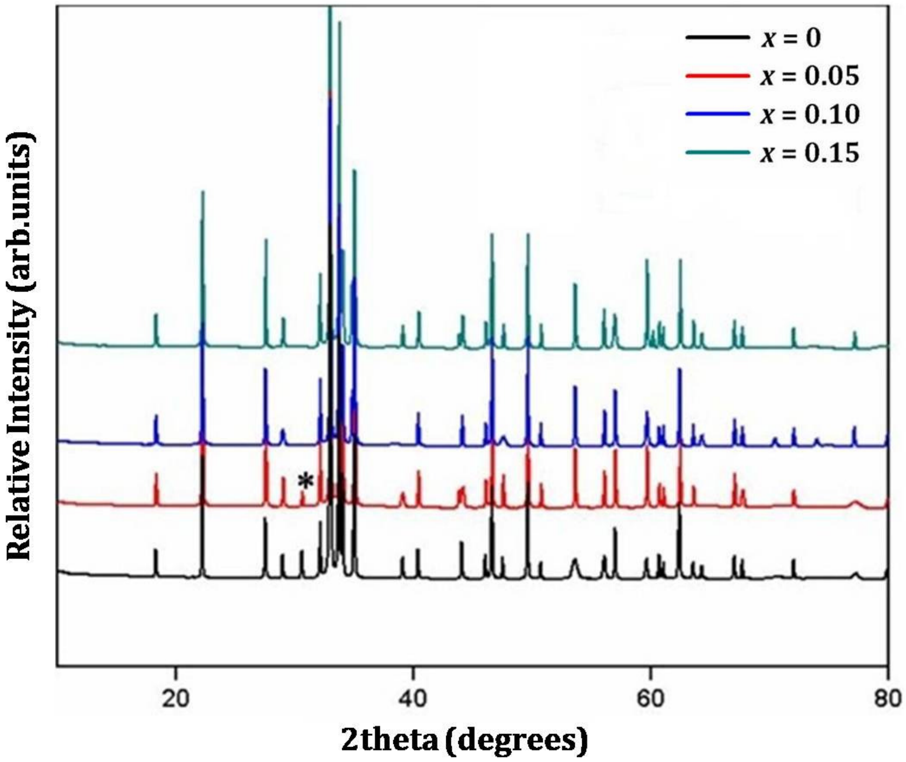

Figure 4.3 Powder XRD patterns of $In_2Cu_{2-x}Zn_xO_5$ (x = 0, 0.05, 0.1 and 0.15).

Crystal structure of $In_2Cu_{1.9}Zn_{0.1}O_5$ was refined based on the experimental powder diffraction data by Rietveld analysis (Table 4.4 and Figure 4.4). Selected Cu–Obond distances, the obtained goodness of fit and R values of $In_2Cu_{2-x}Zn_xO_5$ (x = 0, 0.05, 0.1 and 0.15) are given in table 4.5. The Cu1–O bond length slightly decreases and the Cu2–O bond length increases, the average bond length changes with increasing the doping concentration.

Table 4.3 Lattice parameters of $In_2Cu_{2-x}Zn_xO_5$ (x = 0, 0.05, 0.1 and 0.15).

Sample	a (Å)	b (Å)	c (Å)	V (Å^3)
x = 0	10.5483(3)	3.2820(1)	12.3063(3)	426.0540
x = 0.05	10.5469(3)	3.2810(0)	12.3138(4)	426.1158
x = 0.10	10.5453(3)	3.2798(0)	12.3214(4)	426.1558
x = 0.15	10.5434(3)	3.2791(0)	12.3271(4)	426.1918

Table 4.4 Atomic parameters of $In_2Cu_{1.9}Zn_{0.1}O_5$ from Rietveld refinement.

Atom	Site	x	y	z	occupancy
In1	4a	0.2106(5)	0.2362(4)	0	1
In2	4a	0.0346(6)	0.2264(3)	0.3329(5)	1
Cu1	4a	0.9900(1)	0.6881(4)	0.1141(1)	1
Cu2	4a	0.2610(1)	0.6753(3)	0.2198(2)	0.90
Zn2	4a	0.2610(1)	0.6753(3)	0.2198(2)	0.10
O1	4a	0.1732(6)	0.7309(3)	0.3510(5)	1
O2	4a	0.3265(4)	0.7236(4)	0.0696(1)	1
O3	4a	0.1052(6)	0.2930(0)	0.1487(3)	1
O4	4a	0.4311(5)	0.7731(3)	0.2582(9)	1
O5	4a	0.4241(2)	0.2099(6)	0.4730(4)	1

Table 4.5 Selected Cu–Obond distances and refined parameters of $In_2Cu_{2-x}Zn_xO_5$ (x = 0, 0.05, 0.1 and 0.15).

Bond length (Å)	**x = 0**	**x = 0.05**	**x = 0.10**	**x = 0.15**
Cu_1 - O2	1.815(4)	1.770(3)	1.800(4)	1.743(5)
- O4	1.907(6)	1.918(5)	1.935(4)	1.934(3)
- O3	2.010(2)	1.983(6)	1.948(3)	2.004(2)
- O5	2.000(1)	1.962(5)	1.978(2)	1.956(4)
- O3	2.529(2)	2.519(8)	2.463(4)	2.531(2)
Cu_2 - O4	1.830(4)	1.891(2)	1.912(1)	1.885(3)
- O1	1.845(1)	1.879(4)	1.917(4)	1.928(2)
- O2	2.022(7)	2.091(3)	2.018(2)	1.953(2)
- O3	2.009(3)	2.023(1)	2.094(3)	2.107(3)
- O3	2.594(2)	2.632(2)	2.674(4)	2.584(2)
R_{exp}[%]	9.52	9.66	9.88	10.04
R_p[%]	11.28	10.87	10.27	10.55
R_{wp}[%]	15.14	14.39	13.08	13.65
GOF	2.52	2.17	1.96	1.85

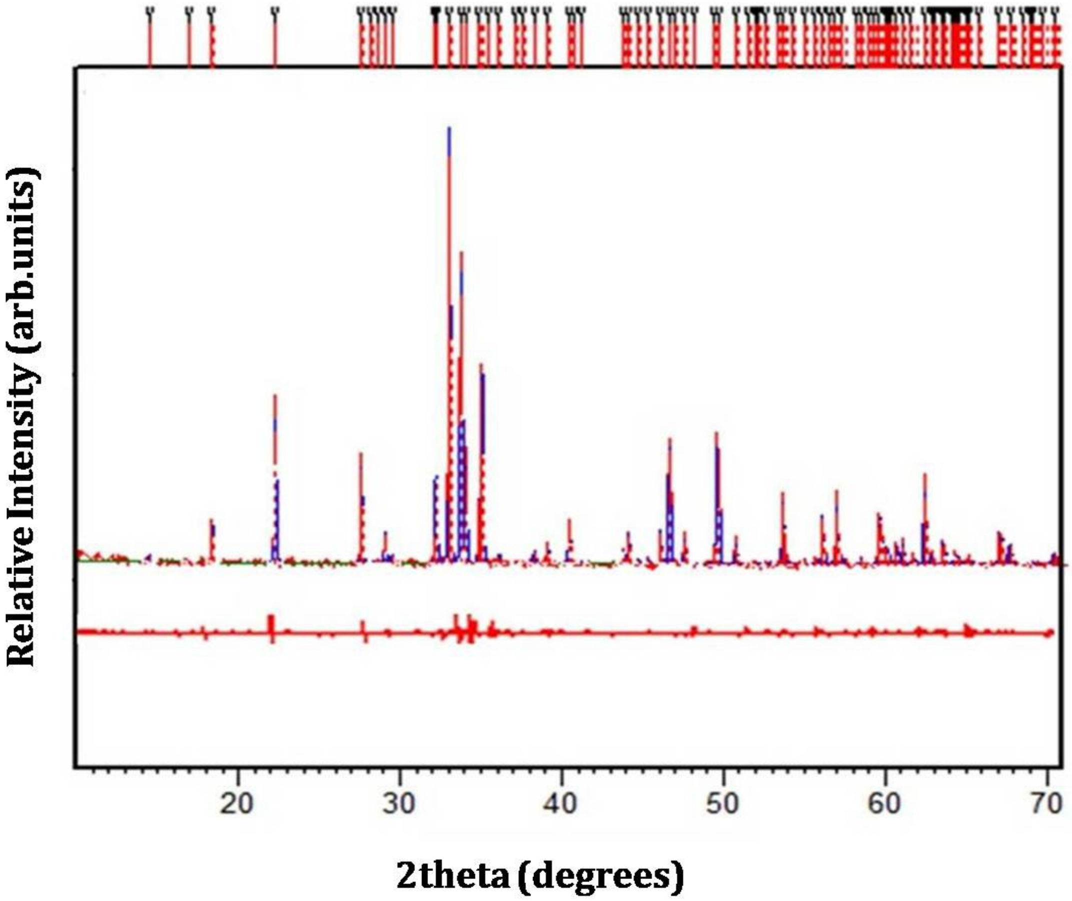

Figure 4.4 Rietveld refinement of the structure of $In_2Cu_{1.9}Zn_{0.1}O_5$. The observed (red solid line), calculated (blue dotted) and difference (at the bottom).

4.3.2 *Optical Studies of $In_{2-x}Sc_xCu_2O_5$ and $In_2Cu_{2-x}Zn_xO_5$ Systems*

4.3.2.1 $In_{2-x}Sc_xCu_2O_5$ (x = 0, 0.05, 0.1 and 0.15)

Figure 4.5 shows the absorbance spectra of $In_{2-x}Sc_xCu_2O_5$ (x = 0, 0.05, 0.1 and 0.15) system. The observed spectra have two main bands, a broad optical absorption band appeared in the 550 - 860 nm region and a strong absorption band located in the high energy region (300 - 450 nm). These are the characteristic absorption bands of Cu^{2+} ion in four coordination and this indicates its square planar geometry. The high energy band in the region of 400 nm is attributed to the ligand to metal charge transfer transition from the O^{2-} to Cu^{2+} [17]. The latter band is attributed to a d-d transition of Cu^{2+} in the square planar field.

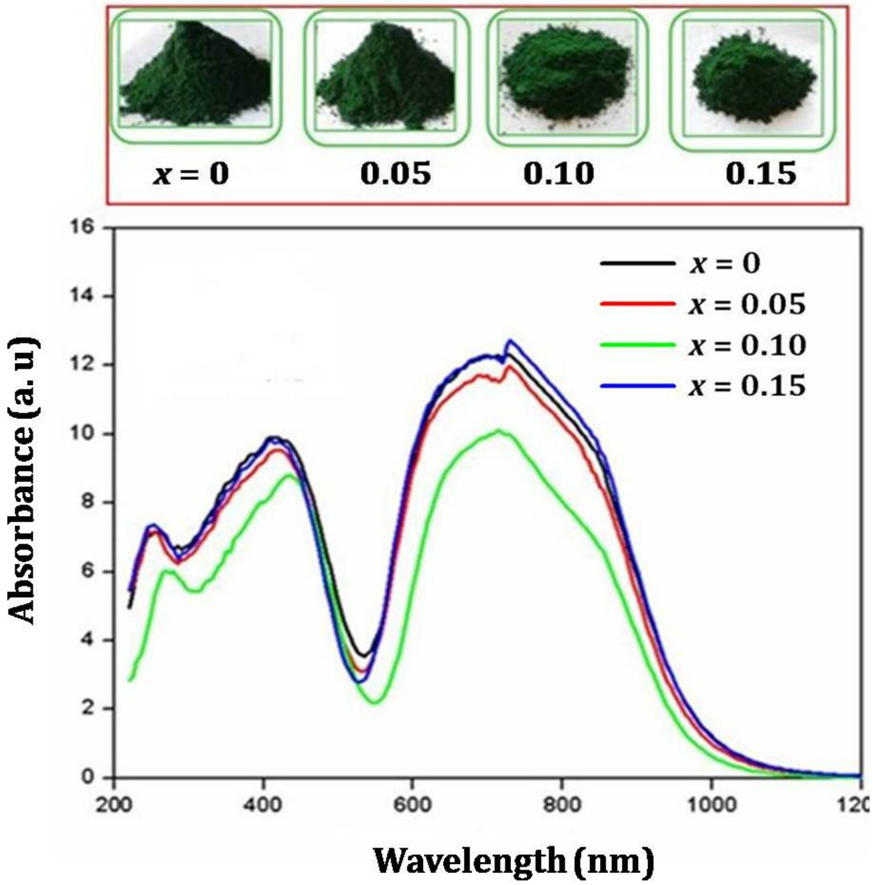

Figure 4.5 Absorbance spectra of $In_{2-x}Sc_xCu_2O_5$ ($x = 0, 0.05, 0.1$ and 0.15)

Square planar coordination can be treated as the limiting case of Jahn-Teller distortion of an octahedral shown in figure 4.6. Cu^{2+} possess d^9 electronic configuration and nearly always found in a distorted ligand environment. In the octahedral site, its high energy e_g orbitals contain three electrons and lower energy t_{2g} orbits are doubly degenerate. In such compounds the e_g orbitals involved in the degeneracy point directly at the ligands so distortion can result in a large energetic stabilization [18]. Jahn-Teller distortion leads to tetragonal distortion of the octahedron, with the extreme of tetragonal distortion being the complete loss of axial ligands and formation of a square planar complex [19]. In square planar complexes the d-orbitals split into four different levels, and the relative energy positions are $d_{x^2-y^2}$ (b_{1g})>d_{xy} (b_{2g})> d_{z^2} (a_{1g})>d_{xz}, d_{yz} (e_g).

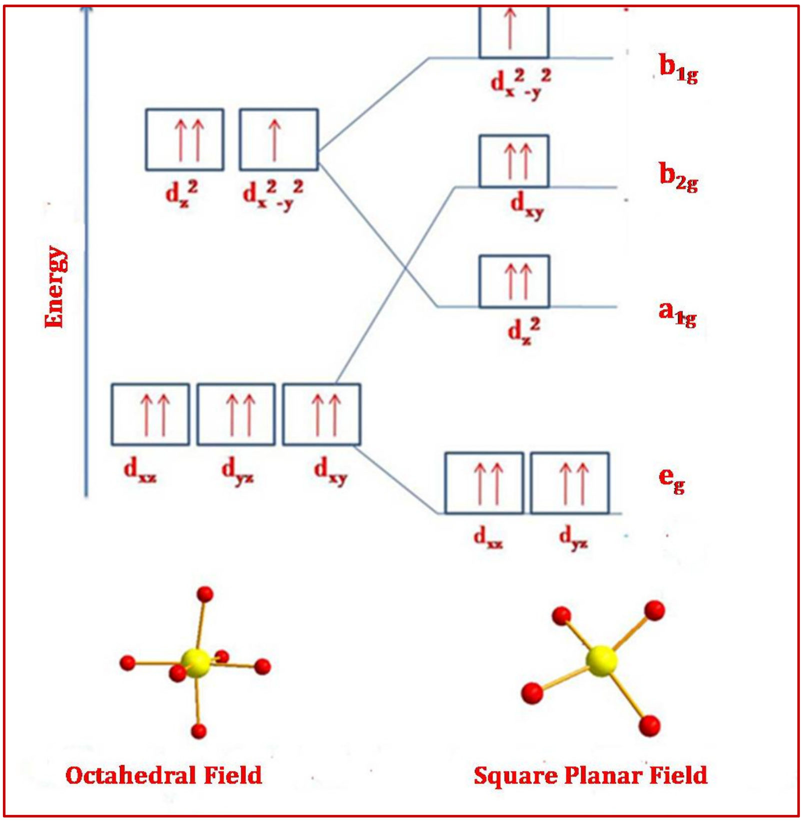

Figure 4.6 Crystal field splitting of Cu^{2+} in octahedral and square planar field.

The broadening of this band around 550-860 nm can be recognized due to the superposition of two electronic transitions in d-orbitals corresponding to $^2B_{1g} \rightarrow {}^2E_g$ (~ 658 - 677 nm) and $^2B_{1g} \rightarrow {}^2B_{2g}$ (~ 791 - 799 nm) transitions [20]. Both of the charge transfer and d-d transition bands shifted to longer wavelength (red shift) with the increasing of Sc^{3+} content.

Our main interest lies in the lowest energy transition, a relatively much stronger and broad band appearing in the visible region. The absorption edge of undoped samples was estimated to be ~ 550 nm and the broad peak shifted towards higher wavelength with increasing the concentration of Sc^{3+} ion up to 10 mol%. Several factors affect the red shift in the absorption spectrum, such as the bond lengths from the metal ion to the coordinating anions, the molecular orbital overlap or degree of covalency between the metal ion and ligands, coordination environment, and bond polarizability [21].To explain this phenomenon, the possible reason is proposed as follows. It is well known that anion polarizability depends on the nature of cation with which they bond [22]. From the electronegativity point of view, the increase in the cation polarizability means decreased ability of an ion to attract electrons from the atoms bonded to it. Since the electronegativity of Sc^{3+} (1.3) is lower than that of In^{3+} (1.7) [23] which increases the polarizability of the anion. Therefore, the Sc^{3+} ions are less able to attract the O^{2-} electron density towards them. As a result of this O^{2-} in the doped samples are more polarizable than that of the O^{2-} in the undoped sample [24]. Although the In^{3+}/Sc^{3+} and Cu^{2+} are sitting in different coordination spheres, the shift of the center of negative charge density around the Cu^{2+} ion will be increasing through inductive effect because they are adjacent to the coordination sphere of Cu^{2+} and thus influence it. As a result of this the distance between the Cu^{2+} and the center of negative charge density decreases. With increasing Sc^{3+}concentration, the absorption becomes stronger, and the absorption edge shifts to the longer wavelength due to the decrease in the Cu–O bond length. From the Rietveld refinement of $In_{2-x}Sc_xCu_2O_5$ (x = 0, 0.05, 0.1 and 0.15) the average Cu_1–O distance is shorter than that of Cu_2–O (Figure 4.7). The average Cu_1–O distance decreases with increasing the concentration of Sc^{3+} up to 10 mol%. Accordingly, the crystal field splitting of the Cu_1 site is larger than that of the Cu_2 site. Thus, we expected that the red shift in the absorption spectrum is due to the crystal field splitting produced by the first copper atom, than that of the second one.

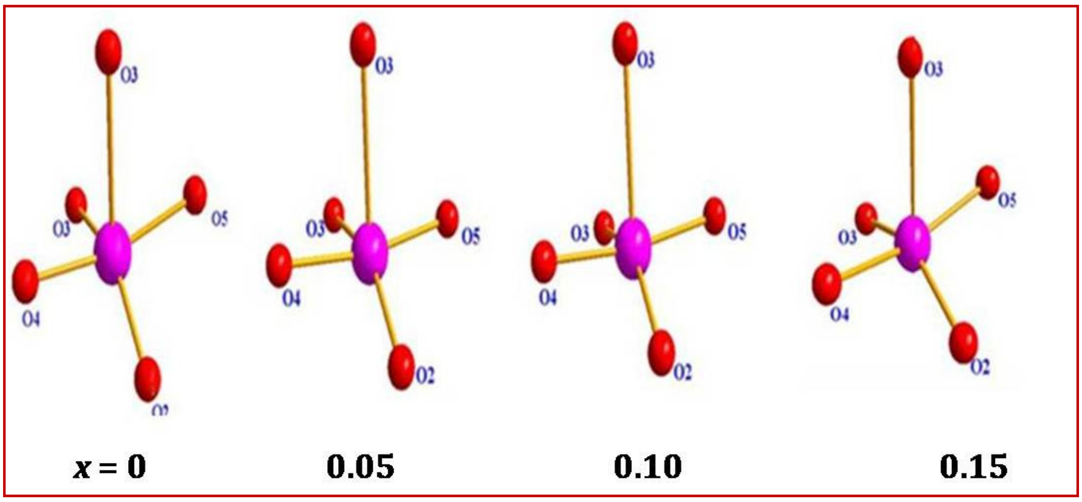

Figure 4.7 Schematic representation of Cu_1 site in $In_{2-x}Sc_xCu_2O_5$ (x = 0, 0.05, 0.1 and 0.15).

There is a red shift in the charge transfer peak also; CT peaks are sensitive to changes in the metal-ligand distances [25]. An increase of the metal-ligand distance tends to increase the energy of CT peaks. Here the metal-ligand distances decrease with increasing the concentration of Sc^{3+}. This is consistent with the red shift of the absorption edge of the charge transfer peak from 300 - 350 nm. Thus, it is expected that the lattice shrink-induced larger crystal field splitting should be the dominant factor in the red shift of CT band. Due to inductive effect, the electron density of the O^{2-} ion increases. This situation favors electron transfer from ligand to metal.

Absorption spectra provide direct information on the relationship between the site distortion and d orbital splitting, particularly in the transition metal bearing compounds. Equations 4.1- 4.4 given the energy levels of the Cu^{2+} ion in tetragonally distorted symmetry [26],

$$^2B_{1g} \rightarrow -6Dq - 2Ds + Dt \tag{4.1}$$

$$^2A_{1g} \rightarrow -6Dq + 2Ds + 6Dt \tag{4.2}$$

$$^2B_{2g} \rightarrow 4Dq - 2Ds + Dt \tag{4.3}$$

$$^2E_g \rightarrow 4Dq + \mathrm{Ds} - 4Dt \tag{4.4}$$

In square field, distortion increases with $^2A_{1g}$ as the highest and $^2B_{1g}$ as the lowest energy levels. E_1 and E_2 are the energy separations between the excited $^2B_{2g}$ and ^2E_g and the ground $^2B_{1g}$ states given in the below equations 4.5 & 4.6.

$$E_1 = 10Dq \tag{4.5}$$

$$E_2 = 10Dq - 3\,Ds + 5Dt \tag{4.6}$$

Here Dq is the cubic field parameter, and Ds and Dt are the tetragonal field parameters. The tetragonal field parameters are calculated using the equations 4.7 and 4.8 from the local geometrical relationship of the studied impurity centers using the superposition model, which has been extensively adopted for transition-metal ions in the compounds [27].

$$D_s = (4/7)\,\bar{A}_2(R)\,[R/R_{\parallel})^{t_2} - (R/R_{\perp})^{t_2}] \tag{4.7}$$

$$D_t = (32/21)\,\bar{A}_4(R)\,[R/R_{\parallel})^{t_4} - (R/R_{\perp})^{t_4}] \tag{4.8}$$

$\bar{A}_2(R)$ and $\bar{A}_4(R)$ are the intrinsic parameters, with the reference bond length R taken as the average Cu^{2+}–O^{2-}distance. Here $t_2 \approx 3$ and $t_4 \approx 5$ are the power-law exponents. For octahedral $3d^n$ clusters, the relationships $\bar{A}_4(R) \approx (3/4)\ Dq$ [27] and $\bar{A}_2(R)/\bar{A}_4(R) \approx 8 - 12$, $\bar{A}_2(R) \approx 9\,\bar{A}_4(R)$ reasonably applied here. From the optical spectra for Cu^{2+}, the spectral parameters *Dq* can be calculated. With this model, we have estimated the peak positions of the crystal field bands.

The crystal field parameters *Ds* and *Dt* can be estimated from the bond distances. Both experimental and calculated energies using the crystal field parameters *Ds* and *Dt* are listed in table 4.6. In the absorption spectra of $In_{2-x}Sc_xCu_2O_5$ (x = 0, 0.05, 0.1 and 0.15) the observed transition energy of $^2B_{1g} \rightarrow {}^2E_g$ and $^2B_{1g} \rightarrow {}^2B_{2g}$ decreases up to 10 mol% of Sc^{3+}.

Table 4.6 Observed and calculated energies and assignments of the bands of $In_{2-x}Sc_xCu_2O_5$ (x =0, 0.05, 0.1 and 0.15) systems.

Sample	***T***	***Dq***	***Ds***	***Dt***	**Band position (cm^{-1})** $^2B_{1g} \rightarrow {}^2E_g$	
					observed	calculated
x = 0	0.76	1256	-3208	-1430	14998	14992
x = 0.05	0.77	1254	-3186	-1421	14966	14970
x = 0.10	0.78	1251	-2949	-1321	14757	14771
x = 0.15	0.74	1264	-3487	-1549	15197	15228

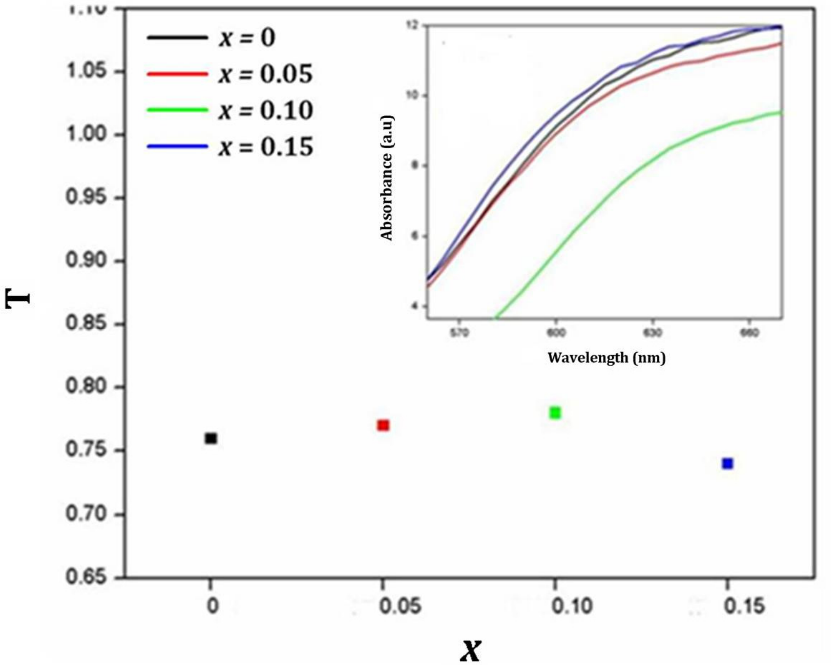

Figure 4.8 Influence of tetragonality factor on the red shift in the absorption spectrum of $In_{2-x}Sc_xCu_2O_5$ (x = 0, 0.05, 0.1 and 0.15).

As expected the low energy of this transition is caused by the comparative shortness of the bond along the z-axis [28]. Transition energies decrease as the tetragonality T increases, Here T is defined as the $\langle Cu–O\rangle_{eq}/\langle Cu–O\rangle_{ax}$, and hence T decreases with increasing elongation. $T = 1$ for a regular octahedral complex, while $T \approx 0.67$ represents an effectively planar complex. Influence of tetragonality factor on the red shift in the absorption spectra of $In_{2-x}Sc_xCu_2O_5$ (x = 0, 0.05, 0.1 and 0.15) is shown in figure 4.8.

4.3.2.2 $In_2Cu_{2-x}Zn_xO_5$ (x = 0, 0.05, 0.1 and 0.15)

The absorption spectra of $In_2Cu_{2-x}Zn_xO_5$ (x = 0, 0.05, 0.1 and 0.15) contain a charge transfer band located between 300- 400 nm and a d-d transition band of Cu^{2+} between 550 - 800 nm (Figure 4.9) [20]. Here the absorption edge of the $In_2Cu_{1.9}Zn_{0.1}O_5$ exhibits a remarkable red shift and all other concentrations exhibit a blue shift. From the Rietveld refinement data of $In_2Cu_{2-x}Zn_xO_5$ (x = 0, 0.05, 0.1 and 0.15) we found that substitution of Zn^{2+} by Cu^{2+} alters the individual Cu–Obond lengths slightly. There is a very pronounced change in bond length around the Cu2 site. This is seen as strong evidence that incorporation of Zn^{2+} almost exclusively takes place at the Cu2 site in the structure.

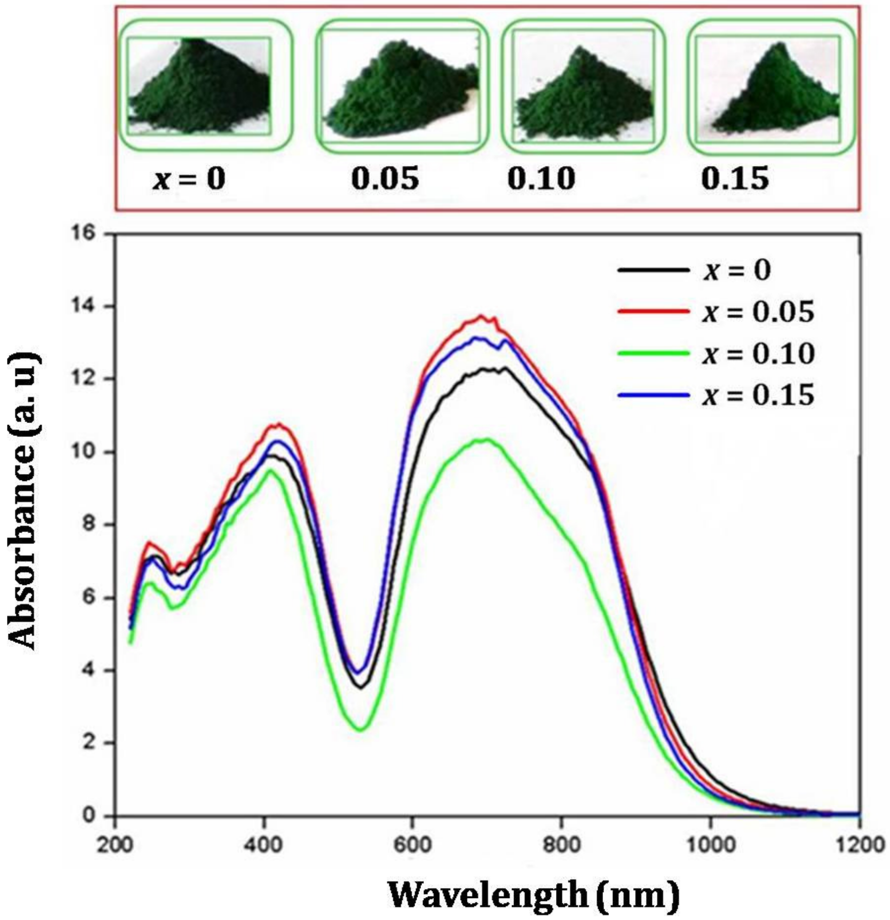

Figure 4.9 Absorbance spectra of $In_2Cu_{2-x}Zn_xO_5$ (x = 0, 0.05, 0.1 and 0.15).

The larger ionic radius of Zn^{2+} in the Cu_2 site lead to a stressful compression in the Cu_1site and this decrease the average Cu_1–O bond distances [29]. This stress is maximum in the case of 10 mol% doping concentration of Zn^{2+}. As a result of this, the average Cu_1–O bond length of $In_2Cu_{1.9}Zn_{0.1}O_5$ is smaller than that of other concentrations. This leads to the red shift in the absorption edge of $In_2Cu_{1.9}Zn_{0.1}O_5$. Weakening in the crystal field except for $In_2Cu_{1.9}Zn_{0.1}O_5$ could result in a blue shift for the transition of Cu^{2+}. From absorption spectrum of $In_2Cu_{2-x}Zn_xO_5$ (x = 0, 0.05, 0.1 and 0.15), it can be observed that introduction of Zn^{2+} ion distorts $In_2Cu_2O_5$ host lattice. The distortion of host lattice will have an impact on the absorption properties of Cu^{2+} ions.

Table 4.7 Observed and calculated energies and assignments of the bands $In_2Cu_{2-x}Zn_xO_5$ (*x* = 0, 0.05, 0.1 and 0.15) systems.

Sample	***T***	***Dq***	***Ds***	***Dt***	**Band position (cm^{-1})** $^2B_1g \rightarrow {}^2Eg$	
					observed	calculated
x = 0	0.76	1256	-3208	-1430	14992	14986
x = 0.05	0.75	1251	-3282	-1461	15037	15052
x = 0.10	0.77	1251	-3019	-1350	14814	14819
x = 0.15	0.75	1264	-3335	-1485	15093	15060

Tetragonality factor and the crystal field parameters *Ds* and *Dt* can be estimated from the bond distances. Both experimental and calculated energies using the crystal field parameters *Ds* and *Dt* are listed in table 4.7. Influence of tetragonality factor *T*, on the red shift in the absorption spectrum of $In_2Cu_{2-x}Zn_xO_5$ (*x* = 0, 0.05, 0.1 and 0.15) shown in figure 4.10.

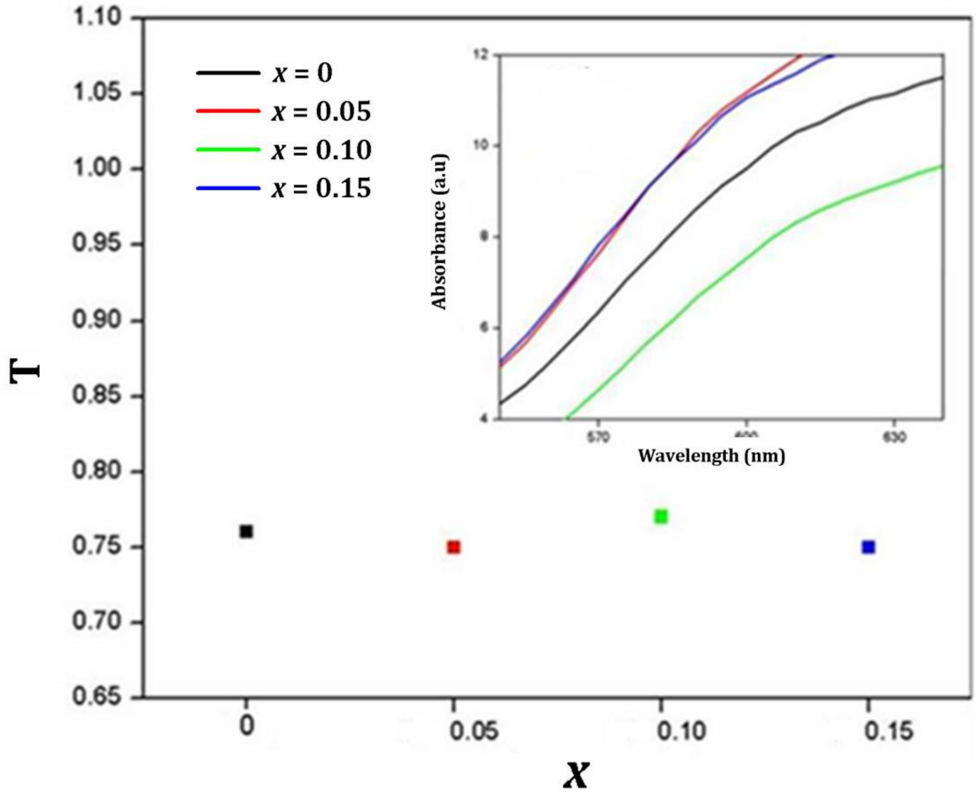

Figure 4.10 Influence of tetragonality factor (*T*), on the red shift in the absorption spectrum of $In_2Cu_{2-x}Zn_xO_5$ (x = 0, 0.05, 0.1 and 0.15).

4.3.3 *Comparison of Red Shift in $In_2Cu_{1.9}Zn_{0.1}O_5$ and $In_{1.9}Sc_{0.1}Cu_2O_5$*

In order to make a comprehensive analysis of the red shift of the absorption, with aliovalent cation substitutions, we select less electronegative Sc^{3+} ions to substitute for In^{3+} an ion that induces significant changes in the crystal field environment around the Cu^{2+} ion with the greater red shift (Figure 4.11). On the other hand, ions with larger ionic radius (Zn^{2+}) substitution for Cu^{2+} ions do not give a significant distortion around the crystal field environment of the Cu^{2+}. From the absorption spectra, we can observe that neighboring cations with smaller electronegativity gives more red shift than those with larger ionic radius. The findings in this work are important, which provide a chance to study the influence of anion polarizability and size effect in the red shift of the absorption spectrum Based on the above analysis; we proposed that anion polarizability enhancing the tetragonal field around Cu^{2+} in the $In_2Cu_2O_5$ system than that of the cation with larger ionic radius.

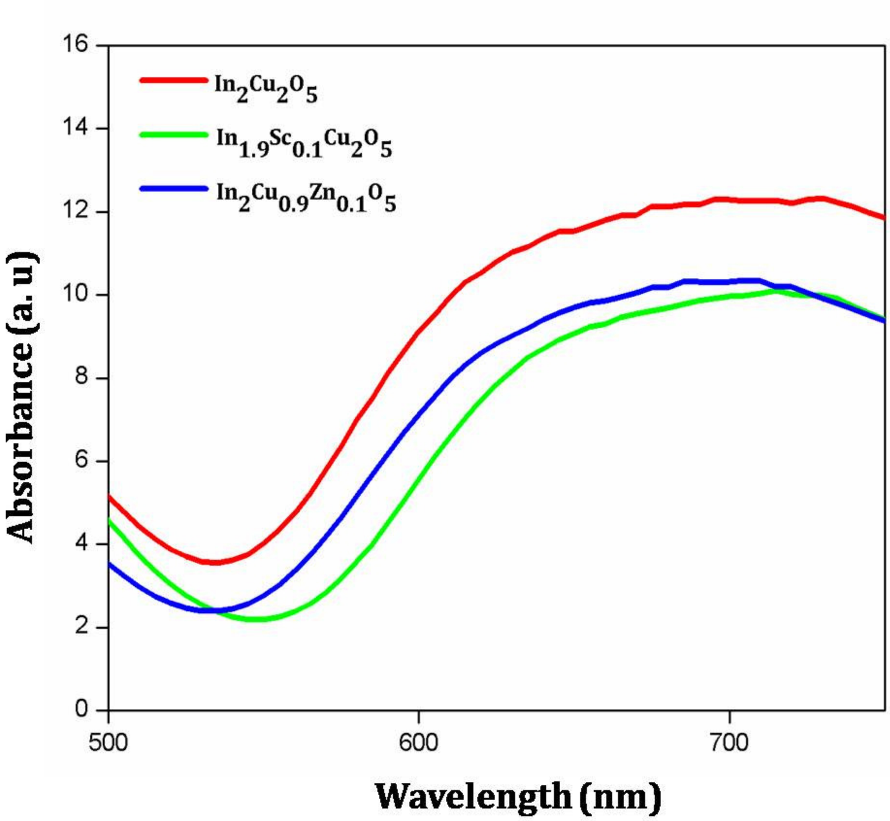

Figure 4.11 Comparison of absorption spectrum between $In_2Cu_{1.9}Zn_{0.1}O_5$ and $In_{1.9}Sc_{0.1}Cu_2O_5$.

4.3.4 *Enhanced Color and Near Infrared Reflectance*

Color properties of all synthesized $In_{2-x}Sc_xCu_2O_5$ and $In_2Cu_{2-x}Zn_xO_5$ (x = 0, 0.05, 0.1 and 0.15) pigments were shown in tables 4.8 and 4.9. Chromatic values are described in terms of $L^*a^*b^*$ coordinates. In $In_{2-x}Sc_xCu_2O_5$ the systematic doping of Sc^{3+} ranging from 0 to 0.10 mol % for In^{3+} results in an increase in the $-a^*$ value indicating an increasing green color. In $In_2Cu_{2-x}Zn_xO_5$, there is an optimum Zn^{2+} content to give the most vivid color. Among the samples both $In_2Cu_{1.9}Zn_{0.1}O_5$ and $In_{1.9}Sc_{0.1}Cu_2O_5$ had highest reflection intensity in the green region and strong absorption in the red region. Absorption of light from the red-orange region will give the green color to the compounds, which is the complementary color of red.

Table 4.8 *L*a*b** Color Coordinate data for $In_{2-x}Sc_xCu_2O_5$ (*x* = 0, 0.05, 0.1 and 0.15).

Sample	***L****	***a****	***b****	***C****	***h°***	**NIR Reflectance (%)**
x = 0	33.71	-17.71	10.42	20.55	149.53	49
x = 0.05	4.9	-20.13	11.01	22.95	151.33	54
x = 0.10	39.03	-25.16	13.17	28.4	152.38	68
x = 0.15	35.3	-23.32	11.38	25.95	153.99	51

Table 4.9 *L*a*b** Color Coordinate data for $In_2Cu_{2-x}Zn_xO_5$ (*x* = 0, 0.05, 0.1 and 0.15).

Sample	***L****	***a****	***b****	***C****	***h°***	**NIR Reflectance (%)**
x = 0	33.71	-17.71	10.42	20.55	149.53	49
x = 0.05	31.86	-18.06	9.4	20.37	152.5	56
x = 0.10	38.6	-22.65	14.49	26.89	147.39	63
x = 0.15	31.92	-17.85	8.65	19.84	154.14	59

As shown in table 4.10 the *L*a*b** parameters of the optimized pigments were compared with those of Cr_2O_3 green pigment. These pigments possess more color and reflectance than conventional and commercially available Cr_2O_3 green pigment [30]. Pigments possessing low absorbance in the NIR region (1100 nm) can be considered as ideal for cool coatings. Light energy from the sun covers a wide range of radiations. Sun's energy that reaches the earth's atmosphere is made up of around 5% UV, 50% visible and 45% nonvisible infrared radiation. Heat is the direct consequence of absorbance of radiations from the infrared region. Thus, absorbance of radiations from the 700 - 1100 nm region of the infrared region results in the heating up of the surface [31]. The synthesized pigments have a good reflectance in the NIR region, up to 68%, 63% for 10 mol % of Sc^{3+} and Zn^{2+} respectively than that of the conventional Cr_2O_3 green pigment.

Table 4.10 $L^*a^*b^*$ Color Coordinate data for $In_2Cu_{1.9}Zn_{0.1}O_5$ and $In_{1.9}Sc_{0.1}Cu_2O_5$.

Sample	L^*	a^*	b^*	C^*	h°	NIR Reflectance (%)
$In_{1.9}Sc_{0.1}Cu_2O_5$	39.03	-25.16	13.17	28.4	152.38	68
$In_2Cu_{1.9}Zn_{0.1}O_5$	38.6	-22.65	14.49	26.89	147.39	63
Commercial Cr_2O_3 green [30]	51.06	-17.28	18.92	26.0	135	49

4.3.5 *Thermal Stability and Acid/Alkali Resistance Studies of the Pigments*

Thermo-gravimetric analysis of the samples was investigated with a view to find out its thermal stability in the range 30 - 300°C and the results clearly indicate that there is a negligible weight loss of the pigment (Figure 4.12). The chemical resistance of the pigment needs to be established for its possible utility in any substrate. Among the series of colorants synthesized, typically $In_2Cu_2O_5$, $In_{1.9}Sc_{0.1}Cu_2O_5$ and $In_2Cu_{0.9}Zn_{0.1}O_5$ and were tested for its acid and alkali resistance. Acid/alkali resistance of the pigment was carried out in 2% HCl and 2% NaOH. For this, a small amount of weighed sample is mixed with 2% NaOH and 2% HCl and immersed for 1 h with constant stirring. Then the pigment was filtered, washed with distilled water, dried and finally weighed. The negligible weight loss was observed for the acid and alkali treated samples. The color difference ΔE^*_{ab} was calculated from the data before and after each test using the equation 4.9 and is summarized in table 4.11. The smaller values of ΔE_{ab^*} indicate that the pigments are chemically stable towards the acid/alkali.

$$\Delta E^*_{ab} = [(L^*_{after} - L^*_{before})^2 + (a^*_{after} - a^*_{before})^2 + (b^*_{after} - b^*_{before})^2]^{1/2} \tag{4.9}$$

Table 4.11 The color coordinates of pigments after chemical resistance tests.

Sample	Acid				Base			
	L^*	a^*	b^*	ΔE_{ab}^*	L^*	a^*	b^*	ΔE_{ab}^*
$In_2Cu_2O_5$	33.71	-16.35	9.18	1.36	33.50	-15.86	9.01	1.85
$In_2Cu_{1.9}Zn_{0.1}O_5$	38.57	-22.11	14.23	0.54	38.20	-22.18	14.25	0.47
$In_{1.9}Sc_{0.1}Cu_2O_5$	38.75	-24.73	12.93	0.43	38.53	-24.51	12.91	0.65

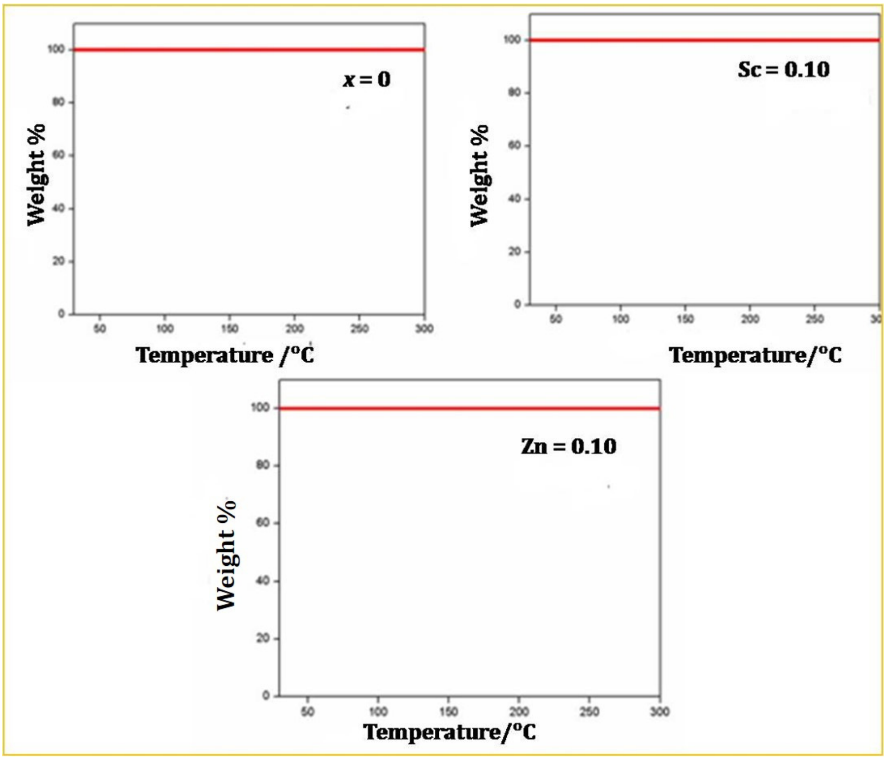

Figure 4.12 Thermo gravimetric analysis of $In_2Cu_{2-x}Zn_xO_5$ and $In_{2-x}Sc_xCu_2O_5$ (x = 0 and 0.1).

The homogeneous and crystalline nature of the sample can be observed in the SEM photographs (Figure 4.13). All the samples have the particle size in the range of 0.5 - 1.5 μm and they are slightly agglomerated. From the micrograph, it is clear that the particle size of $In_{1.9}Sc_{0.1}Cu_2O_5$ is lower than those of $In_2Cu_{0.9}Zn_{0.1}O_5$ and $In_2Cu_2O_5$. This difference is also observed in the reflectance spectrum, where the reflectance of $In_{1.9}Sc_{0.1}Cu_2O_5$ higher than that of the other two. The decrease in reflectance may be due to the presence of increased particles size. The EDS spectra correspondingly showed only peaks of In, Cu, Zn and Sc alongside O. Further, the quantitative analysis of the elements is in close agreement with the stoichiometry of the starting composition (Table 4.12).

Table 4.12 Elemental analysis of $In_2Cu_2O_5$, $In_2Cu_{0.9}Zn_{0.1}O_5$ and $In_{1.9}Sc_{0.1}Cu_2O_5$.

Element	Atomic %	Element	Atomic %	Element	Atomic %
In L	14.98	In L	12.88	In L	14.54
Cu K	14.76	Cu K	11.94	Cu K	15.97
O K	70.25	Zn K	0.79	Sc K	0.69
		O K	74.39	O K	68.80

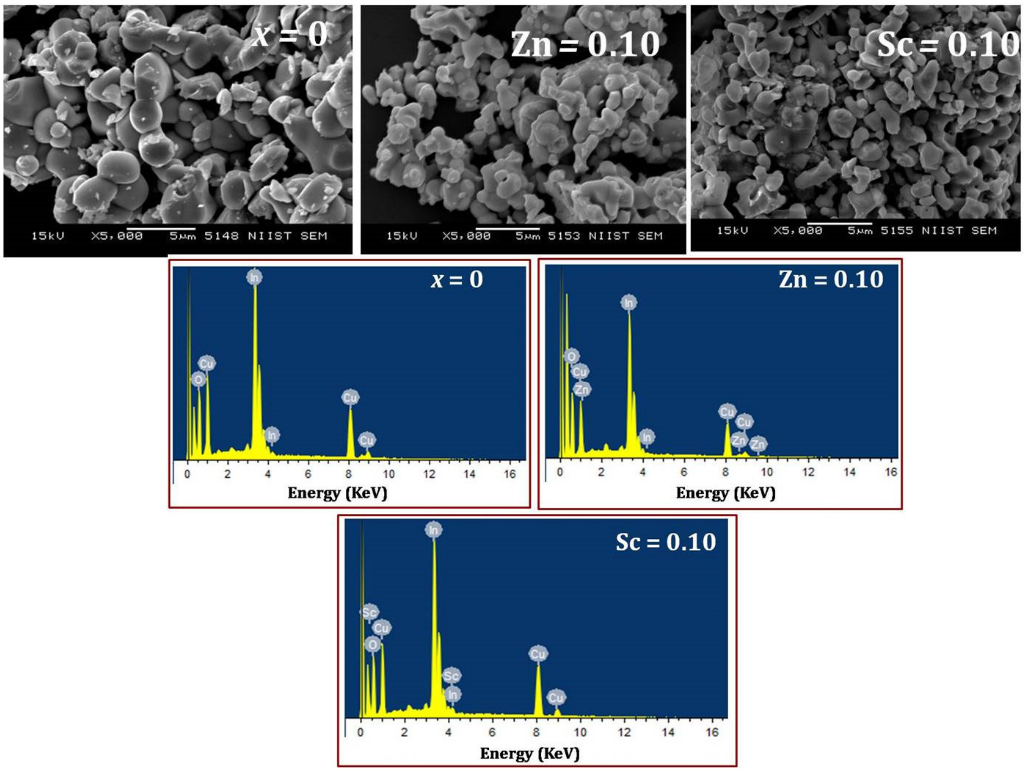

Figure 4.13 Morphological and elemental analysis of $In_2Cu_{2\text{-}x}Zn_xO_5$ and $In_{2\text{-}x}Sc_xCu_2O_5$ (x = 0 and 0.1) through SEM-EDS.

4.4 Conclusions

The $In_2Cu_{2-x}Zn_xO_5$ and $In_{2-x}Sc_xCu_2O_5$ (x = 0, 0.05, 0.1 and 0.15) green pigments were prepared by high temperature solid state method. Doping of Zn^{2+} and Sc^{3+} into the divalent and trivalent site of $In_2Cu_2O_5$ system cause changes in the absorption spectrum and improve its optical properties. The absorption spectrum of $In_{2-x}Sc_xCu_2O_5$ revealed that absorption edge of these compounds, red shifted with an increase in the concentration of Sc^{3+} up to 10 mol%. Since the electronegativity of doped Sc^{3+} lower than that of In^{3+}, this increases the polarizability of the anion. Here the inductive effect of the neighboring cation influences the d-d transition of Cu^{2+} in these compounds. In the $In_2Cu_{2-x}Zn_xO_5$, red shift in the absorption spectrum is due to the distortions caused by the doping of larger Zn^{2+}ion in the host matrix. In the comparison of red shift observed by the doping of both the trivalent and divalent ions, the red shift is pronounced in the Sc^{3+} doped samples. Thus, we can conclude that anion polarizability enhances the red shift than that of smaller average bond length produced by the distortion of the polyhedron by doping of larger ions. The greenness value for $In_2Cu_{1.9}Zn_{0.1}O_5$ and $In_{1.9}Sc_{0.1}Cu_2O_5$ were significantly larger than those of the conventional and commercially available Cr_2O_3 green pigment. Furthermore, C^* value and the $h°$ are also high for these synthesized pigments. These results suggest making them suitable for the environmentally friendly pigment that has sufficient green chromaticity.

4.5 References

1. R. G. Burns, Mineralogical Applications of Crystal Field Theory, Cambridge University Press, Cambridge, United Kingdom (1970).
2. D. S. Gouveia, L. E. B. Soledade, C. A. Paskocimas, E. Longo, A. G. Souza, I. M. G. Santos, Mater. Res. Bull. 41 (2006) 2049.
3. F. Fernández, C. Colón, A. Durán, R. Barajas, A. d'Ors, M. Becerril, J. Llopis, S.E. Paje, R. Sáez-Puche, I. Julián, J. Alloys Compd. 750 (1998) 275.
4. Y. Chen, M. Shang, X. Wu, S. Feng, CrystEngComm. 16 (2014) 5418.
5. R. J .D. Tilley, Color and the Optical Properties of Materials, John Wiley and Sons, Chichester, United Kingdom (2010).
6. P. García-Fernández, M. Moreno, J. A. Aramburu, Inorg. Chem. 54 (2015) 192.
7. J. Lucas, P. Lucas, T. L. Mercier, A. Rollat, W. G. Davenport, Rare Earths: Science, Technology, Production and Use, Elsevier Science, Amsterdam, Netherlands (2014).
8. B. C. Chakoumakos, J. A. Fernandez-Baca, L. A. Boatner, J. Solid State Chem. 103 (1993) 105.
9. Y.-J. Li, S. Ye, C.-H. Wang, X.-M. Wang, Q.-Y. Zhang, J. Mater. Chem. C. 2 (2014) 10395.
10. M. Nazarov, D. Y. Noh, New Generation of Europium- and Terbium-Activated Phosphors, Pan Stanford, Penthouse Level, Singapore (2011).
11. R. J. Xie, Y. Q. Li, N. Hirosaki, H. Yamamoto, Nitride Phosphors and Solid-State Lighting, CRC Press, Boca Raton, Florida (2011).
12. M. Jansen, H. P. Letschert, Nature 404 (2000) 980.
13. R. Famery, F. Queyroux, Mater. Res. Bull. 24 (1989) 275.
14. H.-R. Freund, H. k. Müller-Buschbaum, Z. anorg. allg. Chem. 441 (1978) 103.
15. U. Adem, G. Nénert, Arramel, N. Mufti, G. R. Blake, T. T. M. Palstra, Eur. Phys. J. B. 71 (2009) 393.
16. R. D. Shannon, C. T. Prewitt, Acta Crystallogr. Sect. B. 25 (1969) 925.
17. V. F. Anufrienko, T. M. Yurieva, F. S. Hadzhieva, T. P. Minyukova, S. Y. Burylin, React. Kinet. Catal. Lett. 27 (1985) 201.
18. R. Janes, E. A. Moore, Metal-ligand Bonding, Open University, Milton Keynes, United Kingdom (2004).

19. R. Bruce King, Encyclopedia of Inorganic Chemistry, John Wiley and Sons, New Jersey, United States (2005).
20. M. G. Clark, R. G. Burns, J. Chem. Soc. A. (1967) 1034.
21. E. G. Rogers, P. Dorenbos, J. Lumin. 155 (2014) 135.
22. V. Dimitrov, T. Komatsu, J. Solid State Chem. 196 (2012) 574.
23. A. L. Allred, J. Inorg. Nucl. Chem. 17 (1961) 215.
24. A. M. Srivastava, Opt. Mater. 31 (2009) 881.
25. L. Li, S. Zhang, J. Phys. Chem. B. 110 (2006) 21438.
26. S. Vedanand, B. J. Reddy, Y .P. Reddy, Solid State Commun. 77 (1991) 231.
27. D. J. Newman, B. Ng, Rep. Prog. Phys. 52 (1989) 699.
28. M. A. Hitchman, T. D. Waite, Inorg. Chem. 15 (1976) 2150.
29. N. Komuro, M. Mikami, P. J. Saines, K. Akimoto, A. K. Cheetham, J. Mater. Chem. C. 3 (2015) 7356.
30. H. L. Zhang, S. T. Liang, M. T. Luo, M. G. Ma, P. P. Fan, H. B. Xu, P. Li ,Y. Zhang, Mater. Lett. 117 (2014) 244.
31. A .K. Bendignavale, V. C. Malshe, Recent Patents Chem. Eng. 1 (2008) 67.

5

ENHANCED PIGMENTARY PROPERTIES OF RARE EARTH GERMANATES OF THE TYPE $La_2CuGe_2O_8$ THROUGH DISTORTION IN CuO_6 OCTAHEDRON

Copper based blue-green inorganic pigments, $La_2Cu_{1-x}Li_xGe_{2-x}P_xO_8$ (x = 0, 0.1, 0.2 and 0.3) were synthesized by a conventional solid state method. Optical properties of the synthesized samples are enhanced with the doping of monovalent (Li^+) in the Cu^{2+} site. Absorption spectra measurement reveals that the origin of the color is due to the crystal field splitting of Cu^{2+} ions in the distorted octahedral field. Polarizability of the oxygen ion of Cu–O/Li–O bonds in the solid solutions tunes the crystal field strength around Cu^{2+} ion such that intense blue-green color results for materials with small values of x. Among the samples, the most vivid hue was obtained for $La_2Cu_{0.8}Li_{0.2}Ge_{1.8}P_{0.2}O_8$ with a CIE greenness value of ($a^* = -38.71$). Studies on the coloring applications of the prepared pigments in poly (methyl methacrylate), concrete cement block and metal plate, demonstrate their ability to transfer color and NIR reflectance.

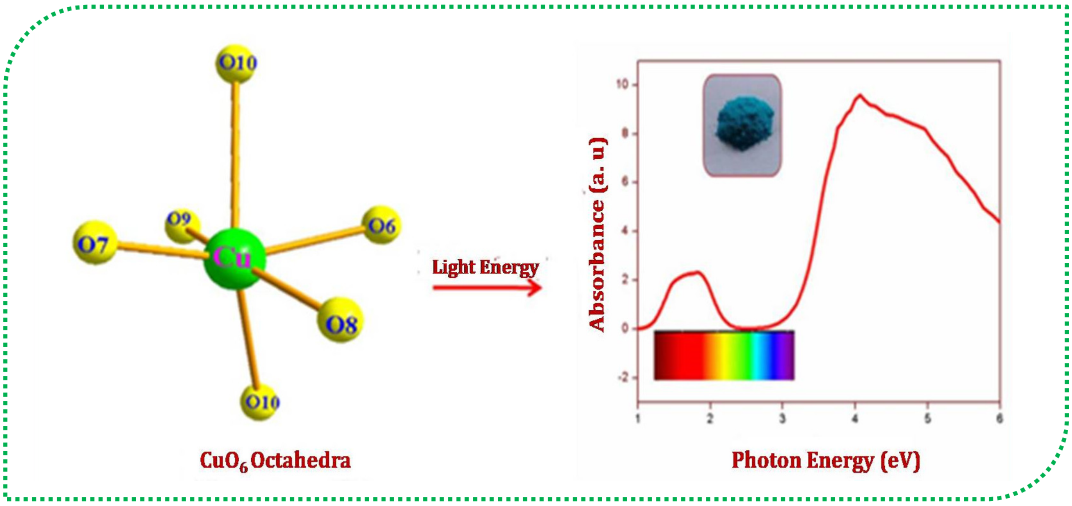

5.1 Introduction

Cu^{2+} based complexes are extremely important as industrial colorants [1, 2]. A great variety of Cu^{2+}compounds is blue or green. A large number of Cu^{2+} based colorants have been developed so far in different crystal structures. Cu^{2+} is considered as a chameleon in coordination chemistry, Cu^{2+} ions are expected to adapt six (octahedral), five (square pyramidal, trigonal bipyramidal) and four (tetrahedral, square planar) coordination. The exotic bright colors of this $MCuSi_4O_{10}$ (M = Ca, Sr and Ba) pigments are due to square planar CuO_4^{6-} chromophore [3, 4.] As heavier alkaline earth elements substitute in $MCuSi_4O_{10}$, systematic increases in the M–O bonds and decreases in the Cu–O bonds are apparent [5]. The creation of a green color in $Y_2Cu_2O_5$ and Y_2BaCuO_5 is due to the crystal field splitting of the d-orbitals of Cu^{2+} in the square pyramidal site (C.N = 5) [6]. It is believed that the d-d electronic transitions give rise to the color in both cases. The coordination chemistry of Cu^{2+} with C.N = 4 and 6 is strongly influenced by distortions induced by Jahn-Teller effects [7]. As an added advantage, Cu^{2+} has only one half-filled electronic orbital ([Ar] $3d^9$), the presence of specific distortion effects, which are connected with the d^9 configuration of copper(II) [8]. The role of the Jahn-Teller effect in influencing the molecular geometries and physical properties of transition-metal complexes has become increasingly apparent in recent years [9-12]. Although the importance of this effect on the structural chemistry of copper(II) has been queried [13,14]. The Jahn-Teller distortion, which is always correlated to the removal of the degeneracy of energy level, results in lowering the symmetry and energy [15]. The magnitude of the splitting of the d-orbitals into appropriate energy levels was dissimilar in both types of compounds because 3d electrons would be expected to interact differently with the surrounding environment (due to the changes in the geometrical arrangement) [16]. A number of parameters need to be considered in describing the optical characteristics of transition metal complexes, these include the peak position, intensity, and width of the absorption band [17]. A number of factors influence the alterations in the chemical environment, changes in the polarizability of the bonds caused by differences in electronegativity between the dopant and its surroundings, leading to changes in covalency; changes in the crystal-field splitting of the ions due to the changes in metal-ligand distances [18]. Ligand-field theory has often been helpful to explain trends in the d-orbitals splitting arising from different chemical environments, which in turn determine the peak absorption (wavelength) [19].

The combination of copper, rare earth (R) and germanium give rise to a large number of Cu-R germanates. Cu-R germanates of stoichiometry $Ln_2CuGe_2O_8$ (Ln = La, Pr-Yb and Y) gives rise to an isostructural series of compounds belonging to the monoclinic structure with a space group of Cm (No.8) [20, 21]. The Crystal structure of $Ln_2CuGe_2O_8$ containing chains of much distorted CuO_6 octahedra. In $Ln_2CuGe_2O_8$ germanium atoms exhibit two different kinds of coordination polyhedra, tetrahedral and triangular bipyramid coordination [20]. The rare earth atoms coordinate to eight oxygen atoms to form LnO_8 triangulated dodecahedra. The CuO_6 octahedra share apical oxygen vertices in the *a* direction and linked in the *b* direction through GeO_4 tetrahedra forming layers. These layers alternate with other layers formed by the union of GeO_5–GeO_4–GeO_5, which share vertices in the *b* direction. These two layers are mutually connected in the *c* direction through GeO_5 bipyramids that have one common face with the CuO_6 octahedra. CuO_6 octahedra are elongated with a different distance from Cu to the apical oxygen and the deformed octahedra show Jahn -Teller distortions [21]. In $Ln_2CuGe_2O_8$ every four LnO_8 polyhedra associated by sharing edges forming tetrameric units, the LnO_8 polyhedra packing gives rise to three different kinds of intersites. The (GeO_4) tetrahedra at the center of each unit and octahedral and trigonal bipyramids formed with the union between the different units, which are Cu, and Ge atoms respectively are shown in figure 5.1. The representative crystal structure of the $La_2CuGe_2O_8$ system is shown in figure 5.2.

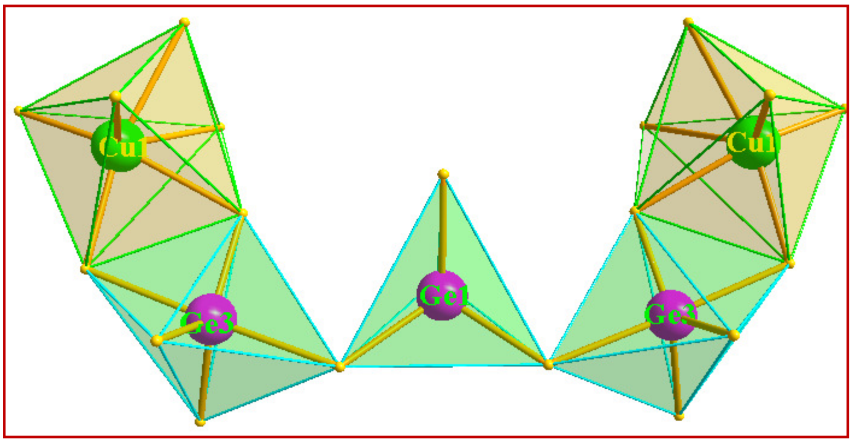

Figure 5.1 Layer formed by the union of GeO_5-GeO_4-GeO_5, through common vertices in the *b* direction and GeO_5 share common face with CuO_6 octahedra.

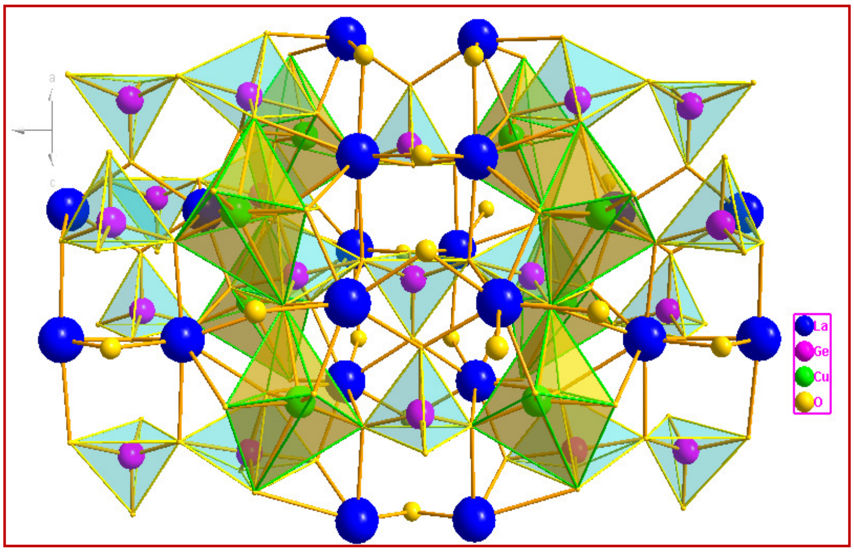

Figure 5.2 Representative crystal structure of $La_2CuGe_2O_8$.

In this work, the change in the color and optical properties of Cu-R germanates were studied. Since there is a lack of available information on the pigmentary properties of germanates containing copper and rare earth metals, we attempted to investigate the characteristics of these systems. As far as we know, none of these compounds have been reported as inorganic pigments to date. Further, in this work, we improve the chromatic properties of the $La_2CuGe_2O_8$ system by the doping of Li^+ in the Cu^{2+} lattice and the charge compensation is accomplished by the doping of P^{5+} in the Ge^{4+} lattice. The valence state of doped alkali metal ions (Li^+) is different from that of the transition metal ion (Cu^{2+}). The difference of valence state and ionic size between the metal ions and the transition elements gives rise to a distortion of the transition metal crystal field, affects the development of a lattice, and improves the optical performances of the materials. In the present work we prepared the compositions based on $La_2Cu_{1-x}Li_xGe_{2-x}P_xO_8$ (x = 0, 0.1, 0.2 and 0.3) inorganic pigments by the conventional solid state method [22]. The present paper presents an analysis of the optical properties of the $La_2CuGe_2O_8$ system and describes their potential application as inorganic pigments.

5.2 Experimental Section

5.2.1 *Materials and Synthesis*

To synthesize $La_2Cu_{1-x}Li_xGe_{2-x}P_xO_8$ (x = 0, 0.1, 0.2 and 0.3) pigments, La_2O_3 (Aldrich, 99.99%), Li_2CO_3 (Aldrich, 99.9%), CuO (Aldrich, 99.9%), GeO_2 (Aldrich, 99.998%) and $NH_4H_2PO_4$ (Aldrich, 99.999%) were used as the starting materials. The stoichiometric amount of the weighed samples is mixed thoroughly in an agate mortar using acetone as the mixing medium. In a typical pigment sample $La_2Cu_{0.9}Li_{0.1}Ge_{1.9}P_{0.1}O_8$, La_2O_3 (52.97 mg, 0.16 mmol), CuO (11.64 mg, 0.14 mmol), Li_2CO_3 (1.19 mg, 0.016 mmol), GeO_2 (32.31 mg, 0.31mmol) and $NH_4H_2PO_4$ (1.86mg, 0.016 mmol) were mixed for four times using a mortar with acetone and then the mixture was dried in an oven at 100°C for 30 min to evaporate acetone. Finally, the dried mixtures were placed in platinum crucibles and calcined in an electric furnace at 900- 1000°C for 6 h, using a heating rate of 5°C/min. Here the formation temperature of the undoped sample is 1000°C/6 h and the doped samples are formed at 900°C/6 h. The calcined samples were ground thoroughly into fine powders in an agate mortar for further studies.

5.2.2 *Characterization*

Formation of single-phase product and their crystalline structure was studied by using powder X-ray diffraction. The PXRD pattern was taken with the aid of PANalytical X'Pert Pro diffractometer (Ni-filtered Cu Kα radiation, λ = 1.5406 Å). The structural parameters of the samples were refined by the Rietveld method using the X'Pert HighScore Plus software. The data were recorded over the 2θ range of 10-90°. The morphology and elemental analysis of the prepared samples were examined by scanning electron microscopy (JEOL JSM-5600 LV SEM) and energy dispersive spectrometer (EDS). For characterization of pigment quality of the samples (the color parameters), the diffuse reflectance spectra were recorded (220 - 2500 nm) employing a UV-vis spectrometer (Shimadzu UV-3600) using PTFE as the reference. The CIE 1976 $L^*a^*b^*$ colorimetric method was used, as recommended by the Commission Internationale de l'Eclairage (CIE). In this method, L^* is the lightness axis [black (0) to white (100)], a^* is the green (−ve) to red (+ve) axis, and b^* is the blue (−ve) to yellow (+ve) axis. The parameter, C^* (chroma) represents saturation of the color and is calculated using the equation 5.1.

$$C^* = [(a^*)^2 + (b^*)^2]^{1/2} \tag{5.1}$$

and $h°$ represents the hue angle. The hue angle $h°$ is expressed in degrees, ranges from 0 to 360°, and is calculated by using the formula 5.2.

$$h° = tan^{-1}(\frac{b^*}{a^*}) \tag{5.2}$$

The band gap values were calculated using the Kubelka-Munk function, which is given in the equation 5.3

$$f(R) = (1 - R)^2/2R \tag{5.3}$$

Where R is the reflectance value. The thermal stability of the colorant was also checked using a (HITACHI, STA7300 thermal analysis) make in an argon atmosphere at a heating rate of 10°C/min.

5.3 Results and Discussion

5.3.1 *Structural Analysis of $La_2Cu_{1-x}Li_xGe_{2-x}P_xO_8$ (x = 0, 0.1, 0.2 and 0.3)*

The crystalline structure of the prepared $La_2Cu_{1-x}Li_xGe_{2-x}P_xO_8$ (x = 0, 0.1, 0.2 and 0.3) samples were investigated by powder X-ray diffraction. Figure 5.3 represents the PXRD patterns of the synthesized samples. From the PXRD patterns all the diffraction peak of the samples matched with those of monoclinic structure (JCPDS No. 00-034-0391), however a low intense diffraction peak at 2θ = 28° belongs to a minor impurity phase of $CuGeO_3$ was observed in all the samples (marked as asterisk).

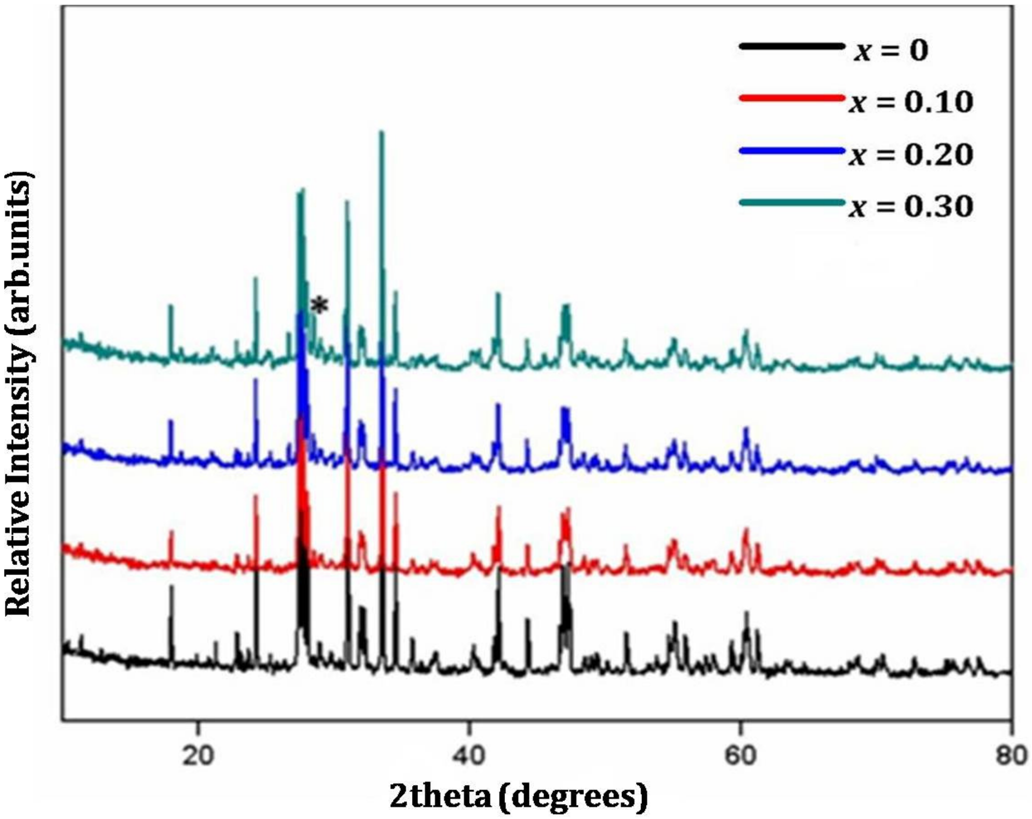

Figure 5.3 Powder XRD patterns of $La_2Cu_{1-x}Li_xGe_{2-x}P_xO_8$ (x = 0, 0.1, 0.2 and 0.3).

Furthermore, we observed shifting of diffraction peaks towards the lower angle side with doping. It is well known that the size of the ionic radius of the substituting cation influences the resultant change in the lattice parameters. This can be attributed to the change in the host lattice caused by substitution of Cu^{2+} (C.N (VI) = 0.73 Å) ions by larger Li^+ (C.N (VI) = 0.74 Å) ions [23], which results in the expansion of the lattice parameters. The difference in the valence state of the alkali metal ion and transition metal gives rise to a distortion in the crystal field of the transition metal ion; this affects the lattice parameters of the doped samples. Rietveld refinements of the doped samples were performed with the aid of X'Pert High Score Plus to extract the lattice parameters and bond length. The crystallographic data of previously reported $CuNd_2Ge_2O_8$ as the starting model was employed to refine the patterns of the doped samples.

Table 5.1 Lattice constants of $La_2Cu_{1-x}Li_xGe_{2-x}P_xO_8$ (x = 0, 0.1, 0.2 and 0.3).

x	0	0.1	0.2	0.3
a (Å)	8.8874(3)	8.8902(3)	8.9007(3)	8.9013(5)
b (Å)	15.1640(3)	15.1666(3)	15.1732(3)	15.1792(3)
c (Å)	7.9370(3)	7.9398(3)	7.9529(3)	7.9606(3)
β (degrees)	145.7926(2)	145.6875(3)	145.7159(2)	145.7580(2)

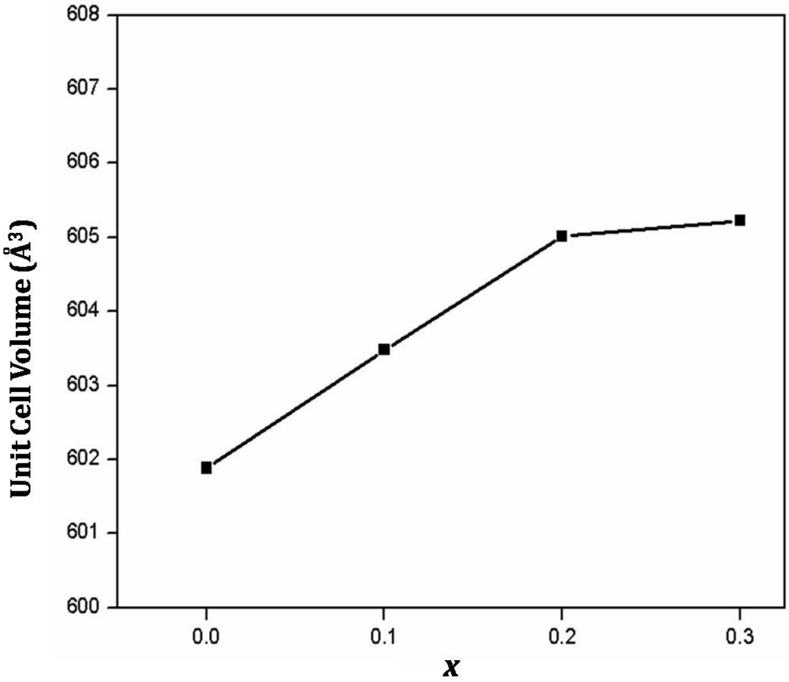

Figure 5.4 Lattice volume variation of $La_2Cu_{1-x}Li_xGe_{2-x}P_xO_8$ (x = 0, 0.1, 0.2 and 0.3).

According to PXRD patterns of doped samples, the lattice parameters were calculated and are summarized in the above table 5.1. The cell volume (V) varies with increasing the doping concentration as shown in figure 5. 4. The results show that doping the metal cations makes a small distortion of the CuO_6 crystal field and do not change the phase at all. From the refinement data, we found that the Cu–O distances varying with increasing the doping concentrations shown in table 5.2. The Cu site is coordinated with six oxygen atoms with Cu–O distances of 1.806 Å - 2.523 Å. The octahedral coordination around the Cu atom, represented in the figure. 5.5 is strongly Jahn–Teller distorted due to the effect of the Cu^{2+} ion, which has four short Cu–O bonds in the range of 1.806 - 2.094 Å, and two long Cu–O bonds in the range of 2.331 - 2.523 Å.

Table 5.2 Cu–O bond distances of $La_2Cu_{1-x}Li_xGe_{2-x}P_xO_8$ (x = 0, 0.1, 0.2 and 0.3).

Bond length (Å)	***x* = 0**	***x* = 0.1**	***x* = 0.2**	***x* = 0.3**
Cu_1 - O7	1.8270(1)	1.8059(7)	1.8110(2)	1.8130(1)
- O8	1.8640(6)	1.8450(1)	1.8370(1)	1.8310(6)
- O9	2.0240(1)	2.0440(4)	2.0806(4)	2.0670(2)
- O6	2.0290(1)	2.0940(3)	2.0860(1)	2.0910(5)
- O10	2.3429(2)	2.3557(7)	2.3779(9)	2.3310(9)
- O10′	2.5230(4)	2.4710(4)	2.4776(1)	2.5110(2)

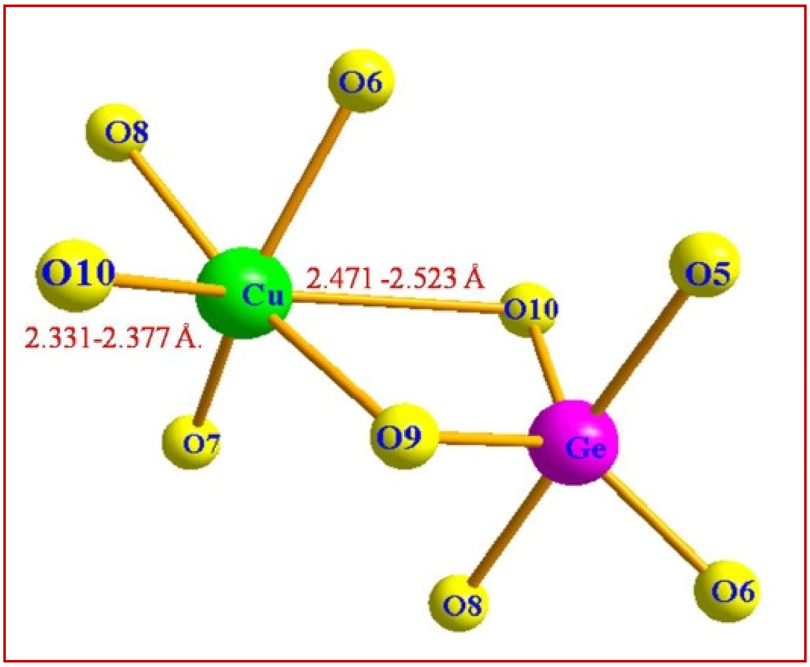

Figure 5.5 Cu–O bond lengths in $La_2Cu_{1-x}Li_xGe_{2-x}P_xO_8$ (x = 0, 0.1, 0.2 and 0.3).

5.3.2 *UV-Visible Studies*

To understand the origin of color we measured the diffuse reflectance spectra of the prepared samples then absorption spectra were made using the Kubelka- Munk function. Figure 5.6 represents the absorption spectra of $La_2Cu_{1-x}Li_xGe_{2-x}P_xO_8$ (x = 0, 0.1, 0.2 and 0.3) developed pigment powders. All samples exhibit strong optical absorptions at wavelengths below 400 nm and longer than 600 nm. The position of the absorption bands for a given transition metal ion depends on the specific structural details of its environment. Cu^{2+} has an electronic configuration of $(t_{2g})^6 (e_g)^3$. The energy level of a $3d^9$ (Cu^{2+}) ion will be split into ^2E_g and $^2T_{2g}$ with the ground state ^2Eg possessing octahedral symmetry. As the symmetry of the coordination is reduced the energy levels are further split. The largest Jahn Teller distortions are found when the degeneracy is in the e_g orbitals which occurs when they are occupied by one or three electrons. Two structural changes are possible one is elongated and the other is compressed. It is observed that elongated structures are more energetically favorable than the compressed ones [24]. In the crystal structure of $La_2CuGe_2O_8$, the copper ion polyhedra exhibit the characteristic distortion of four short bonds and two long bonds. Therefore, in the present system, Cu^{2+} ions are in the tetragonally elongated octahedral environment.

In the elongated tetragonally distorted octahedral environment, the ^2Eg level may be further split into $^2A_{1g}$ (d_{z^2}) and $^2B_{1g}$ ($d_{x^2-y^2}$), and $^2T_{2g}$ level into ^2Eg (d_{xz}, d_{yz}) and $^2B_{2g}$ (d_{xy}) the ground state being $^2B_{1g}$ [25]. The broad weak absorption band located in the 600 - 820 nm regions corresponds to the well known d–d transition for Cu^{2+} ion in the tetragonally distorted octahedral field. For $Cu^{2+}$with elongated octahedral symmetry, more than one band will be observed [26]. But only a single optical absorption maximum was observed in most of the cases [27, 28]. The absorption band located in the 600 - 820 nm is assigned to the transitions of Cu^{2+} ions from $^2B_{1g}$ to $^2B_{2g}$ in a distorted octahedral site. This single optical band was interpreted as the overlap of all the three transitions ($^2B_{1g} \rightarrow {}^2A_{1g}$, $^2B_{1g} \rightarrow {}^2B_{2g}$ and $^2B_{1g} \rightarrow {}^2Eg$). The strong absorption band located below in the 400 nm region is attributed to the charge transfer transition take place from the ligand to metal ion (O^{2-} to Cu^{2+}) [29]. The variations in the intensity of optical transitions in the charge transfer and visible regions are very pronounced. The weak absorption of all d-d transitions is due to forbidden transitions compared to charge transfer transitions, which are allowed and occur with a greater probability.

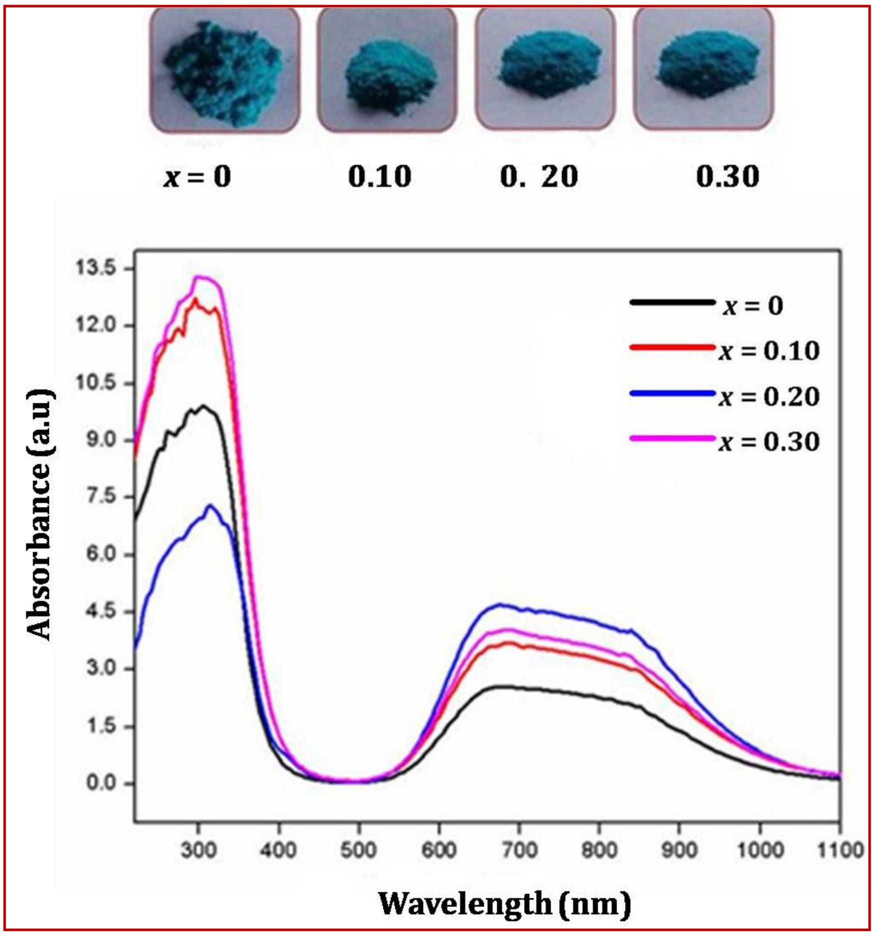

Figure 5.6 Color and absorbance spectrum of $La_2Cu_{1-x}Li_xGe_{2-x}P_xO_8$ (x = 0, 0.1, 0.2 and 0.3).

The peak position is shifted to the shorter wavelength region with the increase of the doping concentration up to 20 mol% beyond this concentration the peak position is shifted towards higher wavelength. A number of parameters need to be considered in describing the optical characteristics of transition- metal ions. According to crystal field theory, the site symmetry, ligand charge, bond length and covalence have an important influence on the crystal field strength [30]. The relationship between the crystal field strength (Dq) and R is expressed by the following equation 5.4. It is noteworthy that the crystal field strength decreases when the interatomic distance increases [31], can be shown using the equation 5.4:

$$Dq = \frac{3Ze^2r^4}{5R^5} \tag{5.4}$$

Where Z is the valence charge of the anion, R represents the distance between the central ion and its ligands, and r is the mean size of the central ion. It can be seen from the equation that Dq is inversely proportional to the fifth power of the bond length R. This is the typical case for the relationship between the lattice volume and the absorption wavelength being affected by the crystal fields on the cation sites. When relatively larger Li^+ ions are doped in the Cu^{2+} site of the $La_2CuGe_2O_8$ system the lattice volume increases up to 20 mol% of doping concentration. Longer Cu–O bonds generally lead to higher absorption energy or shorter wavelength and decrease the crystal field splitting. The structural distortion of the CuO_6 octahedron affects the Cu–O hybridization because longer Cu–O bonds usually correspond to weaker Cu–O hybridization. The results in table 5.2 from structural analysis confirm the above observations. The weak hybridization can be caused by long Cu–ligand distance and/or distorted bond angles around the Cu ion the distorted octahedral site.

In addition, the blue shift of the absorption spectrum indicated the fluctuation in ligand field around the Cu^{2+}ion, which is related to change in polarizability of oxygen ion surrounding the Cu^{2+} and its dependence on field strength. It is well known that anion polarizability depends on the electronegativity of the cation to which they are bound and anion polarizability increases with decreasing the electronegativity of the cation. The electronegativity (χ) of Li^+ (0.98) is smaller than that of Cu^{2+} (1.98) [32]. In the $La_2Cu_{1-x}Li_xGe_{2-x}P_xO_8$ system, based on the electronegativity point of view, less electronegative Li^+ ions are not able to attract the O^{2-}towards them relative to the smaller and most electronegative Cu^{2+} ion. When the less electronegative Li^+ is incorporated in these materials, negative charge density around the O^{2-} will be higher and the distance between the Cu^{2+} and center of charge density on the O^{2-} ion will be increased. This leads to the lengthening of the {Cu,Li}–O bond, which in turn will render a weaker crystal field at the Cu^{2+} site in the doped samples [33]. This broadening and the blue shift of the absorption bands with increasing concentrations have contributed highly for the optical properties of the samples [34].

The chromatic properties of the powdered pigment samples were evaluated using the CIELAB 1976 color space and employing a D65 illuminant. The chromatic values described in terms of L^*, a^* and b^*coordinates for x doping varying from 0 to 0.3 is shown in table 5.3. The systematic doping of x ranging from (0 to 0.2) in the $La_2Cu_{1-x}Li_xGe_{2-x}P_xO_8$ results in an increase in the a^* value from -32.28 to -38.71 indicating an increasing green color. The decrease of green tinge is observed by increasing the doping concentration of x above 20 mol %. The most vivid green hue was obtained for $La_2Cu_{0.8}Li_{0.2}Ge_{1.8}P_{0.2}O_8$ sample.

Table 5.3 $L^*a^*b^*$ color coordinate data for $La_2Cu_{1-x}Li_xGe_{2-x}P_xO_8$ (x = 0, 0.1, 0.2 and 0.3).

Sample	L^*	a^*	b^*	C^*	h°	**Band Gap (eV)**
x = 0	74.10	-32.28	-15.75	35.92	206	2.10
x = 0.1	78.18	-34.09	-14.16	36.54	203	2.13
x = 0.2	72.57	-38.71	-17.23	42.37	202	2.15
x = 0.3	71.38	-33.83	-15.10	36.54	203	2.14

The effect of doping is also reflected in its color saturation value (C^*) of the pigment which increases from 35.92 to 42.37and the hue angle decreases from 206 to 202. Here the color purity value (h°) of 206 corresponds to the blue- green color, as the doping concentration of Li^+ increases the hue angle (h°) and the greenish tint increases, for pure green the hue angle is equal to 180.

Doping Li^+ for Cu^{2+} in $La_2CuGe_2O_8$ (x = 0, 0.1, 0.2 0.3) shows an NIR reflectance (1100 nm) in the range of 58 to 51% (Figure 5.7). Thus, absorbance of radiation from the 700 - 1100 nm region of the infrared region results in the heating up of the surface. Here we can see that NIR reflectance of the doped samples decreases with increasing the doping, this is due to the increased particle size with increasing the amount of dopants. It is evident from the reflectance spectra of these pigments that the progressive doping amount of Li^+ for Cu^{2+} in $La_2CuGe_2O_8$ gently changes the absorption edge, to the shorter wavelength region, which results in a blue shift of the d–d transition band of Cu^{2+} and improvement of the green hue of $La_2CuGe_2O_8$ pigments. Thus the band gaps of $La_2Cu_{1-x}Li_xGe_{2-x}P_xO_8$ pigment samples increased from 2.10 to 2.15 eV with the increase of Li^+ doping amount x from 0 to 0.2, further increasing of doping concentration decreases the band gap.

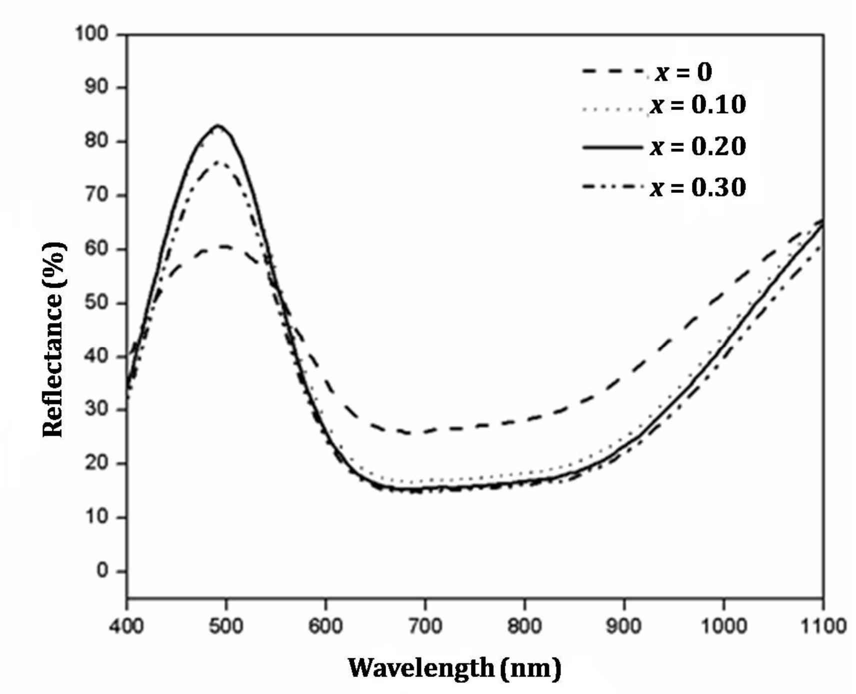

Figure 5.7 NIR reflectance spectra of $La_2Cu_{1-x}Li_xGe_{2-x}P_xO_8$ (x = 0, 0.1, 0.2 and 0.3).

5.3.3 *Coating Studies*

To study the potential of the pigments as colorants for various applications, we tested the color characteristics on various substrates. The ability of the pigment to transfer its color to a polymer substrate was examined by incorporating it into plastic materials like PMMA. The coloring performance of the typical efficient pigment, $La_2Cu_{0.8}Li_{0.2}Ge_{1.8}P_{0.2}O_8$ obtained from among the series of pigments synthesized was also evaluated. This was done by incorporating the pigment into a polymer substrate like poly (methyl methacrylate) (PMMA; Sigma Aldrich). PMMA is a well known water soluble polymeric material extensively used for cold extrusion of many inorganic oxides such as alumina and zirconia. A viscous solution of PMMA (90 wt. %) was made using a conventional electric coil heater and 10 wt. % of the pigment was slowly added with stirring and converted into a thick paste by adding acralyn cold curing liquid (Asian Acrylates, India).The resulted viscous thick paste was allowed to set in cylindrical molds by keeping them in the air for 6 h. Each side of the dried polymer compact was polished to a fine surface using a fine-grade emery sheet. Cylindrical discs containing 10 wt. % of the pigment sample were prepared, whose photograph is shown in figure 5.8. The color coordinates of the pigment incorporated polymer discs were measured at different locations of that and an average value are depicted in table 5.4. The color coordinate values obtained were almost the same indicating the uniform distribution of pigment particles in the polymer matrix.

Figure 5.8 Photograph of 10% $La_2Cu_{0.8}Li_{0.2}Ge_{1.8}P_{0.2}O_8$ coated on PMMA.

Table 5.4 The color coordinates of the $La_2Cu_{0.8}Li_{0.2}Ge_{1.8}P_{0.2}O_8$ pigment powder after applying in polymer.

Sample	Color coordinates				
	L*	***a****	***b****	***C****	***h*** °
$La_2Cu_{0.8}Li_{0.2}Ge_{1.8}P_{0.2}O_8$	72.57	-38.71	-17.23	42.37	202
$La_2Cu_{0.8}Li_{0.2}Ge_{1.8}P_{0.2}O_8$ (10 %) + PMMA	58.36	-38.45	-13.27	40.68	199

The typical developed pigment $La_2Cu_{0.8}Li_{0.2}Ge_{1.8}P_{0.2}O_8$ with superior chromatic properties was selected to evaluate the color and reflectance properties. In order to assess the performance of the pigments as cool colorants for reducing the heat buildup, we have evaluated the color and NIR reflectance of the designed pigments by coating onto a roofing material like the concrete cement block and metal sheet. The photographs of the resultant coating samples are depicted in figure 5.9 and figure 5.10. The coating was undertaken in a two step process. In the first step the concrete cement block and metal sheet surfaces were coated with a NIR reflective inexpensive white pigment TiO_2, and in the next step, the synthesized pigment was applied to the pre-coated concrete cement block. The pigment to binder ratio as 1:1 by weight, were dispersed in an acrylic acralyn emulsion by ultrasonication

(Vibronics, 250 W, India) after grinding and sieving the pigment under 35 mm mesh size. The homogeneous viscous solution was then coated on a concrete cement block surface followed by drying in air. The pigment coated over bare concrete and a metal plate possess a NIR reflectance of 51% and 50%, whereas the pigment over a TiO_2 base coat exhibited a NIR reflectance of 58% and 57%. (Table 5.5) These coatings can reduce the surface temperature of the roof and lead to energy savings. The reflectance of the typical pigment sample coated directly over the concrete material and coated over a base coat of TiO_2 on the roofing material is shown in figure 5.11

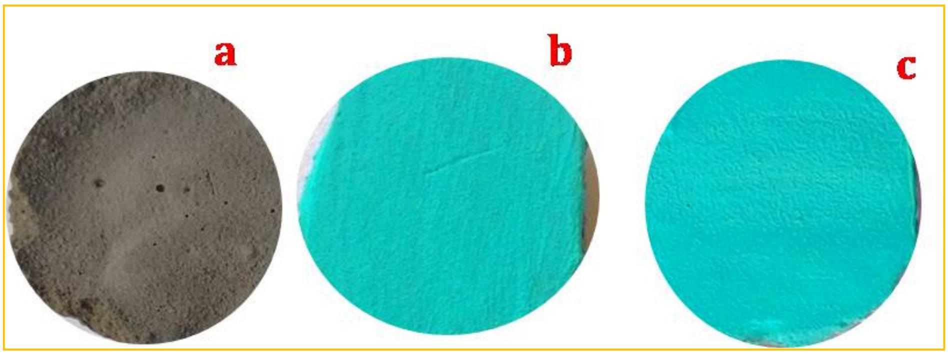

Figure 5.9 Photographs of a) bare concrete b) pigment coated cement block c) pigment coated over a TiO_2 base coat on cement blocks.

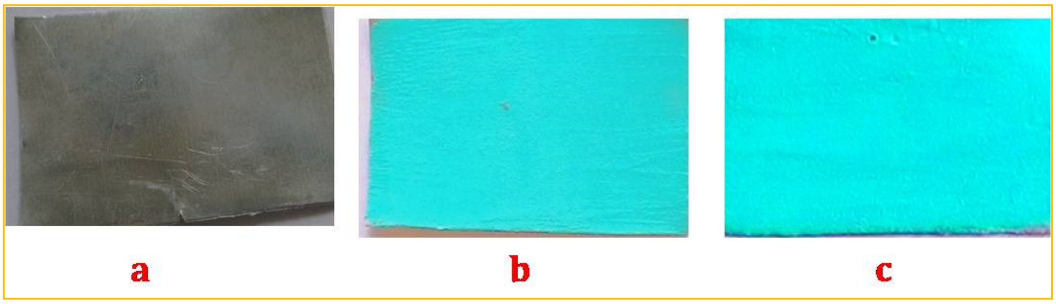

Figure 5.10 Photographs of a) bare metal plate b) pigment coated metal plate c) pigment coated over a TiO_2 base coat on metal plate.

Table 5.5 The color coordinates of the $La_2Cu_{0.8}Li_{0.2}Ge_{1.8}P_{0.2}O_8$ pigment coated over a bare, TiO_2 coated concrete block, and metal plate.

Color coordinates	**Concrete block**		**Metal plate**	
	Bare	**TiO_2 Coat**	**Bare**	**TiO_2 Coat**
L^*	70.01	72.07	71.54	71.43
a^*	-37.72	-38.63	-34.57	-36.34
b^*	-13.55	-16.02	-13.55	-16.24
C^*	38.72	40.39	37.13	40.55
h°	200	202	201	203
NIR Reflectance (%)	51	58	50	57

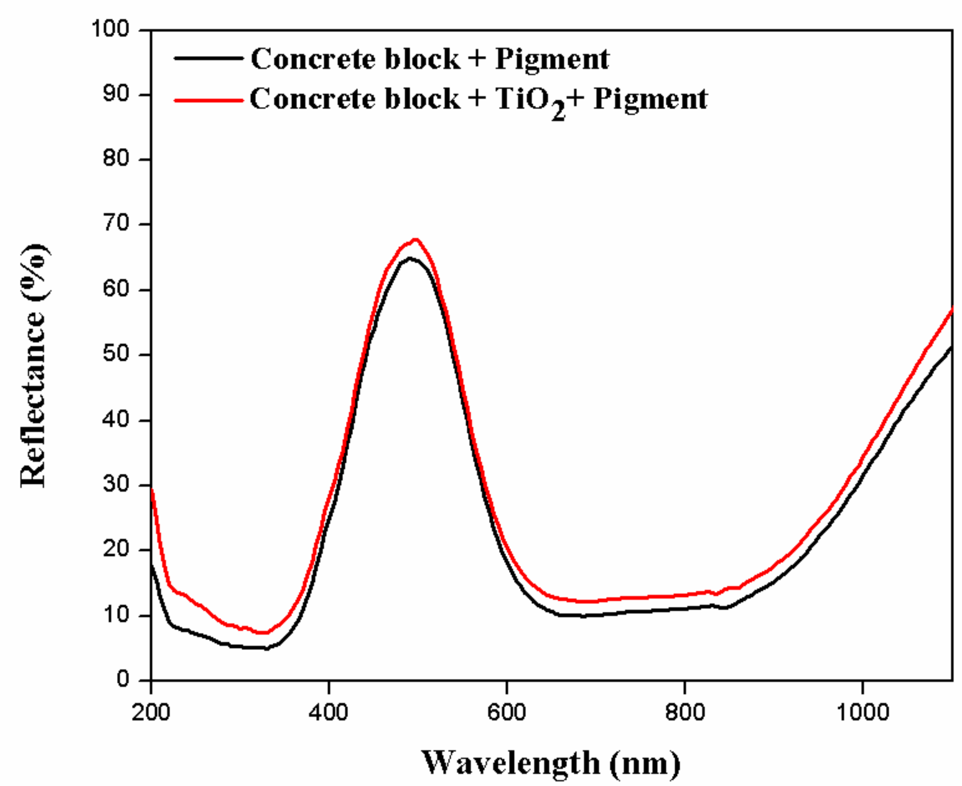

Figure 5.11 NIR reflectance of pigment coated concrete cement block with and without TiO_2 base coat.

5.3.4 *Light resistance studies*

The light resistance of the typical pigmented coating on a concrete block was evaluated in a rudimentary manner by exposing the coating to natural sunlight at the interval of one day and measured the color coordinates. The color stability of the inorganic pigment is normally considered to be good when the $\varDelta E^*_{ab}$ value is less than ($\varDelta E^*_{ab} \leq 2$), which is the industrially acceptable limits of color difference ($\varDelta E^*_{ab}$) [35]. After the exposing the coating to natural sunlight for five days, the color difference was calculated from the color coordinates of the resultant treated samples and untreated samples, as a result, the value of ΔE^*_{ab} is 0.82 (Table 5.6). However, more exposure tests are necessary to qualify as a durable pigment for any commercial application. The color difference ΔE^*_{ab} was calculated from the data before and after each test using the following equation 5.5.

$$\Delta E^*_{ab} = [(L^*_{after} - L^*_{before})^2 + (a^*_{after} - a^*_{before})^2 + (b^*_{after} - b^*_{before})^2]^{1/2} \tag{5.5}$$

Table 5.6 Color coordinates of $La_2Cu_{0.8}Li_{0.2}Ge_{1.8}P_{0.2}O_8$ pigment in concrete block on exposure to sunlight.

Time duration	L^*	a^*	b^*	$\varDelta E^*_{ab}$
0	70.01	-37.72	-13.55	–
Day 1	69.92	-37.61	-13.43	0.19
Day 2	69.79	-37.52	-13.33	0.38
Day 3	69.68	-37.40	-13.17	0.61
Day 4	69.62	-37.37	-13.13	0.69
Day 5	69.53	-37.30	-13.07	0.82

5.3.5 *Thermal Stability and Chemical Resistance Studies of $La_2Cu_{0.8}Li_{0.2}Ge_{1.8}P_{0.2}O_8$ pigment*

Thermo-gravimetric analysis of the samples was investigated with a view to find out its thermal stability in the range 50 - 300°C and the results clearly indicate that there is an insignificant weight loss (0.29 %) of the pigment in the above temperature range (Figure 5.12). The chemical resistance of the pigment needs to be established for its possible utility in any substrate. The evaluation was done using the typical pigment $La_2Cu_{0.8}Li_{0.2}Ge_{1.8}P_{0.2}O_8$. Acid/alkali/water resistance of the pigment was carried out in 2% HCl, 2% NaOH and H_2O. For this, a small amount of weighing sample is mixed with 2% NaOH/2% HCl/water and immersed for 1 h with constant stirring. Then the pigment was filtered, washed with distilled water, dried and finally weighed. Negligible weight loss was observed for the acid, alkali and water treated samples. The total color difference ΔE^*_{ab} was calculated and is summarized in table 5.7. Smaller values of ΔE^*_{ab} indicate that the pigments are chemically stable towards the acid/alkali.

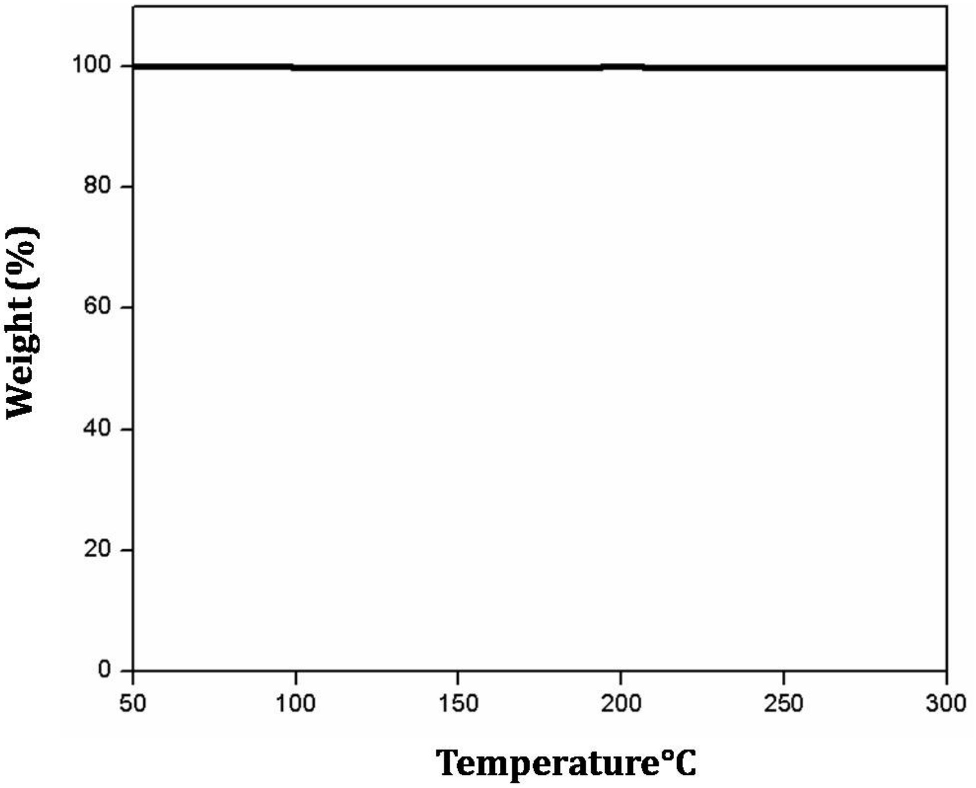

Figure 5.12 TGA of $La_2Cu_{0.8}Li_{0.2}Ge_{1.8}P_{0.2}O_8$ pigment.

Table 5.7 The color coordinates of the $La_2Cu_{0.8}Li_{0.2}Ge_{1.8}P_{0.2}O_8$ powder pigments after chemical resistance test.

Acid/ Alkali	L^*	a^*	b^*	ΔE^*_{ab}
$La_2Cu_{0.8}Li_{0.2}Ge_{1.8}P_{0.2}O_8$	72.57	-38.71	-17.23	-
HCl	71.90	-38.21	-17.05	0.8
NaOH	71.81	-38.13	-17.11	0.9
H_2O	72.16	-38.12	-17.08	0.67

5.3.6 *Morphological and Elemental Analysis of $La_2Cu_{1-x}Li_xGe_{2-x}P_xO_8$ (x = 0, 0.1, 0.2 and 0.3)*

From the scanning electron micrograph, it can be seen that all of the samples have a particle size less than 5 μm and they are highly agglomerated (Figure 5.13). As the amount of dopant increased the extent of agglomeration reduced. From the micrograph, it is clear that the particle size of the doped sample is higher than that of undoped one. Undoped sample and low doping concentration contain aggregates of small particles; this provides greater surface area contributing to higher NIR reflectance. The EDS spectra of $La_2Cu_{0.8}Li_{0.2}Ge_{1.8}P_{0.2}O_8$ correspondingly showed only peaks of La, Cu, Ge and P alongside O. The Li element is not detected due to going beyond the detection range of the instrument Further the quantitative analysis of the elements is in close agreement with the stoichiometry of the starting composition (Figure 5.14)

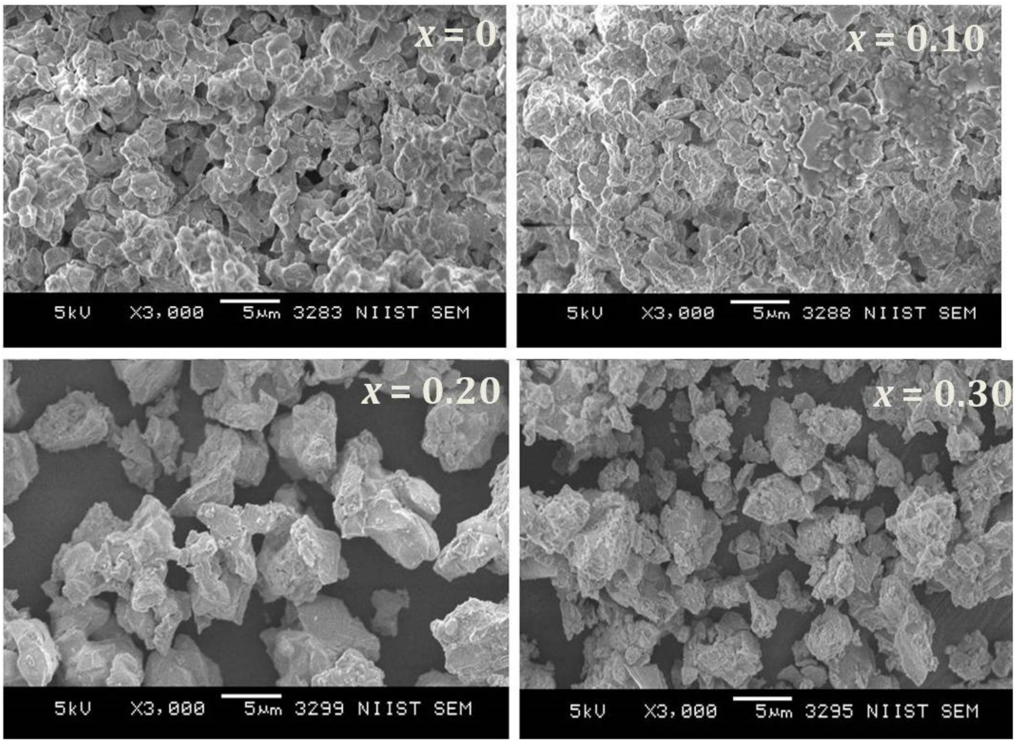

Figure 5.13 SEM photographs of $La_2Cu_{1-x}Li_xGe_{2-x}P_xO_8$ (x = 0, 0.1, 0.2 and 0.3).

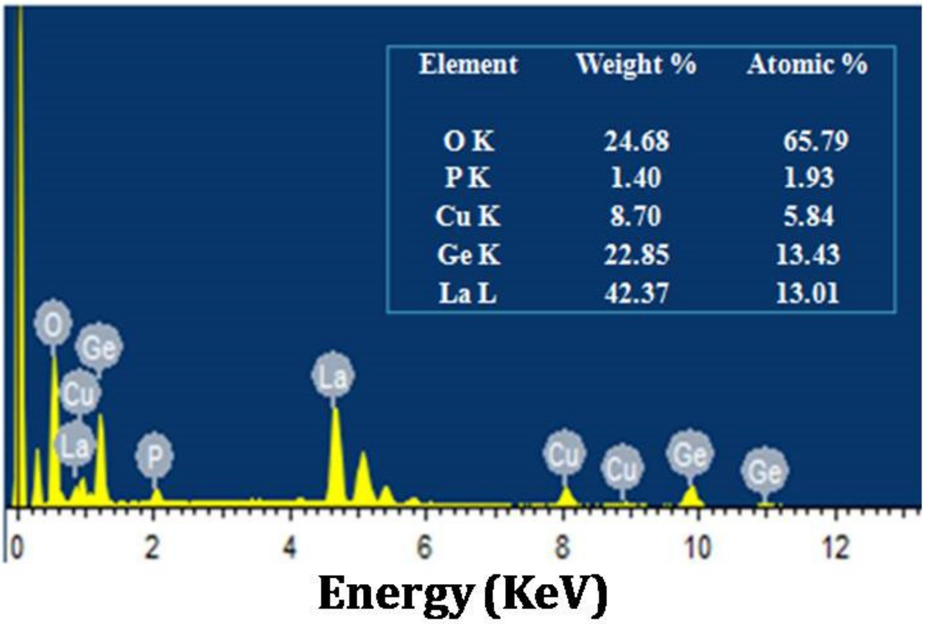

Element	Weight %	Atomic %
O K	24.68	65.79
P K	1.40	1.93
Cu K	8.70	5.84
Ge K	22.85	13.43
La L	42.37	13.01

Figure 5.14 Elemental analysis of $La_2Cu_{0.8}Li_{0.2}Ge_{1.8}P_{0.2}O_8$ through SEM-EDS.

5.4 Conclusions

$La_2CuGe_2O_8$ based, environmentally friendly inorganic blue-green pigments were prepared successfully. Doping Li^+ and P^{5+} into the divalent and tetravalent site of $La_2CuGe_2O_8$ systems improved the optical properties exhibiting brilliant blue-green colors. The synthesized pigments show color reproducibility and the most vivid hue was obtained for $La_2Cu_{1-x}Li_xGe_{2-x}P_xO_8$ ($x = 0.2$) which has $L^*a^*b^*$ color parameters of $L^* = 72.57$, $a^* = -38.71$, $b^* = -17.23$. The results demonstrated that doping of Li^+ for Cu^{2+} enhances the color of the $La_2CuGe_2O_8$ pigment. The enhanced pigmentary properties are mainly attributed to the tiny distortion of the crystal field environment around the CuO_6 octahedra. The technological performances of the synthesized pigment were demonstrated effectively transferring color and reflectance to the plastic, concrete block and metal plate. Our preliminary investigation indicates the prepared pigments show signs of thermal and chemical stability and light resistance.

5.5 References

1. B. C. Chakoumakos, J. A. Fernandez-Baca, L. A. Boatner, J. Solid State Chem. 103 (1993) 105.
2. W. A. Weyl, Colored Glasses, Society of Glass Technology, Sheffield, United KIngdom (1951).
3. M. G. Clark , R. G. Burns, J. Chem. Soc. A. (1967) 1034.
4. T. E. Warner, Synthesis, Properties and Mineralogy of Important Inorganic Materials, Wiley, West Sussex, United Kingdom (2011).
5. C. R. Bamford, Color Generation and Control in Glass, Elsevier Scientific Publishing Company, Amsterdam And New York(1977).
6. M. N. PoPova, I. V. Paukov, Phys. Lett. A. 159 (1991) 187.
7. D. Reinen, Comments Inorg. Chem. 2 (1983) 227.
8. A. Putnis, Introduction to Mineral Sciences, Cambridge University Press, Cambridge, United Kingdom (1992).
9. A. Putnis, Coord. Chem. Rev. 14 (1975) 357.
10. J. bGaăzo, I. B. Bersuker, J. Garaj, M. Kabešová, J. Kohout, H. Langfelderová, M. Melník, M. Serator, F. Valach, Coord. Chem. Rev. 19 (1976) 253.
11. I. B. Bersuker, The Jahn-Teller Effect and Vibronic Interactions in Modern Chemistry, Plenum Press, New York (1984).
12. R. Englman, The Jahn-Teller Effect in Molecules and Crystals, Wiley-Interscience, London (1912).
13. J. K. Burdett, Inorg. Chem. 20 (1981) 1959.
14. D. W. Smith, J. Chem. Soc. A (1970) 1498.
15. R. J. Deeth, M. A. Hitchman, Inorg. Chem. 25 (1986) 1225.
16. J. K. Kar, R. Stevens, C. R. Bowen, J. Alloys Compd. 455 (2008) 121.
17. B. Dejene, H. C. Swart, Luminescence 31 (2016) 1313.
18. V. M. Bachmann. Studies on Luminescence and Quenching Mechanisms in Phosphors for Light Emitting Diodes. PhD Thesis, Utrecht Univeristy Netherlands (1977).
19. B. E. Douglas, D. H. McDaniel, J. J. Alexander, Concepts and Models of Inorganic Chemistry, Wiley, New York (1994).
20. U. Lambert, W. Eysel, Powder Diffr. 1 (1986) 45.
21. J. A. Campá, E. Gutiérrez-Puebla, M. A. Monge, C. R. Z. Valero, J. Mira, J. Rivas, C.

Cascales, I. Rasines, J. Solid State Chem. 120 (1995) 254.

22 M. Dondi, C. Zanelli, M. Arditw, G. Cruciani, J. Am. Ceram. Soc. 94 (2011) 1025

23. R. D. Shannon, C. T. Prewitt, Acta Cryst. Sect. B. 25 (1969) 925.

24. C. K. Jorgensen, Acta Chem. Scand. 9 (1955) 1362.

25. G. Wulfsberg, Inorganic Chemistry, University Science Books, Sausalito, California (2000).

26. N. Srinivasa Rao, M. Purnima, S. Bale, K. Siva Kumar, S Rahman, Bull. Mater. Sci. 29 (2006) 365.

27. L. E. Orgel, J. Chem. Phys. 23 (1955) 1004.

28. C. J. Ballhausen, Introduction to Ligand Field Theory, McGraw-Hill, New York (1962).

29. V. F. Anufrienko, T. M. Yurieva, F. S. Hadzhieva, T. P. Minyukova, S. Y. Burylin, Kinet. Catal. Lett. 27 (1985) 201.

30. H. S. Jang, W. B. Im, D. C. Lee, D.Y. Jeon, S. S. Kim, J. Lumin. 126 (2007) 371.

31. J. S. Kim, Y. H. Park, J. C. Choi, H. L. Park, J. Electron. Soc. 152 (2005) H135.

32. A. L. Allred, J. Inorg. Nucl. Chem. 17 (1961) 215.

33. A. M. Srivastava, Opt. Mater. 31 (2009) 881.

34 L. Sandhya Kumari, P. Prabhakar Rao, A. N. Radhakrishnan, J. Vineetha, S. Sameera, P. Koshy. Sol. Energ. Mat. Sol. Cells 112 (2013) 134.

35. S. Jose, A. Jayaprakash, S. Laha, S. Natarajan, K. G. Nishanth, M. L. P. Reddy, Dyes Pigm 124 (2016) 120.

6

CONCLUSIONS AND FUTURE SCOPE

Significant conclusions derived from the work based on the development of new blue and green inorganic pigments for coloring applications are presented in this concluding chapter. The detailed exploration of optical properties can give a route to develop new, intense colored pigments with multifunctionality for a multitude of applications. Future scope of this work is also presented here.

6.1 General Conclusions

The development of novel blue and green colored inorganic pigments has become a matter of prime focus as the industry has realized the potential of these pigments for various applications. This attempted to prepare a new class of blue and green inorganic pigments having less toxicity as an alternative to the existing pigments. The samples were synthesized by solid state route and characterized for their structural and optical properties. The effect of substitution on the structure, microstructure and optical properties of these pigments has been studied. The coloring performance of the pigments in a polymer matrix like PMMA is also highlighted. The NIR reflectance studies of a series of developed pigments have been explored to use them as potential candidates for cool roof applications. The relevant conclusions derived from the current work focused on developing blue and green colored inorganic pigments are presented here

- In the case of currently available blue pigments, the blue color is normally assigned to the incorporation of Co^{2+} in tetrahedral symmetry. Even though cobalt is considered toxic, cobalt appears to be hardly replaceable in order to achieve a deep blue coloration.
- In view of this, the new blue colored ceramic pigment prepared with a very low doping concentration of cobalt in the octahedral site of the monoclinic $MgWO_4$ host lattice. Intense blue hue was obtained at a relatively low doping concentration of Co^{2+} (20 mol%) with b^* value of -46.97, which is considerably intense than cobalt aluminate spinel (b^* = -32.70).
- An important reduction in the toxicity and cost of production of the obtained ceramic pigments may be accomplished. The IR reflectance of $Mg_{1-x}Co_xWO_4$ (x = 0.20) is enhanced with the addition of a mineralizer upto 70%. They also improve morphology as well as crystallinity and help in the formation of the host lattice structure at a lower calcination temperature.
- Recent times research efforts are being made to develop and explore blue chromophore for environmentally benign pigment applications.
- Novel blue chromophore for environmentally benign pigments applications was prepared with the introduction of Mn^{3+} in the monoclinic $LaGaGe_2O_7$ host

other than the hexagonal perovskites. The Mn^{3+} substitution affected the absorption spectra of $LaGa_{1-x}Mn_xGe_2O_7$ (x = 0.1 to 0.4), that is different from the absorption spectra of Mn^{3+} doped hexagonal perovskites. This effect is due to the presence of longer Mn–O apical bond length in $LaGa_{1-x}Mn_xGe_2O_7$ (x = 0.1 to 0.4).

- Shorter Mn–O apical bonds favor the origin of blue color in hexagonal perovskites. In the present system, all the doped samples possess longer Mn–O apical bonds, this situation also favors the development of blue color.
- However, a few host structures having a Mn^{3+} ion in their geometry have been found so far. In this respect, there is a growing need for finding out host structures incorporating Mn^{3+}in the trigonal bipyramidal geometry.
- The influence of aliovalent cation substitutions on the optical properties of the $In_2Cu_2O_5$ system has been studied with doping of Zn^{2+} and Sc^{3+} in the host matrix.
- The aliovalent cation substitution affected the optical absorption of the system distinctly as the counter cation substitution of Sc^{3+} influences the crystal field environment of Cu^{2+} ions more dominantly than that of the direct substitution of Zn^{2+} ions.
- The synthesized pigments are chemically and thermally stable. Among the samples both $In_2Cu_{1.9}Zn_{0.1}O_5$ (L^* = 39.03, a^* = -25.16, b^* = 13.17 and R (%) = 68) and $In_{1.9}Sc_{0.1}Cu_2O_5$ (L^* = 38.60, a^* = -22.65, b^* = 14.49 and R (%) = 63) exhibit brilliant green colors and NIR reflectance.
- The modified absorption properties translated in enhancing the green chromaticity and reflectance of the $In_2Cu_2O_5$ system had even better than the commercially available chromium oxide green (L^* = 51.06, a^* = -17.28, b^* = 18.92 and R (%) = 49).
- An attempt has been made to improve the color characteristics of $La_2CuGe_2O_8$ based, environmentally friendly inorganic blue-green pigments. With the doping Li^+ and P^{5+} into the divalent and tetravalent site of $La_2Cu_{1-x}Li_xGe_{2-x}P_xO_8$ (x = 0 to 0.2) systems improved the optical properties exhibiting brilliant blue-green colors (L^* = 72.57, a^* = -38.71, b^* = -17.23 for x = 0.2).

- The technological performances of the synthesized pigment were demonstrated effectively transferring color and reflectance to the plastic, concrete block and metal plate. The developed pigments are chemically and thermally stable

6.2 Future Scope

- This thesis explains the structure and optical properties of some compounds that promises future scope of work and applications.
- The origin of color and optical properties of compound strongly depends on the crystal field splitting. To study the influence of crystal field splitting on the optical properties in more details are suggested.
- A further enhancement in the optical properties can be expected by using various mineralizers, different cationic modifications, different alternate synthesis routes, alteration in the morphology of the particles, etc.
- Application study of the developed pigments for their color as well as IR reflective property on various substrates is required.
- Thesis allows preparing many derivative compositions from the system studied for the coloring applications.

List of publications

1) **Divya S.,** P. Prabhakar Rao, "New inorganic blue pigments from cobalt doped magnesium having transition element oxides and a process for preparing the same," WO2016046846 A1 (**Patent filed in India**).
2) **Divya S.,** P. Prabhakar Rao, Athira K. V. Raj, T. R. Aju Thara, "Enhanced pigmentary properties of rare earth germanates of the type $La_2CuGe_2O_8$ through distortion in CuO_6 octahedron," Dyes Pigm. 142 (2017) 472.
3) **Divya S.,** P. Prabhakar Rao, S. Sameera, Athira K. V. Raj, "Influence of aliovalent cation substitutions on the optical properties of $In_2Cu_2O_5$ system," Dyes Pigm. 134 (2016) 506.
4) **Divya S.,** P. Prabhakar Rao, S. Sameera, Vineetha James, Athira K. V. Raj, "Monoclinic $LaGa_{1-x}Mn_xGe_2O_7$: a new blue chromophore based on Mn^{3+} in trigonal bipyramidal coordination with longer apical bond lengths," , RSC Adv. 5 (2015) 27278.
5) **Divya S.,** P. Prabhakar Rao, Athira K. V. Raj, T. R. Aju Thara, "Synthesis characterization and optical properties of Co-$MgWO_4$ blue inorganic pigments" (Under Revision).
6) T. R. Aju Thara, P. Prabhakar Rao, **S. Divya,** Athira K. V. Raj, T. S. Sreena, "Enhanced near infrared reflectance with brilliant yellow hues in scheelite type solid solutions, $(LiLaZn)_{1/3}MoO_4$–$BiVO_4$ for energy saving products". ACS Sustainable Chem. Eng. 5 (6) (2017) 5118.
7) Athira K. V. Raj, P. Prabhakar Rao, **S. Divya,** T. R. Aju Thara, "Terbium doped Sr_2MO_4 [M = Sn and Zr] yellow pigments with high infrared reflectance for energy saving applications," Powder Technol. 311 (2017) 52.
8) Athira K. V. Raj, P. Prabhakar Rao, **S. Divya,** T. R. Ajuthara, "High IR reflecting yellow colorants in yttrium doped $MgBi_{2-x}O_4$ solid solutions," Chem. Lett. 45 (2016) 928.
9) S. Sameera, P. Prabhakar Rao, **S. Divya**, Athira K. V. Raj, "Brilliant IR reflecting yellow colorants in rare earth double molybdate substituted $BiVO_4$ solid solutions for energy saving applications," ACS Sustainable Chem. Eng. 3 (2015) 1227.

10) Athira K V. Raj, P. Prabhakar Rao, S. Sameera, **S. Divya,** "Intense red pigments based on terbium-doped yttrium cerate with high NIR reflectance for cool roof and surface coating applications," Dyes Pigm. 122 (2015)116.

11) Vineetha James, P. Prabhakar Rao, S. Sameera, **S. Divya**, "Multiferroic based reddish brown pigments: $Bi_{1-x}M_xFeO_3$ (M = Y and La) for coloring applications," Ceram. Int. 40 (2014) 2229.

12) S. Sameera, P. Prabhakar Rao, Vineetha James, **S. Divya**, Athira K. V. Raj, "Influence of $(LiLa)_{1/2}MoO_4$ substitution on the pigmentary properties of $BiVO_4$," Dyes Pigm. 104 (2014) 41.

13) Athira K. V. Raj, P. Prabhakar Rao, S. Sameera, Vineetha James, **S. Divya**, "Synthesis of novel nontoxic yellow pigments: $Sr_2Ce_{1-x}Tb_xO_4$,"Chem. Lett. 43 (2014) 985.

14) S. Sameera, P. Prabhakar Rao, L. Sandhya Kumari, Vineetha James, **S. Divya**, "Potential NIR reflecting yellow pigments in $(BiV)_{1-x}(YNb)_xO_4$ solid solutions," Chem. Lett. 42 (2013) 521.

Lists of Conference Papers

1) **Divya S.,** P. Prabhakar Rao, "Influence of longer apical bond length of $Mn^{III}O_5$ on the optical properties of monoclinic $LaGa_{1-x}Mn_xGe_2O_7$ system" as Oral Presentation Critical and Strategic Materials for Advanced Technologies [CSMAT], Munnar, Kerala 2017.

2) **Divya S.,** P. Prabhakar Rao, Effects of apical bond distances in d-d transitions of $Mn^{III}O_5$ trigonal bipyramid of monoclinic $LaGa_{1-x}Mn_xGe_2O_7$, International conference on Science, Technology and Applications of Rare Earths [ICSTAR], Thiruvananthapuram, Kerala, 2015.

3) S. Sameera, P. Prabhakar Rao, Vineetha James, and **S. Divya**, Athira K V. Raj, "Ecological IR reflecting pigments in $(BiV)_x(CaMo)_{1-x}O_4$ for cool roof applications," National Conference on Advanced Technologies for Materials Processing and Diagnostics held by Indian Society of Analytical Scientists at kochi, India, 2014.

4) Athira K. V. Raj, P. Prabhakar Rao, S. Sameera, Vineetha James, **S. Divya, "**Synthesis of Terbium doped $Sr_2M_{0.6}Tb_{0.4}O_4$ [M = Si, Sn and Zr] as yellow pigments for coloration

for plastics," National Conference on Advanced Technologies for Materials Processing and Diagnostics held by Indian Society of Analytical Scientists, kochi, India, 2014.

5) S. Sameera, P. Prabhakar Rao, Vineetha James, and **S. Divya**, Athira K V. Raj, "Yellow pigments based on $(LiRE)_{1/2}MoO_4$ – $BiVO_4$ solid solutions for cool roof applications" International Conference on Advanced Functional Materials (ICAFM) held by CSIR, NIIST, Thiruvananthapuram, Kerala, 2014.

6) S. Sameera, P. Prabhakar Rao, Vineetha James, and **S. Divya**, "Enhanced NIR reflecting yellow pigments: $(BiV)_{1-x}(ReP)_xO_4$ (Re = Yand Gd) for cool roof applications," 25th Kerala Science Congress, Technopark, Thiruvananthapuram, 2013.

7) Vineetha James, P. Prabhakar Rao, S. Sameera, **S. Divya**, "Synthesis and Optical properties of La doped $BiFeO_3$ thin films for window coating applications," National Symposium on Polymers and Coatings (NSPC) held by Indian Institute of Chemical Technology (IICT), Hyderabad, 2012.